

# Ultrashort Light Sources from High Intensity Laser-Matter Interaction

## DISSERTATION

zur Erlangung des akademischen Grades

Doctor rerum naturalium  
(Dr. rer. nat.)

vorgelegt

der Fakultät Mathematik und Naturwissenschaften  
der Technischen Universität Dresden

von

Dipl. Phys. Christian Köhler

geboren am 16.09.1981 in Wolgast

Eingereicht am 19.03.2012

Die Dissertation wurde in der Zeit von Dezember 2008 bis  
März 2012 am Max-Planck-Institut für Physik komplexer Systeme angefertigt

Eingereicht am 19.03.2012

1. Gutachter:
2. Gutachter:

# Contents

<b>1. Introduction</b>	<b>1</b>
<b>2. High Intensity Laser Pulse Propagation in Optically Transparent Media</b>	<b>5</b>
2.1. From Maxwell's to wave equation . . . . .	5
2.2. Forward wave equations . . . . .	7
2.3. Co-moving reference frame . . . . .	9
2.4. Slowly varying envelope and complex representation of the electric field	10
<b>3. Terahertz Generation by Ionizing Two-Color Laser Pulses</b>	<b>13</b>
3.1. Introduction . . . . .	13
3.2. The two-color mechanism . . . . .	14
3.2.1. Introduction . . . . .	14
3.2.2. Kerr nonlinearity . . . . .	14
3.2.3. Photo-current mechanism . . . . .	16
3.2.3.1. Charge generation . . . . .	16
3.2.3.2. Equation for the current . . . . .	19
3.3. Local terahertz spectra . . . . .	24
3.3.1. Generic dependencies . . . . .	24
3.3.1.1. Kerr nonlinearity vs. photo-current . . . . .	24
3.3.1.2. Spectral shapes . . . . .	25
3.3.2. Analytical spectral shapes . . . . .	30
3.4. Extended plasma source . . . . .	35
3.4.1. Jefimenko's equation . . . . .	35
3.4.2. Simplified generic setup . . . . .	36
3.4.3. Three dimensional Jefimenko approach . . . . .	38
3.5. Propagated terahertz spectra . . . . .	43
3.5.1. Modeling the fields . . . . .	44
3.5.1.1. Unidirectional pulse propagation equation . . . . .	44
3.5.1.2. Finite-differences time-domain approach . . . . .	45
3.5.2. Nonlinear propagation in the two dimensional finite-difference time-domain approach . . . . .	46
3.5.3. Results from the unidirectional pulse propagation equation . . . . .	48
3.5.3.1. Confrontation with experiment . . . . .	49
3.6. Summary and outlook . . . . .	53

<b>4. Self-Compression of Ultra-Short UV-Pulses in a Self-Defocusing Gas</b>	<b>55</b>
4.1. Introduction . . . . .	55
4.2. Basic idea of self-compression . . . . .	56
4.2.1. Self phase modulation . . . . .	56
4.2.2. Spatial wave collapse . . . . .	58
4.2.3. Demonstration of bulk self-compression . . . . .	60
4.3. Specification of the governing equation . . . . .	60
4.3.1. Forward propagation equation for the complex field . . . . .	60
4.3.2. Material model . . . . .	61
4.4. (1+1)-dimensional setup . . . . .	62
4.4.1. Model equations . . . . .	64
4.4.1.1. The NLS equation . . . . .	64
4.4.1.2. The NLSND equation . . . . .	64
4.4.2. Estimating compression parameters via modulational instability (MI) . . . . .	66
4.4.3. Pulse compression via soliton dynamics . . . . .	68
4.4.4. Simulation results . . . . .	69
4.4.4.1. NLS equation . . . . .	69
4.4.4.2. NLSND equation . . . . .	69
4.4.4.3. (1+1)-dimensional full model equation . . . . .	71
4.4.5. Pulse compression for vanishing Kerr coefficient . . . . .	71
4.5. (3+1)-dimensional setup in radial symmetry . . . . .	73
4.5.1. Nonlinear Schrödinger equation results . . . . .	73
4.5.2. Complete model results . . . . .	74
4.6. Conclusions . . . . .	75
<b>5. Towards a Quantum Mechanical Description of the Medium</b>	<b>77</b>
5.1. Introduction . . . . .	77
5.2. Stating the problem . . . . .	78
5.3. Model . . . . .	80
5.4. Methods . . . . .	82
5.4.1. Numerical implementation . . . . .	82
5.4.2. Extracting the linear response $\chi^{(1)}$ . . . . .	82
5.4.3. Nonlinear polarization $P_{\text{NL}}$ and nonlinear refractive index $n_{\text{NL}}$ . . . . .	83
5.4.4. Higher order nonlinearities . . . . .	84
5.5. Results and discussion . . . . .	85
5.5.1. Linear response $\chi^{(1)}$ . . . . .	85
5.5.2. Nonlinear polarization $P_{\text{NL}}$ and nonlinear refractive index $n_{\text{NL}}$ . . . . .	86
5.5.3. Extraction of higher order responses $\chi^{(2j+1)}$ and ionization cross-section $\sigma_K$ . . . . .	86
5.5.4. Comparison to phenomenological models for polarization . . . . .	92
5.6. Conclusion and outlook . . . . .	99

<b>6. Summary and Outlook</b>	<b>107</b>
<b>A. Finite-Differences Time-Domain Scheme</b>	<b>111</b>
<b>B. Crank Nicholson Scheme</b>	<b>113</b>
<b>C. Definition of the optical intensity</b>	<b>115</b>
C.1. Continuous wave . . . . .	115
C.2. Pulse . . . . .	115
<b>D. Fourier Transformation</b>	<b>117</b>
D.1. Continuous wave . . . . .	117
D.2. Pulse . . . . .	117
<b>E. Nonlinear polarization</b>	<b>119</b>
E.1. Contributions at $\omega_0$ . . . . .	119
E.2. Contributions at $(2j + 1)\omega_0$ . . . . .	121
<b>Nomenclature</b>	<b>123</b>
<b>Bibliography</b>	<b>124</b>
<b>Acknowledgments</b>	<b>135</b>



# 1. Introduction

The development and characterization of new light sources is a major issue in optics, since the advancement of technology continuously provides new areas of application. Light is indispensable for atomic and molecular spectroscopy, imaging in biology and chemistry, modern communication and media technology.

A historical milestone was the development of the Light Amplification by Stimulated Emission of Radiation (LASER) in 1960 [1]. LASERs stand out due to providing monochromatic and over long distances coherent light. Although available for a broad range of wavelengths ranging from the x-ray regime via the ultra-violet and visible to the far infrared region, the operating frequency is determined by the energy difference of the used lasing transition. However, situations occur, where the desired frequency does not match any available lasing transition or where a broad frequency band of the electromagnetic spectrum is needed. For matching specific requirements, the tasks of tuning the operating frequency, broadening the spectrum or generally shaping the laser pulse naturally arises. For that purpose, the interaction of the laser light from a standard source with a medium can be exploited. In particular, applying high-intensity, ultra-short pulses renders the laser-matter interaction nonlinear, which provides a rich variety of physical effects we can utilize for pulse engineering. Among the available media gases excel, since the strength of the interaction can easily be adjusted on large scales by varying the gas pressure and no permanent material damage can occur.

The accurate modeling of laser-matter interaction is highly complex, and is usually approached from two sides. On the one hand side, one focuses on the exact description on the laser light and handles the medium in an approximate manner. Vice versa, one can consider the laser light as given external input and concentrates on the exact modeling of medium. The two approaches are referred to as optical and atomic physics approach, respectively.

When coming from the optics side, the electro-magnetic laser radiation is described by Maxwell's equations. These can model light propagation in matter, provided that (macroscopic) material equations for a (gaseous) medium are introduced in the description. These material equations describe how the considered medium responds to a present light field. For low intensities the response is linear in the applied field, while for high-intensity pulses this response is characterized by a nonlinear dependency on the applied field. Both, the linear and nonlinear dependency are due to the electronic response of the gas atoms to the light field. In general, the medium response can be distinguished between the response of bound and ionized electrons. Within the framework of Maxwell's equations, the polarization accounts for the response from the bound electrons. The polarization is usually modeled by a perturbative expansion of

the response into terms of the applied field, which underlines its approximate character. The response of ionized electrons is accounted for by inclusion of an electric current, whose description often is on a macroscopic, phenomenological level. The combination of Maxwell's and the material equations then describe laser light propagation in media. The simultaneous solution of Maxwell's and material equations can only be performed numerically in most cases.

Approaching laser matter-interaction from the atomic physics side neglects any propagation of the laser light and assumes a fixed spatio-temporal distribution. The medium is exactly described performing the modeling on the quantum mechanical level. If one is interested in the electronic response, the time dependent Schrödinger equation for the electronic wave function with the laser as external time-dependent potential is solved. Depending on the medium, one usually deals with many electron systems and obtaining the electronic wave-function is only numerically possible.

In this thesis, we investigate laser-matter interaction from the optical as well as from the atomic physics side. Chapter 3 and 4 are devoted to the optical description of nonlinear propagation of laser light in gases, where we explore optical nonlinearities to generate new light sources. There, Chapter 3 is dealing with an optical response which originates from ionized electrons and Chapter 4 utilizes a bound electron response. In contrast, Chapter 5 uses the atomic physics approach in order to exactly model the medium response from bound as well as from ionized electrons. This distinction defines the three major parts of this thesis.

The first major part deals with the generation of THz radiation, with frequencies of  $10^{12} \dots 10^{14}$  Hz lying between the infrared and microwave region of the electromagnetic spectrum. These frequencies correspond to wavelength of 0.02..2 mm and photon energies on the order of meV. The position of THz frequencies in the electromagnetic spectrum provides desired features for a broad range of applications. In particular, the development of nonlinear and time-domain THz spectroscopy [2–4] provided the possibility of nondestructive material imaging. The THz imaging is indispensable in chemistry, where the characteristic spectral features of many materials in the THz regime are used to determine chemical substances including, e.g. narcotics or explosives [5,6]. In biology THz radiation is used for analyzing human skin tissue [7] or probing bio-molecules [8]. Furthermore, remote sensing of aerosols in the atmosphere involves THz radiation [9,10]. The numerous ways to generate THz radiation include the THz quantum cascade laser [11], photo-conductive switches [12], optical rectification in second-order nonlinear crystals [13–16] and conical emission from laser filaments [17]. These generation mechanisms feature a serious disadvantage: the obtained THz field amplitudes are limited due to saturation or damage of the material for high intensities. Setups in gaseous media avoid these difficulties, since for high intensities the gas is just ionized and we deal with a plasma. In preformed plasmas, mechanisms for THz generation were proposed, which exploit ponderomotive forces on the relativistic electrons [18] or excite plasma oscillations [19]. However, another mechanism in gases stands out, since it provides comparably high THz amplitudes up to 100 MV/m and spectral widths of 100 THz. By focusing an ionizing two-color laser



---

consisting of an optical fundamental and its second harmonic into a gas, Cook et al. showed that the second frequency is crucial for the observation of THz radiation [20]. Thus THz generation was interpreted as an optical rectification process, where both frequencies sum up to THz frequencies via a third order Kerr nonlinearity [21–24]. The for a Kerr nonlinearity unexpected scaling of the THz field amplitude [25] and the demonstration that a Kerr nonlinearity is much too small to explain the observed THz field strength [26] render the rectification process unlikely. The observation of a threshold for THz emission [22, 27] that corresponds to the onset of plasma formation along with the measurement of a plasma current [28] revealed the photo-current mechanism as the source for THz radiation [22, 27–31]. In the photo-current setup, the input field ionizes the gas and accelerates the newly born electrons. The accelerated electrons constitute a current, which features a low frequency component in the THz regime due to the temporal asymmetry of the two-color input field. That current in turn emits the THz radiation. A detailed analysis and the development of a model describing this mechanism for THz generation is the aim of Chapter 3.

The second major part explores the possibility of laser self-compression in gases. In order to obtain short temporal structures a broad extension in the spectral domain is required. Additionally, one has to ensure a flat spectral phase; only then all frequencies contained in the pulse contribute at the same time. Thus for the compression of a given pulse, one has to broaden its spectrum and adjust a flat spectral phase. Among other compression schemes, such as using frequency conversion in filaments [32] or cascading quadratic nonlinearities [33–35], a convenient setup consists of coupling the initial pulse into an optical fiber, which guides the light [36]. Then the spatially transverse distribution of the light is determined by the excited mode of the fiber and one deals with purely temporal dynamics. For enlarging the spectrum, one employs the spectral broadening ability of self-phase modulation (SPM) by the optical Kerr effect. The strength of this third order effect is determined by the value of the Kerr coefficient  $n_2$  which depends on the employed medium and wavelength. Nevertheless, one obtains a varying spectral phase, which can be accounted for by shining the spectrally broadened light on chirped mirrors or diffractive gratings as in Reference [36]. An elegant alternative uses another nonlinear effect for dealing with the spectral phase: The group velocity dispersion (GVD) characterized by the coefficient  $k_2$  also imposes a spectral phase on the pulse, which can be used to cancel the phase obtained from SPM [37]. For that, different signs of the coefficients  $n_2$  and  $k_2$  are required. For the usually employed wavelength the Kerr coefficient is positive  $n_2 > 0$  and the GVD coefficient is negative  $k_2 < 0$ . However, coupling the input pulse in and out the fiber is complicated and comes along with loss in energy and limitations in the applied intensity, which has to stay below the damage threshold of the fiber (-windows). Therefore, the compression is desired to be handable in bulk gases. Then, one faces a serious problem: For the usual situation of  $n_2 > 0$  and  $k_2 < 0$  one encounters the transverse spatial collapse [38] of the input beam due to the refractive index variations introduced by  $n_2$  if the power of the input pulse exceeds a critical value [39, 40, 40]. The collapse can be avoided under the (exotic) condition that  $n_2 < 0$ . For successful compression

then  $k_2 > 0$ . Indeed such configurations can be found near resonances, e.g. in xenon for  $\lambda = 250$  nm [41]. Close to resonances however, the for spectral broadening required Kerr coefficient  $n_2$  becomes strongly frequency dependent [42]. This dispersion challenges the compression scheme, which is demonstrated successful for a constant  $n_2$  for all frequencies in the pulse. Thus, the aim of Chapter 4 is to analyze the influence of such an dispersive  $n_2$  on the performance of the pulse compression mechanism [43, 44].

The third major part follows the atomic physics approach and aims at an exact description of nonlinear medium responses to an external laser. An exact description is crucial to explain a broad range of physical effects. For example, ionization of atoms, sum and difference frequency generation, spectral broadening due to self phase modulation, soliton formation and beam collapse are phenomena, which we encounter in the first and second major part of this work [43, 45–47]. There, for low laser intensities the response of the medium is due to the bound electrons, which induce a polarization. The perturbative treatment of the response consists in the usual expansion of the polarization into a Taylor series in terms of the applied field amplitude. For low field strength a truncation after the first nonlinear term is justified. We deal with a centrosymmetric, homogeneous gas, thus all even order terms vanish, rendering a third order nonlinearity the lowest nonlinear order. Apart from, e.g. third harmonic generation, the famous optical Kerr effect is a consequence of a third order nonlinearity. The Kerr effect introduces an intensity dependence of the refractive index  $n = n_0 + n_2 I$ , which leads to difficulties when modeling laser propagation in two or more transverse spatial dimensions. For increasing intensity, the refractive index formally diverges for  $n_2 > 0$ . Such an unphysical behavior contradicts observations, e.g. of laser filamentation [39, 48–51], where a saturation of the refractive index is mandatory for their formation [50]. For describing the saturation of the refractive index one can follow two approaches. First, for high enough intensity the medium gets ionized. The generated electrons cause a contribution to the refractive index with a negative value [52], thus eventually stopping or even canceling the Kerr contribution. On the other hand, one can argue that for increasing intensity the perturbative expansion of the polarization should include higher order terms [53, 54]. Indeed, recent measurements of higher order Kerr terms  $n_{2i} I^i$ , which meet the requirement of being negatively valued in order to saturate the refractive index, support this possibility [55, 56]. The disclosure of the physical nature of the saturation of the refractive index was attempted earlier [57–59], but a definite answer is still missing, as underlined by the still ongoing controversy in modeling filamentation [60, 61]. Our goal in Chapter 5 is to reveal the physical mechanism for the saturation of the refractive index.

## 2. High Intensity Laser Pulse Propagation in Optically Transparent Media

In this chapter we review the derivation of basic equations, describing the propagation of laser pulses in nonlinear media. By doing so, we introduce fundamental expressions that reoccur repeatedly throughout this work and are the common basis for all chapters.

### 2.1. From Maxwell's to wave equation

The propagation of light through a (nonlinear) optical medium is described by the macroscopic Maxwell's equations

$$\nabla \cdot \mathbf{D} = \rho_f, \quad (2.1)$$

$$\nabla \cdot \mathbf{B} = 0, \quad (2.2)$$

$$\nabla \times \mathbf{E} = -\frac{\partial \mathbf{B}}{\partial t}, \quad (2.3)$$

$$\nabla \times \mathbf{H} = \mathbf{J}_f + \frac{\partial \mathbf{D}}{\partial t}, \quad (2.4)$$

where the electric induction  $\mathbf{D}$ , the electric field  $\mathbf{E}$ , the magnetic induction  $\mathbf{B}$ , the magnetic field  $\mathbf{H}$ , the free charge density  $\rho_f$  and the free current density  $\mathbf{J}_f$  are all real valued, because being physical quantities. Assuming a nonmagnetic medium  $\mathbf{B} = \mu_0 \mathbf{H}$  and the material to be polarizable in the sense that  $\mathbf{D} = \varepsilon_0 \mathbf{E} + \mathbf{P}$  leads to a wave equation in a form that is often used as starting point for further calculations

$$\nabla^2 \mathbf{E} = \mu_0 \frac{\partial \mathbf{J}_f}{\partial t} + \mu_0 \varepsilon_0 \frac{\partial^2 \mathbf{E}}{\partial t^2} + \mu_0 \frac{\partial^2 \mathbf{P}}{\partial t^2} + \nabla (\nabla \cdot \mathbf{E}). \quad (2.5)$$

We introduce the Fourier domain by the transformations

$$\hat{F}(\omega) = \int dt F(t) e^{i\omega t}, \quad (2.6)$$

$$F(t) = \int \frac{d\omega}{2\pi} \hat{F}(\omega) e^{-i\omega t} \quad (2.7)$$

for further convenience.

The response of the medium is expressed by  $\mathbf{J}_f$  for the free electrons, while the polarization  $\mathbf{P}$  models the response of the bound electrons. For frequencies far from any material resonances it is possible to express the polarization  $\hat{\mathbf{P}}$  in a power series in  $\hat{\mathbf{E}}$ :  $\hat{\mathbf{P}} = \hat{\mathbf{P}}^{(1)} + \hat{\mathbf{P}}^{(3)} + \hat{\mathbf{P}}^{(5)} + \dots$ ,  $\hat{\mathbf{P}}^{(j)} \sim \hat{\mathbf{E}}^j$ , where all contributions of even power in  $\hat{\mathbf{E}}$  vanish due to inversion symmetry in centro-symmetric media. In general,  $j$ th order of  $P$  is proportional to the  $j$ th order susceptibility tensor  $\chi^{(j)}$ :

$$\hat{P}_\mu = \varepsilon_0 \sum_{\alpha_1, \dots, \alpha_j} \int \dots \int \chi_{\mu\alpha_1, \dots, \alpha_j}^{(j)}(-\omega_\sigma; \omega_1 \dots \omega_j) \quad (2.8)$$

$$\times \hat{E}_{\alpha_1}(\omega_1) \dots \hat{E}_{\alpha_j}(\omega_j) \delta(\omega - \omega_\sigma) d\omega_1 \dots d\omega_j \quad (2.9)$$

$$\omega_\sigma = \omega_1 + \dots + \omega_j \quad (2.10)$$

We refer to  $\hat{\mathbf{P}}^{(1)} = \hat{\mathbf{P}}_{\text{Lin}}$  as the linear polarization and to the remainder  $\hat{\mathbf{P}}_{\text{NL}} = \hat{\mathbf{P}}^{(3)} + \hat{\mathbf{P}}^{(5)} + \dots$  as the nonlinear part. Note that such a power series expansion is an approximation for the polarization only and we refer the reader to Section 5 for a detailed discussion on the applicability of Equation (2.8).

We consider isotropic media and linearly polarized light  $\mathbf{E} = E_x \mathbf{e}_x \rightarrow E$ , therefore the tensor  $\chi^{(1)}$  reduces to its diagonal elements and the linear polarization simplifies to

$$\hat{P}_{\text{Lin}}(\omega) = \varepsilon_0 \chi^{(1)}(-\omega; \omega) \hat{E}(\omega), \quad (2.11)$$

which leads together with the nonlinear part to  $\mathbf{P} = P_x \mathbf{e}_x \rightarrow P$  only having contributions parallel to the input field. We introduce the wave number  $k(\omega)$  and the dielectric function  $\varepsilon(\omega)$

$$k(\omega) = \frac{\omega}{c} \sqrt{1 + \chi^{(1)}(-\omega; \omega)} = \frac{\omega}{c} \varepsilon(\omega) \quad (2.12)$$

with the speed of light  $c$  and express Equation (2.5) in Fourier space

$$\left( \nabla^2 + k^2(\omega) \right) \hat{E} = -i\mu_0 \omega \hat{J}_f - \mu_0 \omega^2 \hat{P}_{\text{NL}}, \quad (2.13)$$

where we neglected  $\nabla \cdot \mathbf{E}$ .  $\nabla \mathbf{E} = 0$  is justified in the following for the setups under consideration in Section 4 and 5.

We have

$$\mathbf{D} = \varepsilon_0 \mathbf{E} + \mathbf{P}, \quad \mathbf{P} = \mathbf{P}_{\text{Lin}} + \mathbf{P}_{\text{NL}}, \quad (2.14)$$

thus

$$\nabla \cdot \mathbf{E} = \frac{\nabla \cdot \mathbf{D} - \nabla \cdot \mathbf{P}_{\text{Lin}} - \nabla \cdot \mathbf{P}_{\text{NL}}}{\varepsilon_0}. \quad (2.15)$$

In Section 4 we deal with neutral atoms, which justifies  $\rho_f = 0$ . Although we consider a (partially) ionized gas in Section 3, the overall charge is zero and the gas is neutral. This absence of free charges  $\rho_f = 0$  leads to  $\nabla \cdot \mathbf{D} = 0$  for both cases, and for

homogeneous media we arrive at

$$\nabla \cdot \hat{\mathbf{E}} = -\frac{\nabla \cdot \hat{\mathbf{P}}_{NL}}{\varepsilon(\omega) \varepsilon_0} \quad (2.16)$$

in Fourier space. For Section 4 and 5 we assume a third order nonlinear polarization  $\hat{\mathbf{P}}_{NL} = \hat{\mathbf{P}}^{(3)}$ , which reads for linearly polarized light ( $\hat{\mathbf{P}}_{NL} = \hat{P}_{NL,x} \mathbf{e}_x \rightarrow \hat{P}_{NL}$ ) in isotropic media

$$\begin{aligned} \hat{P}_{NL}(\omega) = & \varepsilon_0 \iint \chi^{(3)}(\omega; \omega - \omega_1 - \omega_2, \omega_2, \omega_1, ) \\ & \times \hat{E}(\omega_1) \hat{E}(\omega_2) \hat{E}(\omega - \omega_1 - \omega_2) d\omega_1 d\omega_2. \end{aligned} \quad (2.17)$$

In each Section, we include a specific  $\chi^{(3)}$ . In particular in Section 4 we deal with frequencies close to a material resonance and a specialized  $\chi^{(3)}$  has to be included to account for contributions from the resonance. For an instantaneous, i.e. dispersionless  $\chi^{(3)}$  the nonlinear polarization mainly contributes to the central frequency  $\omega_0$ , since contributions accounting for third harmonic generation  $3\omega_0$  appear with phase mismatch  $k(3\omega_0) \neq 3k(\omega_0)$ , thus cancel upon propagation. In time domain, the third order polarization Equation (2.17) simplifies to

$$P_{NL}(t) = 3\varepsilon_0 \chi^{(3)}(-\omega_0; -\omega_0, \omega_0, \omega_0) E(t)^3. \quad (2.18)$$

Due to the quasi linear polarization of our light  $|E_x| \gg |E_{y,z}|$ , it is sufficient to show  $|\nabla \mathbf{E}| \ll |\partial_x E_x| = |\partial_x E|$ . Again using the homogeneity of the medium,

$$|\nabla \cdot \mathbf{E}| = \left| \frac{3}{\varepsilon(\omega_0)} \chi^{(3)}(-\omega_0; -\omega_0, \omega_0, \omega_0) \cdot \left| \partial_x E(t)^3 \right| \right| \quad (2.19)$$

$$\leq \left| \frac{3}{\varepsilon(\omega_0)} \chi^{(3)}(-\omega_0; -\omega_0, \omega_0, \omega_0) \left| 3|E(t)|^2 \right| \partial_x E(t) \right| \quad (2.20)$$

$$\ll |\partial_x E(t)| \quad (2.21)$$

for typical values  $\chi^{(3)}|E(t)|^2 \approx 1 \times 10^{-5}$  in Section 3 and  $\chi^{(3)}|E(t)|^2 \approx 1 \times 10^{-6}$  for Section 4 (see Table 4.2) for peak values of  $|E(t)|$ .

## 2.2. Forward wave equations

For the solution of Equation (2.13) it is justified in many situations to consider forward propagating fields only. Then, the forward direction is given by the propagation direction of the laser pulse, which we here assume to be the positive  $z \geq 0$  direction. It is convenient to split

$$\nabla^2 = \partial_z^2 + \partial_\perp^2, \quad (2.22)$$

where  $\partial_{\perp} = \partial_x^2 + \partial_y^2$  denotes the derivatives with respect to transverse coordinates which are responsible for diffraction. Equation (2.13) now reads

$$\left(\partial_z^2 + \nabla_{\perp}^2 + k^2(\omega)\right) \hat{E} = -i\mu_0\omega\hat{J}_f - \mu_0\omega^2\hat{P}_{\text{NL}}, \quad (2.23)$$

which is the starting point for two approaches modeling forward propagating fields. These are described in the following.

For the first approach, we decompose the electric field  $\hat{E}$  into a forward and backward propagating part

$$\hat{E} = \hat{U}_+ e^{ik(\omega)z} + \hat{U}_- e^{-ik(\omega)z}. \quad (2.24)$$

For  $|k_{\perp}| \ll |k(\omega)|$ , that is for transverse wave numbers much smaller than longitudinal ones and for small nonlinearities on the r.h.s. of Equation (2.23), the backscattered part  $U_-$  is negligible [62]. We introduce forward and backward propagators

$$\hat{D}(\omega)_{\pm} = \partial_z \mp ik(\omega) \quad (2.25)$$

and rewrite Equation (2.23) to

$$\hat{D}(\omega)_+ \hat{D}(\omega)_- \hat{E} = -\nabla_{\perp}^2 \hat{E} - i\mu_0\omega\hat{J}_f - \mu_0\omega^2\hat{P}_{\text{NL}}. \quad (2.26)$$

The backward operator  $\hat{D}(\omega)_-$  reads

$$\hat{D}(\omega)_- \hat{E} = (\partial_z + ik(\omega)) \hat{U}_+ e^{ik(\omega)z} = e^{ik(\omega)z} (\partial_z \hat{U}_+ + 2ik(\omega) \hat{U}_+). \quad (2.27)$$

We apply the so-called paraxiality assumption  $|\partial_z \hat{U}_+| \ll |ik(\omega) \hat{U}_+|$ , which holds if  $\hat{U}_+$  does not vary significantly on propagation distances  $\sim \lambda = 2\pi c/\omega$ . After neglecting the small contribution  $\partial_z \hat{U}_+$  we end up with the so-called forward Maxwell equation [63]

$$\partial_z \hat{E} = \frac{i}{2k(\omega)} \nabla_{\perp}^2 \hat{E} + ik(\omega) \hat{E} - \frac{\mu_0}{2k(\omega)} (\omega\hat{J}_f - i\omega^2\hat{P}_{\text{NL}}). \quad (2.28)$$

The second, more general approach [64] decomposes Equation (2.23) into modal fields

$$\hat{E} = \hat{U}_+ e^{i\sqrt{k^2(\omega) - k_{\perp}^2}z} + \hat{U}_- e^{-i\sqrt{k^2(\omega) - k_{\perp}^2}z}, \quad (2.29)$$

where  $k_{\perp}^2 = k_x^2 + k_y^2$  and assumes the nonlinearity on the r.h.s. of Equation (2.23) to be completely determined by the forward propagating part of  $\hat{E}$ . Then, with similar forward and backward operators

$$\hat{D}_{\pm}^{\perp}(\omega) = \partial_z \mp i\sqrt{k^2(\omega) - k_{\perp}^2} \quad (2.30)$$

and again keeping only the governing forward part  $\hat{U}_+ e^{i\sqrt{k^2(\omega) - k_{\perp}^2}z}$ , one arrives at the

unidirectional pulse propagation equation (UPPE) [64]:

$$\partial_z \hat{E} = i\sqrt{k^2(\omega) - k_\perp^2} \hat{E} - \frac{\mu_0}{2\sqrt{k^2(\omega) - k_\perp^2}} (\omega \hat{J}_f - i\omega^2 \hat{P}_{\text{NL}}) \quad (2.31)$$

For  $|k_\perp| \ll |k(\omega)|$  Equation (2.31) is identical to the previously derived forward Maxwell Equation (2.28).

## 2.3. Co-moving reference frame

Since it is convenient for numerics, we go over from our fixed reference frame  $(z, t, F)$  to a co-moving time frame  $(z', \tau, F')$ , defined by

$$\tau = t - k_1 z \quad (2.32)$$

$$z' = z \quad (2.33)$$

$$F'(z', \tau) = F(z, t), \quad (2.34)$$

where  $k_1$  originates from the Taylor expansion of the linear dispersion  $k(\omega)$  around the center frequency  $\omega_0$

$$k(\omega) = k_0 + \frac{k_1}{1!} \bar{\omega} + \frac{k_2}{2!} \bar{\omega}^2 + D, \quad D = \sum_{n=3} \frac{k_n}{n!} \bar{\omega}^n, \quad (2.35)$$

where

$$k_i = \left. \frac{\partial^i k(\omega)}{\partial \omega^i} \right|_{\omega_0}, \quad \bar{\omega} = \omega - \omega_0. \quad (2.36)$$

Since  $v_g = 1/k_1$ , the new time frame moves with the group velocity  $v_g$  along the positive  $z$ -direction. The fields in Fourier space are connected via

$$\hat{F}(z, \omega) = \hat{F}'(z', \omega) e^{i\omega k_1 z} \quad (2.37)$$

and the differential operators obey

$$\partial_z = \partial_{z'} - k_1 \partial_\tau, \quad \partial_t = \partial_\tau. \quad (2.38)$$

After skipping the  $'$  for brevity, the forward Maxwell Equation (2.28) is written as

$$\partial_z \hat{E} = \frac{i}{2k(\omega)} \nabla_\perp^2 \hat{E} + i(k(\omega) - k_1 \omega) \hat{E} - \frac{\mu_0}{2k(\omega)} (\omega \hat{J}_f - i\omega^2 \hat{P}_{\text{NL}}). \quad (2.39)$$

This is the starting point for the derivation of a fundamental propagation equation in the next section.

## 2.4. Slowly varying envelope and complex representation of the electric field

For configurations, where the electro-magnetic radiation is limited to a small frequency window around a central frequency  $\omega_0$ , a significant simplification in Equation (2.39) can be achieved. We split the electric field into a plane wave with central frequency  $\omega_0$  and the corresponding wave number  $k(\omega_0) = k_0$  and the remaining envelope  $U$

$$E(z, t) = \frac{U(z, t)}{2} e^{ik_0 z - i\omega_0 t} + \text{c.c.} \quad (2.40)$$

Then,  $U(z, t)$  is slowly varying in  $z$  and  $t$  when compared to  $e^{ik_0 z - i\omega_0 t}$ . The intensity  $I$  is defined as temporal average of the absolute value of the pointing vector, which here is given by  $S = \varepsilon_0 c |E(t)|^2$ . Thus

$$I = \varepsilon_0 c \langle |E|^2 \rangle_t \quad (2.41)$$

$$= \frac{\varepsilon_0 c}{4} \langle (U(z, t)^2 e^{i2(k_0 z - \omega_0 t)} + 2|U(z, t)|^2 + U^*(z, t)^2 e^{-i2(k_0 z - \omega_0 t)}) \rangle_t \quad (2.42)$$

$$= \frac{\varepsilon_0 c}{2} |U(z, t)|^2, \quad (2.43)$$

where  $*$  denotes the complex conjugate and we exploited the time average in the second line to gain the third. It is convenient to introduce a new envelope  $\mathcal{E}$  such, that  $|\mathcal{E}|^2 = I$ . Then

$$U(z, t) = \mathcal{E}(z, t) \sqrt{\frac{2}{\varepsilon_0 c}} \quad (2.44)$$

and the electric field reads

$$E(z, t) = \sqrt{s} \mathcal{E}(z, t) e^{i(k_0 z - \omega_0 t)} + \text{c.c.}, \quad (2.45)$$

where we introduced the scaling factor  $s = 1/2\varepsilon_0 c$ . The Fourier components of the electric field in terms of the new envelope  $\mathcal{E}$  express as

$$\hat{E}(\omega) = \int dt \sqrt{s} (\mathcal{E}(z, t) e^{ik_0 z - i\omega_0 t} + \mathcal{E}^*(z, t) e^{-ik_0 z + i\omega_0 t}) e^{i\omega t} \quad (2.46)$$

$$= \sqrt{s} (\hat{\mathcal{E}}(z, \omega - \omega_0) e^{ik_0 z} + \hat{\mathcal{E}}^*(z, \omega + \omega_0) e^{-ik_0 z}) \quad (2.47)$$

Since  $\hat{E}(-\omega) = \hat{E}^*(\omega)$  holds and  $|\hat{\mathcal{E}}(\omega - \omega_0)| \ll |\hat{\mathcal{E}}(\omega + \omega_0)|$  for  $\omega > 0$  it is sufficient to deal with positive frequencies only. Therefore, we use the final definition of the complex envelope

$$\hat{\mathcal{E}}(\bar{\omega}) = \Theta(\bar{\omega} + \omega_0) \frac{1}{\sqrt{s}} \hat{E}(\bar{\omega} + \omega_0) e^{-ik_0 z} \quad (2.48)$$



to express Equation (2.39) as

$$\partial_z \hat{\mathcal{E}} = \frac{i}{2k(\omega)} \nabla_{\perp} \hat{\mathcal{E}} + i(k(\omega) - k_0 - k_1 \bar{\omega}) \hat{\mathcal{E}} - \frac{\mu_0}{2k(\omega)} (\omega \hat{\mathcal{J}}_f - i\omega^2 \hat{\mathcal{P}}_{NL}), \quad (2.49)$$

where  $\hat{\mathcal{J}}_f$  and  $\hat{\mathcal{P}}_{NL}$  denote the envelope expressions for  $\hat{J}_f$  and  $\hat{P}_{NL}$ , respectively.

We demonstrate the potential for significant simplification by deriving the well known nonlinear Schrödinger equation (NLS), which describes despite its simplicity fundamental nonlinear optical effects (see Section 4.2). We consider Equation (2.49) in a charge and current free configuration  $\hat{\mathcal{J}}_f \equiv 0$ . First, we keep only the leading order of linear dispersion by taking

$$k(\omega) \approx k(\omega_0) \quad (2.50)$$

in the first term in Equation (2.49) and

$$k(\omega) - k_0 - k_1 \bar{\omega} \approx \frac{k_2}{2} \bar{\omega} \quad (2.51)$$

in the second term, where  $k_2$  originates from the Taylor expansion in Equation (2.35). Second, assuming a third order Kerr term Equation (2.17) for the nonlinear polarization gives in envelope representation

$$\begin{aligned} \hat{\mathcal{P}}_{NL}(\omega) &= \varepsilon_0 s^{3/2} \iint d\omega_1 d\omega_2 \chi^{(3)}(-\omega; \omega - \omega_1 - \omega_2, \omega_2, \omega_1) \\ &\quad \times 3\hat{\mathcal{E}}(\bar{\omega}_1) \hat{\mathcal{E}}(\bar{\omega}_2) \hat{\mathcal{E}}^*(\bar{\omega}_1 + \bar{\omega}_2 - \bar{\omega}) e^{i(k_0 + k_1 \bar{\omega})z}, \end{aligned} \quad (2.52)$$

where we only included governing contributions of the nonlinear polarization, namely contributions to the central frequency  $\omega_0$  of our input field and neglected not phase matched ( $k(3\omega_0) \neq 3k(\omega_0)$ ) third harmonic contributions. Furthermore, we take the susceptibility  $\chi^{(3)}$  to be instantaneous, i.e. non-dispersive

$$\chi^{(3)}(-\omega; \omega - \omega_1 - \omega_2, \omega_2, \omega_1) = \chi^{(3)}(-\omega_0; -\omega_0, \omega_0, \omega_0). \quad (2.53)$$

Neglecting the dispersion of the linear refractive index  $n(\omega) \approx n(\omega_0) = n_0$  in the wave number  $k(\omega) = \omega n(\omega)/c$  allows us to reduce the prefactor of the nonlinear polarization to

$$\frac{\omega^2}{c^2 k(\omega)} = \frac{\omega_0 + \bar{\omega}}{cn_0} = \frac{\omega_0}{cn_0} \quad (2.54)$$

for  $\omega_0 \gg \bar{\omega}$ . Switching back to time domain results in the nonlinear Schrödinger equation

$$\partial_z \mathcal{E} = \frac{i}{2k_0} \nabla_{\perp} \mathcal{E} - i \frac{k_2}{2} \partial_t^2 \mathcal{E} + i \frac{\omega_0}{c} n_2 |\mathcal{E}|^2 \mathcal{E}, \quad (2.55)$$

which can be considered as the fundamental and simplest model for describing non-

## *2. High Intensity Laser Pulse Propagation in Optically Transparent Media*

---

linear propagation of light.

# 3. Terahertz Generation by Ionizing Two-Color Laser Pulses

## 3.1. Introduction

The subject of investigation is radiation in the tera-Hertz (THz) regime, with characteristic frequencies from  $10^{12}$  to  $10^{14}$  Hz right between infrared and microwaves. These frequencies correspond to wavelengths of 0.02 to 2 mm or photon energies of the order of meV. THz radiation allows a broad variety of applications. For instance fundamental insight was gained through the development of nonlinear and time-domain THz spectroscopy [2–4]. For example, in medicine THz radiation is used for the analysis of human skin cancer tissue [7], bio molecules are probed with THz radiation [8], hidden narcotics can be traced [6] and remote sensing of THz radiation provides information about the atmosphere [9, 10].

There are numerous ways to generate THz radiation, such as using semiconductor photo-conductive switches [12], optical rectification in second-order nonlinear crystals [13–16] or conical THz emission from laser filaments [17]. However, these methods are limited in achievable THz field amplitudes due to saturation or material damage for high input intensities.

A promising alternative setup consists of focusing an ionizing two-color laser into a gas cell. The obtained THz radiation features comparable high amplitudes of up to 100 MV/m and broad spectral widths of 100 THz at the same time. Initially being attributed to a four-wave rectification process [20, 23–25], THz generation was revealed to be caused by the so-called photo-current mechanism [22, 27–31]. In that mechanism, the input field ionizes the medium and subsequently accelerates the generated charge. The accelerated charge builds up a current, which possesses a low frequency component in the THz regime due to the two-color nature of the input laser. This current finally emits the THz radiation. The two-color photo-current mechanism has to be distinguished from other generation mechanisms in gases, which, e.g., use ponderomotive forces of relativistic electrons in preformed plasmas [18] or excite plasma oscillations [19] and are not under consideration in this work.

The aim of this chapter is to describe and to model the THz radiation one obtains when focusing a two-color laser into a gas. We start with the description of the generation mechanism and the underlying physical processes in Section 3.2. Then, the characterization of THz radiation in the spectral domain in Section 3.3 provides the mandatory understanding for modeling realistic setups in Section 3.5, where we

successfully reproduce experimental results. Finally, we summarize in Section 3.6.

## 3.2. The two-color mechanism

### 3.2.1. Introduction

In this Section we explain the physical mechanism that generates the THz radiation. The typical situation we encounter involves the presence of a high intensity two-color laser pulse, being focused into a gas. In this context, high intensity denotes the regime, where the response of the gas is nonlinear, including ionization of the gas. Then, for the medium response a distinction can be drawn between a response originating from the bound electrons and a response which is due to ionized electrons (also see Section 5). We deal with situations, where the medium is partially ionized and thus encounter both responses. In principle, both contributions can lead to emission of THz radiation. We therefore explain the mechanism which generates THz radiation from bound electrons in Section 3.2.2, followed by Section 3.2.3, which is dedicated to the more detailed description of the response of ionized electrons, since the latter one will turn out to be the dominating one.

In the beginning, we consider a small gas volume only. The small volume ensures the electric field to be the same for all spatial points within that volume for a fixed instant of time. In that local approximation, we can assume a two-color input field without any spatial dependencies

$$E(t) = A \left( e^{-\frac{t^2}{\sigma_t^2}} \sqrt{1-\xi} \cos(\omega_0 t) + e^{-\frac{2t^2}{\sigma_t^2}} \sqrt{\xi} \cos((2\omega_0 + 2\pi\delta\nu)t + \phi) \right), \quad (3.1)$$

with amplitude  $A$ , relative strength  $\xi$  and phase  $\phi$  between fundamental  $\omega_0$  and its second harmonic  $2\omega_0$ , and frequency shift  $\delta\nu$  of the second harmonic. The pulse duration  $\sigma_t$  is by a factor of  $\sqrt{2}$  smaller for the second harmonic, because the second harmonic field is usually generated by a frequency conversion process which squares the fundamental field to obtain the frequency  $2\omega_0$ . Usually the fundamental frequency lies in the optical regime, often  $\omega_0 = 2\pi \times 375$  THz or  $\lambda = 2\pi c/\omega_0 = 800$  nm and pulse durations vary in the range of tens of femtoseconds (fs).

### 3.2.2. Kerr nonlinearity

Here, we characterize the response of the gas under irradiation of an intense two-color laser pulse Equation (3.1), which is originating from the bound electrons of the neutral atoms. In particular, we are interested in contributions that lie in the THz-frequency range ( $\nu \sim 1 - 100$  THz).

The response of the gas is given by the polarization, which is split into a linear and nonlinear part

$$P(t) = P_{\text{Lin}}(t) + P_{\text{NL}}(t) \quad (3.2)$$

as introduced before (see Section 2.1). The linear part is proportional to the electric field  $\hat{E}(\omega)$

$$\hat{P}_{\text{Lin}}(\omega) = \varepsilon_0 \chi^{(1)}(\omega) \hat{E}(\omega) \quad (3.3)$$

in Fourier domain. Our pump field Equation (3.1) has only contributions at input frequencies  $\omega_0$  and  $2\omega_0$  which lie in the optical regime. Therefore, also the linear response  $\hat{P}_{\text{Lin}}$  has spectral contributions which are limited to these two optical input frequencies, making it irrelevant when considering THz radiation.

In contrast, the nonlinear polarization (see Equation (2.17)) with an assumed  $\omega$  independent, that is dispersionless  $\chi^{(3)}$  (also compare to Section 4 for a highly dispersive  $\chi^{(3)}$ )

$$P_{\text{NL}}(t) = \varepsilon_0 \chi^{(3)} E(t)^3 \quad (3.4)$$

possesses contributions in the THz range. These are created through the mechanism of sum-/difference frequency generation. For illustrative purposes, let us assume a continuous wave two color pump ( $\sigma_t \rightarrow \infty$ ,  $\delta\nu = 0$  in Equation (3.1))

$$E(t) = \frac{A}{2} (\sqrt{1-\xi} (e^{i\omega_0 t} + \text{c.c.}) + \sqrt{\xi} (e^{i(2\omega_0 t + \phi)} + \text{c.c.})), \quad (3.5)$$

where 'c.c.' means complex conjugate and plug that into Equation (3.4). Among others, we will obtain terms which read

$$P_{\text{NL}}(t) = \varepsilon_0 \chi^{(3)} \left( \frac{3}{8} A^2 A^* (1-\xi) \sqrt{\xi} e^{i((\omega_0 + \omega_0 - 2\omega_0)t - \phi)} + \text{c.c.} + \dots \right), \quad (3.6)$$

that is contributions with zero frequency  $0 = \omega_0 + \omega_0 - 2\omega_0$ . If we allow again pulsed ( $\sigma_t \sim 50 \times 10^{-15}$  s) two-color pump fields, our input pulse does not only contain the exact frequencies  $\omega_0$  and  $2\omega_0$  but also contributions in a small frequency band ( $\Delta\omega \sim 1/\sigma_t \sim 20 \times 10^{12}$  Hz  $\ll \omega_0 \sim 2 \times 10^{15}$  Hz) around these frequencies. Then,  $\omega_0 + \omega_0 - 2\omega_0$  is not exactly - but in the order of  $\Delta\omega$  close to - zero. Since we have  $\Delta\omega \sim 20 \times 10^{12}$  Hz = 20 THz, generated frequencies lie in the THz regime. The electric field created by that polarization is

$$E^{\chi^{(3)}} \propto \mu_0 \frac{\partial^2}{\partial t^2} P_{\text{NL}} \quad (3.7)$$

or written in Fourier domain (see, e.g. Equation (2.28))

$$\hat{E}^{\chi^{(3)}}(\omega) \propto \mu_0 \omega^2 \hat{P}_{\text{NL}}(\omega). \quad (3.8)$$

Thus, because the nonlinear polarization  $\hat{P}_{\text{NL}}(\omega)$  has contributions in the THz range, also the generated field has THz components.

### 3.2.3. Photo-current mechanism

In the following the second mechanism for THz generation, the photo-current mechanism, will be introduced. Again, a two-color laser pulse Equation (3.1) is focused into a gas. In the focal region, the intensity reaches values high enough to ionize the gas and free electrons are born. These electrons are then accelerated in the incident two-color electric laser field, building up a current. It turns out that the current in turn emits radiation with contributions in the THz range as a consequence of the two-color-induced temporal asymmetry of the driving laser field. Therefore, we have to model the two basic processes involved in that mechanism. First we will have a look at the ionization process, followed by the characterization of the current.

#### 3.2.3.1. Charge generation

Depending on the incident optical intensity, different photo-ionization processes are dominating. For intensities below  $I \lesssim 10^{14}$  W/cm<sup>2</sup> multi-photon and, to a lower extent, above-threshold ionization are prevailing, whereas for higher intensities tunneling or above-barrier ionization are most important [65]. In order to determine the appropriate model, the Keldysh parameter [66]  $\gamma = \omega\sqrt{2m_eU_0}/q_eA$  can be evaluated. Here  $\omega$  and  $A$  are the laser frequency and field strength,  $U_0$  the ionization potential for the medium and  $m_e$  and  $q_e$  the electron mass and charge, respectively. Physically, the Keldysh parameter compares the laser frequency  $\omega$  with the tunneling frequency of an electron  $q_eA/\sqrt{2m_eU_0}$ . Thus, for  $\gamma \ll 1$  tunnel ionization takes place whereas for  $\gamma \gg 1$  ionization is caused by a multi-photon process. The range where  $\gamma \simeq 1$  marks a intermediate regime between both processes. A schematic overview of the main ionization mechanisms is given in Figure 3.1. The multi-photon processes for  $\gamma \ll 1$  are shown in a) and c). In the multi-photon ionization mechanism in a), simultaneous absorption of  $N$  photons provides the minimal energy needed for the ionization of an electron. If more than the minimal number of photons is absorbed as depicted in c), the ionization process is referred to as above threshold ionization. The dominating ionization mechanisms for  $\gamma \gg 1$  are presented in b) and d). In the case of tunnel ionization in b), the laser potential slants the atomic potential such that the electron is able to tunnel through the barrier. For even stronger laser fields in d), the atomic potential is deformed by the laser potential strong enough that the initial electronic state energy exceeds the potential barrier.

With regard to the forthcoming treatment of spatially focused ultra-short laser pulses, we encounter the following difficulties for an appropriate choice of the ionization model. First, in the focal region, where ionization mainly takes place we deal with typical intensities  $I \gtrsim 100$  TW/cm<sup>2</sup> and therefore evaluate  $\gamma \lesssim 1$  for  $\omega_0 = 2\pi \times 375$  THz. That is, we do not meet a limiting case, where either multi-photon or tunnel ionization is dominant. Additionally, ultrashort pulses exhibit a broad spectrum, i.e. the broad range of contained frequencies leads to a broad range of the Keldysh parameter  $\gamma$ . Although there exist ionization rates for a broad interval of  $\gamma$ , an exact

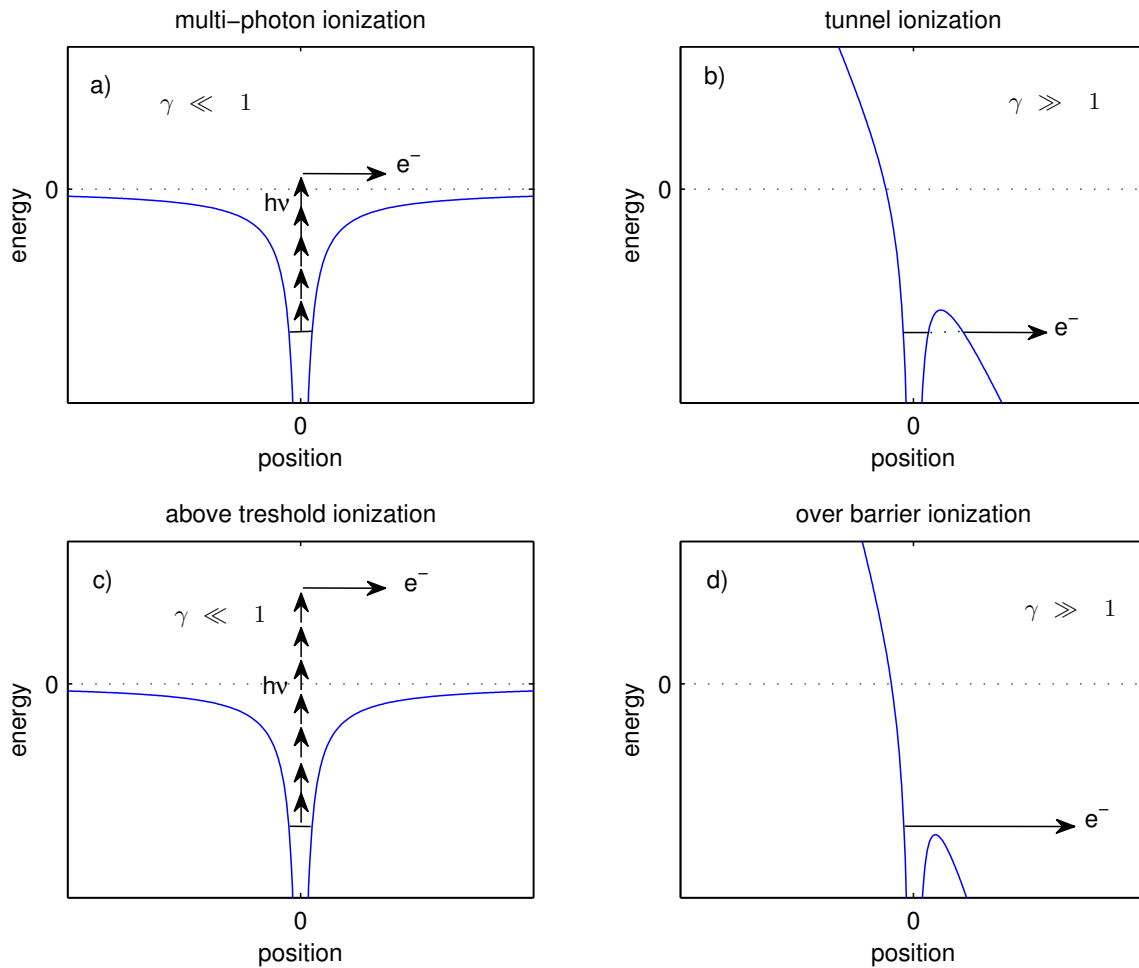


**Figure 3.1.:** Schematic illustration of basic ionization processes for different regimes of the Keldysh parameter  $\gamma$ . a) for multi-photon ionization, the minimal number  $N$  of photons to provide the ionization energy is absorbed. c) in the above threshold ionization process more than  $N$  photons are absorbed simultaneously. b) shows a slanted atomic potential with a barrier narrow enough for the electron to tunnel out. In d) the atomic potential is heavily deformed, such that the energy of the formerly bound electron exceeds the height of the barrier.

analytical description for the general case is not possible and the inclusion in a laser pulse propagation equation turns out numerically intractable ([67], also compare to Section 5 for quantum mechanical treatment of ionization). Therefore, we have to choose a model, which is suited to be included in the forthcoming laser pulse propagation equation but gives at least qualitatively correct results and matching orders of magnitude. Fortunately, for our typical intensities of  $I \simeq 100 \text{ TW/cm}^2$  a stepwise increase of the charge density was reported experimentally [68, 69]. Such a stepwise increase turns out to be a crucial feature for THz generation. In the following, we will use a tunnel ionization model, since a stepwise increase of the charge density is characteristic for these models.

There exist two different models describing the tunnel ionization, that is the quasi-static tunneling model [70] and the Ammosov-Delone-Krainov (ADK) tunneling model [71]. For a given atomic ionization potential, the ADK model additionally distinguishes different angular momentum quantum numbers in its ionization rate, whereas the rate for quasi-static tunneling does not. Nevertheless, it was shown [27], that both rates show the same qualitative dependence on the incident field strength, and even quantitatively agree within a factor of two.

In this work, we use the quasi-static tunneling rate. The rate is applicable for s-state electrons in hydrogen-like atoms and can be obtained by solving the atomic Schrödinger equation. Thereby, the most significant approximation is incurred by matching the electronic wave function within the potential barrier with a semi-classical plane wave outside the barrier [72] and one obtains

$$w_{\text{st}}(E(t)) = 4\omega_a r_H^{5/2} \frac{E_a}{|E(t)|} \exp\left(-\frac{2r_H^{3/2} E_a}{3|E(t)|}\right), \quad (3.9)$$

where  $E_a = m_e^2 q_e^5 / (4\pi\epsilon_0)^3 \hbar^4$  is the atomic field strength,  $\omega_a = m_e q_e^4 / (4\pi\epsilon_0)^2 \hbar^3$  the atomic frequency and  $r_H = U_{\text{At}}/U_{\text{H}}$ , with  $U_{\text{At}}$  and  $U_{\text{H}}$  the ionization potential of the medium under consideration and hydrogen, respectively. Then, the density of free electrons  $\rho_e$  which are created obeys

$$\partial_t \rho_e(t) = w_{\text{st}}(E(t)) (\rho_{\text{at}} - \rho_e(t)), \quad (3.10)$$

with  $\rho_{\text{at}}$  the atomic number density.

Figure 3.2 a) illustrates the strong nonlinear dependence of the ionization rate Equation (3.9) on the field strength. This dependency leads to the fact, that ionization mainly occurs at instants of time when the field is maximal. These maxima are separated in time, which leads to a stepwise increase of the electron density at these instants of time (see Figure 3.2 b)) to which we will refer as ionization events in the following. These discrete and well defined moments of ionization are important for the properties of the electron current, which is introduced in the next section.



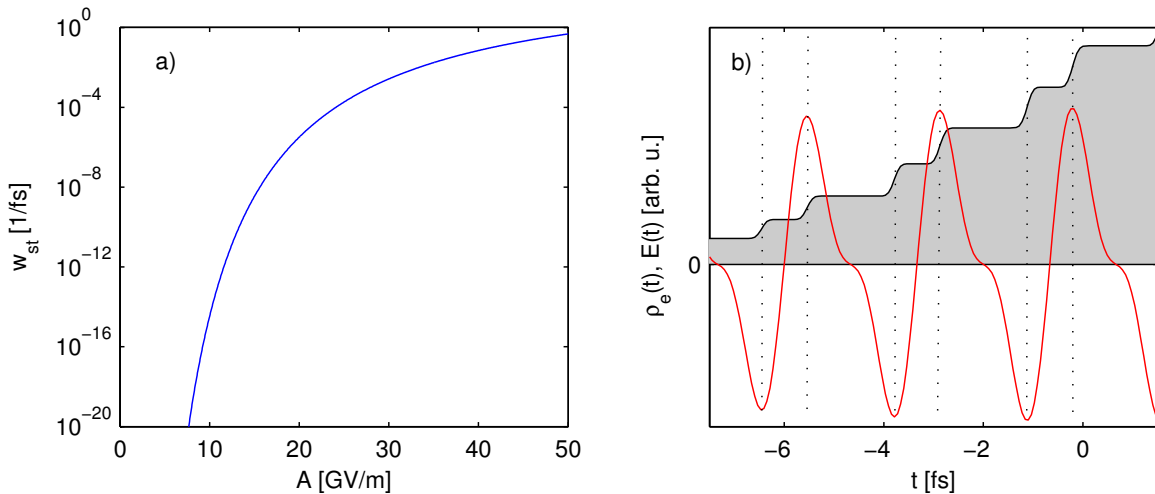


**Figure 3.2.:** (a) strong nonlinear dependence of the quasi-static tunnel ionization rate  $w_{st}$  on the electric field amplitude  $A$ . (b) ionization mainly occurs at field (red line) maxima, leading to a stepwise modulation of the electron density  $\rho_e$  (shaded gray area). We used an input field  $E(t)$  given by Equation (3.1) with  $A = 33$  GV/m,  $\sigma_t = 24$  fs,  $\phi = \pi/2$  and  $\xi = 0.16$ .

### 3.2.3.2. Equation for the current

Let us detail the macroscopic description of the current. After being born in the ionization process, the newly generated electrons are assumed to have zero velocity. This is based on the fact, that we deal with an ionization process which is just in between multi-photon and tunnel ionization. In the multi-photon picture, the electron absorbs the minimal number of photons to escape the binding potential, having only a small energy excess, e.g. small kinetic energy. In the tunneling ionization picture, the electron tunnels through a rather broad barrier and just reaches the unbound region, thus again exhibiting small kinetic energy. For a first illustration, we neglect any interaction of the electrons with each other or with the ions. Then, we suppose to generate  $d\rho_e(t_0) = \partial_{t_0}\rho_e(t_0)dt_0$  electrons at time  $t_0$ . At a later time  $t > t_0$  these electrons have the velocity  $v(t, t_0)$ , thus the contribution to the current is  $v(t, t_0) d\rho_e(t_0)$ . The overall current is then obtained by integrating over all initial times  $t_0$  [27–29]:

$$J(t) = q_e \int_{-\infty}^t v(t, t_0) \partial_{t_0}\rho_e(t_0) dt_0. \quad (3.11)$$

Since the electrons are assumed to be non-interacting and non-relativistic, they are only accelerated by the laser field

$$\frac{dv(t, t_0)}{dt} = \frac{q_e}{m_e} E(t) \quad (3.12)$$

and due to zero velocity at  $t_0$  the velocity expresses as

$$v(t, t_0) = \frac{q_e}{m_e} \int_{t_0}^t E(\tau) d\tau = \tilde{v}(t) - \tilde{v}(t_0), \quad (3.13)$$

where we introduced

$$\tilde{v}(t) \equiv v(t, -\infty) = \frac{q_e}{m_e} \int_{-\infty}^t E(\tau) d\tau \quad (3.14)$$

Plugging that in Equation (3.11) gives

$$J(t) = q_e \int_{-\infty}^t [\tilde{v}(t) - \tilde{v}(t_0)] \partial_{t_0} \rho_e(t_0) dt_0 \quad (3.15)$$

$$= q_e \tilde{v}(t) \rho_e(t) - q_e \int_{-\infty}^t \tilde{v}(t_0) \partial_{t_0} \rho_e(t_0) dt_0 \quad (3.16)$$

Finally, taking the derivative with respect to time gives

$$\dot{J}(t) = q_e [\dot{\tilde{v}}(t) \rho_e(t) + \tilde{v}(t) \dot{\rho}_e(t)] - q_e \tilde{v}(t) \dot{\rho}_e(t) = q_e \dot{\tilde{v}}(t) \rho_e(t) \quad (3.17)$$

and using Equation (3.14) results in

$$\dot{J}(t) = \frac{q_e^2}{m_e} E(t) \rho_e(t). \quad (3.18)$$

So far we did not take the interaction between electrons and ions into account. First of all, we can neglect the coulomb interaction between electrons and ions, since the electrons move in the homogeneous background of the positively charged ions. However, there has to be a source of damping of the current  $J(t)$ , otherwise we would obtain infinitely long lasting currents (see Figure 3.4 b)). Such an unphysical behavior leads to a constant electric field and is also intractable numerically. For our current, damping arises from electron-ion recombination or electron-ion collisions and depends on the density of electrons and ions, the amplitude and frequency of the electric field and the velocity of electrons [73]. On the macroscopic level we describe our current on, these mechanisms are accounted for on a phenomenological basis in terms of rate equations [74]. Then, the cross sections for collisions or recombination translate into average interaction times. It turns out that the electron ion recombination occurs on a timescale of nanoseconds, thus is of minor influence for frequencies in the THz range [52, 74, 75]. In contrast, electron-ion collision occurs in the order of  $\tau_c = 200$  fs ( $1/\tau_c = 5$  THz) and therefore will be accounted for in the following [73, 76]. Note that the timescale for damping is larger than typical pulse durations. That is, damping influences the low frequency part of upcoming spectra, which lies below the accessible spectral range of radiation that is generated during the interaction of the pulse with the gas. Our main interest is this high frequency part of the spectrum, thus the precise value of our anyways only phenomenological  $\tau_c$  is of minor importance.

Due to the collisions, Equation (3.12) is modified

$$\frac{dv(t, t_0)}{dt} = \frac{q_e}{m_e} E(t) - \frac{1}{\tau_c} v(t, t_0). \quad (3.19)$$

Introducing a new variable  $v'$  for velocity

$$v'(t, t_0) = v(t, t_0) \exp\left(\frac{1}{\tau_c} t\right) \quad (3.20)$$

transforms Equation (3.19) into

$$\frac{dv'(t, t_0)}{dt} = \frac{q_e}{m_e} E(t) \exp\left(\frac{1}{\tau_c} t\right). \quad (3.21)$$

Integrating and returning to the original variable  $v(t, t_0)$  gives

$$v(t, t_0) = \frac{q_e}{m_e} \int_{t_0}^t E(\tau) \exp\left(\frac{1}{\tau_c}(\tau - t)\right) d\tau. \quad (3.22)$$

Repeating the above steps Equation (3.14) - (3.17) leads to the current equation analogue to Equation (3.18)

$$\dot{J}(t) + \frac{1}{\tau_c} J(t) = \frac{q_e^2}{m_e} E(t) \rho_e(t). \quad (3.23)$$

We now want to demonstrate that with a two color input field we have current contributions which lie in the THz range. We proceed in two steps. In the first step, we consider the current of the electrons which are generated at one single ionization event. The second step then takes all ionization events into account.

Let us start with considering the dynamics of electrons from a single ionization event, that is of electrons born at one single field maximum. For demonstration purposes, we assume the convenient case of  $\tau_c \gg \sigma_t$ . Since for one single ionization event the amount of generated electrons is fixed, the current is completely characterized by the electron velocity. Figure 3.3(a) shows a one color ( $\xi = 0$ ) input field (red line) and the velocity of electrons generated at the field maxima at  $t = 0$  (blue line). It is evident, that the initially resting electrons are accelerated, exhibiting a velocity alternating with the frequency of the electric input field. After the pulse, they are at rest again as long as the pulse duration  $\sigma_t$  is considerably larger than the period of one optical cycle  $T = 2\pi/\omega_0$  of the input pulse. Figure 3.3(b) details the two-color ( $\xi = 0.2, \phi = \pi/2$ ) case for electrons generated at  $t = 0$ . Again, the initially resting electrons are accelerated, acquiring a velocity alternating with the frequency(s) of the electric field. In contrast to the former example, at the end of the pulse, a nonzero electron velocity remains, which is due to the temporally asymmetric shape of the electric field, introduced by the second frequency. Obviously, this velocity is built up

on the timescale of the pulse duration  $\sigma_t$  and will relax to zero on the electron-ion collision timescale  $\tau_c$  according to Equation (3.19). That means, in the two color case the velocity does not only contain the frequencies of the pump field, but additional contributions in the order of  $1/\sigma_t$  and  $1/\tau_c$ . For typical parameters, e.g.  $\tau_c = 200$  fs and  $\sigma_t = 25$  fs, these contributions lie in the THz range.

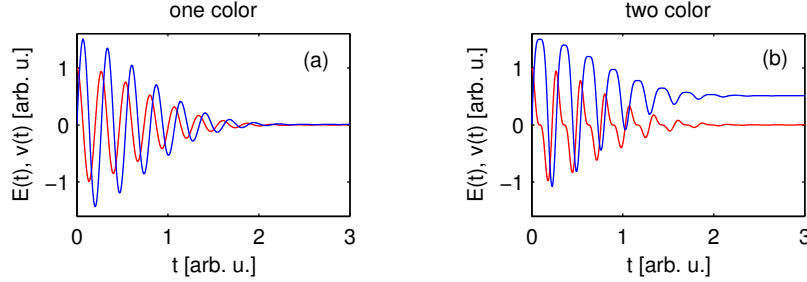


**Figure 3.3.:** (a) One color input field ( $\xi = 0$ , red line). Only electrons generated at the field maximum at  $t = 0$  are considered. Their velocity (blue line) is zero after the pulse. (b) The temporally asymmetric two-color input field ( $\xi = 0.2$  and  $\phi = \pi/2$ , red line) leads to non-zero velocity (blue line) of electrons that are born at time  $t = 0$ .

Going over to consider not only the current contribution from one single ionization event, but taking into account all contributions from the pump pulse preserves the above characteristics. We consider the current for a one color input field in Figure 3.4(a): the overall current follows the one color field and at the end of the pulse no current remains. In the two color case Figure 3.4(b), the current also follows the electric field, but after the pulse, a non-zero current contribution remains. Again, pulse duration  $\sigma_t$  and ion-electron collision time  $\tau_c$  are the relevant time-scales.

The crucial effect is emphasized, when considering the electric fields radiated by these currents. They are given by [77]

$$E^J \propto \mu_0 \partial_t J(t) \quad (3.24)$$

in time domain or

$$\hat{E}^J \propto \mu_0 \omega \hat{J}(\omega) \quad (3.25)$$

in Fourier domain. The spectrum of the input (red line) and radiated (blue line) field is presented for the one color case in Figure 3.4(c), clearly showing that the radiated field has the same spectral components as the input field. In contrast the situation for the two-color input field in Figure 3.4(d): Here, the radiated field does not only have contributions at the frequencies contained in the input pulse, but also in the THz range. In the following, we will term the radiated fields Equations (3.24) and (3.25) local spectra. In Section 3.4 these local spectra are the fundamental constituents for spectra from extended sources as they reappear in forward direction. Thus, local spectra deserve their detailed analysis in the next section.

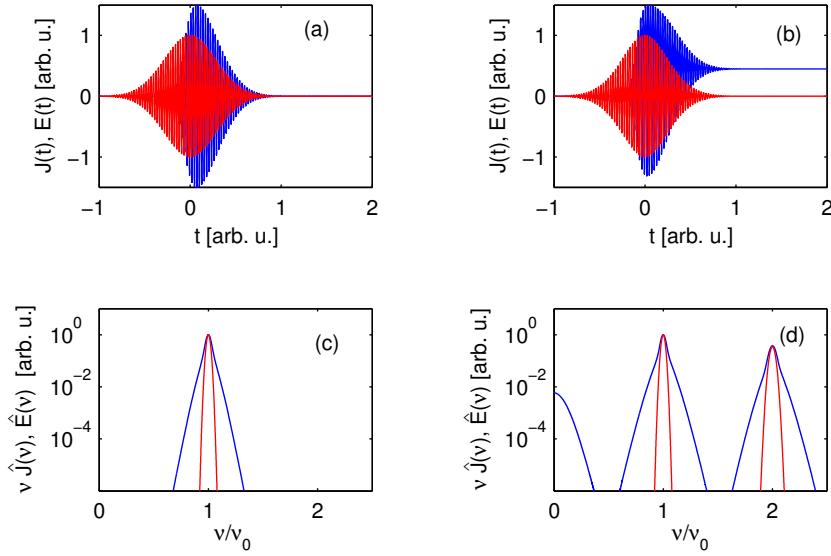


**Figure 3.4.:** Comparison of the current (for  $\tau_c \rightarrow \infty$ ) for one ( $\xi = 0$ ) and two-color ( $\xi = 0$ ,  $\phi = \pi/2$ ) input fields in time- and Fourier-domain. In (a) the one color input field (red line) causes a zero current (blue line) after the pulse. In Fourier domain c), the spectrum of the radiated field (blue line) has the same spectral contributions at the fundamental frequency  $\nu_0$  as the input field (red line). b) depicts the two-color input field (red line). The created current (blue line) persists after the pulse. d) The two-color input field has spectral contributions at the fundamental  $\nu_0$  and second harmonic  $2\nu_0$  (red line). The radiated field (blue line) additionally has low frequency contributions in the THz regime.

### 3.3. Local terahertz spectra

In the preceding section, we explained the physical mechanism that leads to radiation in the THz range. In the following, we want to characterize that radiation. As before, we stay in the local approximation with a purely time dependent two-color input field Equation (3.1). Our investigation will be split into two parts. In the first Section 3.3.1, we characterize the dependency of the spectra on the pump on an observational level. For example, we will see that the THz generation process via a  $\chi^{(3)}$  nonlinearity is negligible compared to the photo current process. Thus, the second Section 3.3.2 exclusively deals with an analytical description of the spectral properties within the photo-current framework. Hereby, we will actually elucidate the physical mechanism responsible for the THz emission.

#### 3.3.1. Generic dependencies

The two-color input field Equation (3.1) is characterized by the pulse amplitude  $A$ , pulse duration  $\sigma_t$ , the relative strength  $\xi$  and phase  $\phi$  of fundamental  $\omega_0$  and second harmonic  $2\omega_0$  and by possible frequency shifts  $\delta\nu$  in the second harmonic. In the following, we analyze effects of changes in these parameters on the emitted spectrum.

##### 3.3.1.1. Kerr nonlinearity vs. photo-current

Let us start with the illustration of the THz generation by a two-color current as presented in Section 3.2.3 prevailing over the generation via Kerr nonlinearity described in Section 3.2.2. We consider the radiated electric field (local spectra) for both cases. For the Kerr process the local spectrum is given by Equation (3.8). The emitted field of the two-color photo-current obeys Equation (3.25). We compare the overall yield in the THz regime

$$Y_{\text{THz}}^{J/\chi^{(3)}} = \int_0^{2\pi \times 100\text{THz}} |\hat{E}^{J/\chi^{(3)}}(\omega)|^2 d\omega \quad (3.26)$$

depending on relative strength  $\xi$ , relative phase  $\phi$  and amplitude  $A$  of our input pulse with  $\delta\nu = 0$ .

The THz yield  $Y_{\text{THz}}^{\chi^{(3)}}$  for the Kerr mechanism is shown in the left column of Figure 3.5 for different input pulse amplitudes  $A$ . For all input amplitudes  $A$ , the yield is maximal for  $\xi \approx 0.3$  and  $\phi \approx 0, \pi$ , whereas a clear minimum of the yield is observed for  $\phi = \pi/2$ . This behavior can be explained by analyzing Equation (3.6), which characterizes the nonlinear polarization as source of the radiated field: For maximum yield, the relative strength  $\xi$  of fundamental  $\omega_0$  and second harmonic  $2\omega_0$  has to be chosen  $\xi = 1/3$  in order to maximize the coefficient  $(1 - \xi)\sqrt{\xi}$ . Additionally, the exponential term is maximal for  $\phi = 0, \pi, 2\pi, \dots$  for long input pulses. Finally, increasing the input field strengths  $A$  leads to increased emission of THz radiation. This is only limited by the fact, that eventually the medium gets ionized and the pure Kerr description becomes incorrect (see Section 5).

In the right column of Figure 3.5, the THz yield  $Y_{THz}^J$  for the photo-current mechanism is presented. For low input amplitude of  $A = 10$  GV/m in b) we observe maximum yield for  $\xi \approx 0.5$  and  $\phi \approx 0, \pi$ . For increasing input amplitude  $A$  in d), f), h) this optimum value for  $\phi$  shifts continuously to  $\phi = \pi/2$  for  $A \gtrsim 50$  GV/m. This reveals a two step character of THz generation: First, the charge is generated and secondly accelerated in the laser field. That is already indicated in Equation (3.15), where the radiating current is proportional to the amount of ionized electrons  $\rho_e$ . So for low input amplitudes, the effective generation of charge is more important than the subsequent acceleration. The amount of generated charge depends on the ionization rate, which is highly nonlinear in the input field amplitude (recall Figure 3.2). Since the field maximum for a fixed amplitude  $A$  is highest for  $\phi \approx 0, \pi$ , the optimal THz yield is reached for these values of  $\phi$ . For high input amplitudes  $A$  the medium is almost completely ionized for every  $\phi$ , such that the optimal yield can be found when the current is optimized, that is for  $\phi = \pi/2$ . An explanation for this behavior is given in the next Section, where we analytically describe THz generation. Above all, note the differences of several orders of magnitude in the yield amplitude for the different input amplitudes. We further observe saturation, when comparing the amplification of the maximum yield by a factor of  $10^8$  for doubling the input amplitude from  $A = 20$  GV/m to  $A = 50$  GV/m with an amplification factor of only 2 when increasing from  $A = 50$  GV/m to  $A = 100$  GV/m. Again, it can be argued, that the medium is almost completely ionized for amplitudes  $A > 50$  GV/m making the effect of additionally generated charge for even further increased amplitudes negligible.

Let us finally directly compare the THz yield of the Kerr mechanism with the yield of the photo-current. Only for a low input amplitude  $A = 10$  GV/m in a) and b) the amplitude of the yield from Kerr mechanism is larger than the one from the photo-current. Already for  $A = 20$  GV/m in c) and d) we encounter the opposite situation, which becomes even clearer for  $A \gtrsim 50$  GV/m in e)-h) when the yield of the photo-current mechanism exceeds the yield from the Kerr mechanism by several orders of magnitude. This fact is further confirmed in References [25, 26]. In the following, our input amplitudes will be well above  $A \gtrsim 20$  GV/m, which allows us to neglect Kerr contributions when considering THz generation in the two-color setup.

In summary, for an effective generation of THz radiation, we have to provide sufficiently high input amplitudes, which assure ionization of the medium. For the example of argon gas that we used here, this amplitude is in the order of  $A = 50$  GV/m. For such high amplitudes, we can neglect Kerr contributions to the THz yield, since they are exceeded by the highest yield from the photo-current mechanism at  $\xi = 0.5$  and  $\phi = \pi/2$  by several orders of magnitude.

### 3.3.1.2. Spectral shapes

As reasoned above, we restrict ourselves to the analysis of the THz radiation within the photo-current framework. Up to now, we considered the yield in the THz regime, that is the integrated spectra of the radiated field. We now characterize the spectrum

### 3. Terahertz Generation by Ionizing Two-Color Laser Pulses

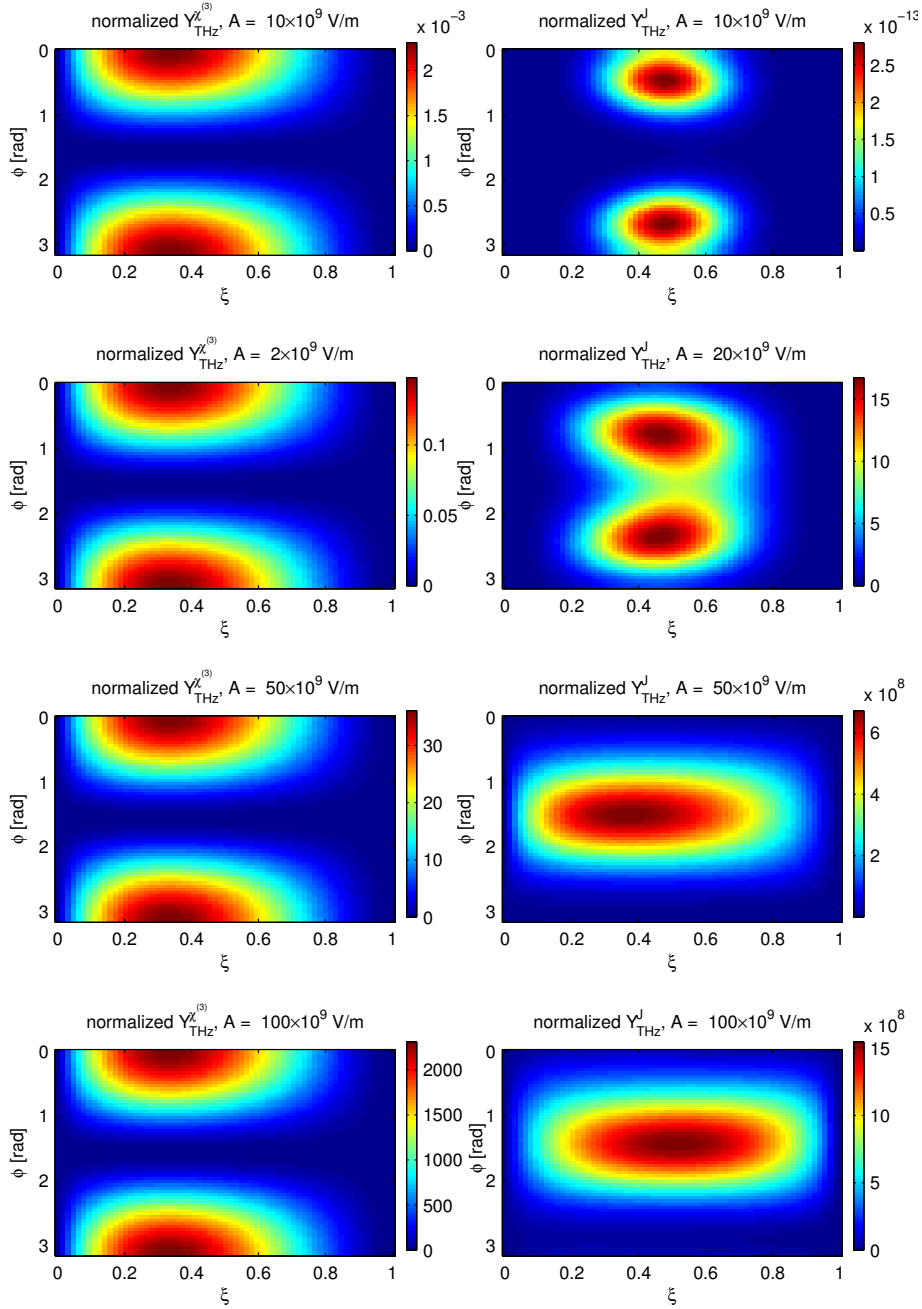


**Figure 3.5.:** The THz yield  $Y_{THz}^{J/\chi^{(3)}}$  for an input pulse with duration  $\sigma_t = 40$  fs and frequency shift  $\delta\nu = 0$  depends on the relative strength  $\xi$  and phase  $\phi$  of fundamental and second harmonic. The yield  $Y_{THz}^{\chi^{(3)}}$  for the Kerr process via  $\chi^{(3)}$  in a), c), e), and g) is optimal for  $\xi = 0.3$  and  $\phi = 0, \pi$  for all input amplitudes  $A$ . The qualitative change of optimal yield  $Y_{THz}^J$  for the photo-current mechanism in b), d) and f) goes along with an increase of the maximal yield over several orders of magnitude. For high input amplitudes  $A \gtrsim 50$  GV/m in f) and h) the optimum for  $Y_{THz}^J$  can be found for  $\xi = 0.5$  and  $\phi = \pi/2$  and is orders of magnitude larger than the yield for the Kerr process in e) and g). All values are normalized to  $Y_{THz}^{\chi^{(3)}}$  for an input pulse with  $A = 27$  GV/m,  $\sigma_t = 40$  fs,  $\xi = 1/3$  and  $\phi = 0$ .



$\hat{E}^J(\omega)$  itself. For that, we fix the relative strength to  $\xi = 0.5$ , the relative phase to  $\phi = \pi/2$  and apply amplitudes of  $A \gtrsim 40$  GV/m, since the yield is optimal for these values, as learned above.

Figure 3.6 shows the spectra in the THz regime for frequencies up to  $\nu = \omega/2\pi = 100$  THz for two different pulse durations  $\sigma_t = 25$  fs in a) and  $\sigma_t = 50$  fs in b) and for different input amplitudes  $A$ . The maxima of the spectra are at  $\nu \approx 8$  THz for both cases. Obviously, the spectrum is much broader for the setup with  $\sigma_t = 25$  fs (half maximum at  $\nu \approx 50$  THz at  $A = 60$  GV/m) than in the  $\sigma_t = 50$  fs case (half maximum at  $\nu \approx 30$  THz at  $A = 60$  GV/m). An explanation is given in the next chapter. However, the singly peaked spectral shape is the same for both setups.

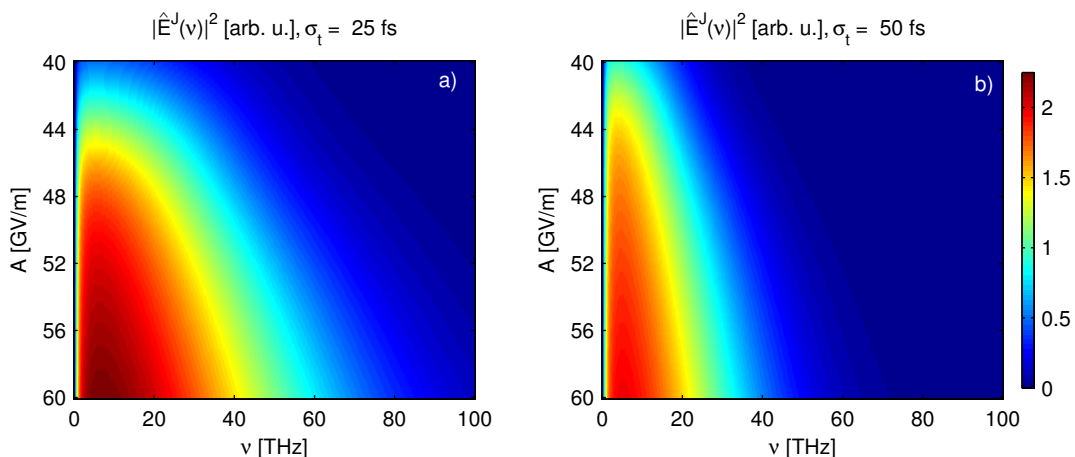


**Figure 3.6.:** Spectral intensity  $|\hat{E}^J(\nu)|^2$  for different input pulse amplitudes  $A$  and input pulse durations of a)  $\sigma_t = 25$  fs and b)  $\sigma_t = 25$  fs. Using the same color scale reveals much broader spectra for  $\sigma_t = 25$  fs in a) than for  $\sigma_t = 50$  fs in b). We used  $\xi = 0.5$  and  $\phi = \pi/2$  for both cases a) and b).

Let us now detail on the just observed dependence of the spectral width on the input pulse duration. Again, we fix the relative strength to  $\xi = 0.5$ , the relative phase to  $\phi = \pi/2$  and investigate the dependence of the spectra on the input pulse duration for typical amplitudes  $A$ . For input amplitude  $A = 40$  GV/m (Figure 3.7 a)) we have broad spectra with small amplitude for short pulse durations, which continuously evolve into narrow, but peaked spectra with higher maximal amplitude for pulse durations  $\sigma_t > 50$  fs. This qualitatively changes for increasing amplitude  $A$  in b), c). For  $A = 50$  GV/m (Figure 3.7 d)) the spectral width still decreases for increasing pulse duration, but the maximal spectral amplitude can no longer be found for longest pulse durations, but for  $\sigma_t \approx 25$  fs. Nevertheless, as already indicated in Figure 3.6, the main feature is the inverse proportionality of increasing spectral width for decreasing pulse durations. Thus, when thinking in terms of integrated spectra, we obtain smaller yield for longer pulse duration, although the input pulse carries more energy for longer pulse duration. That unintuitive behavior is explained in the next

## Section 3.3.2.

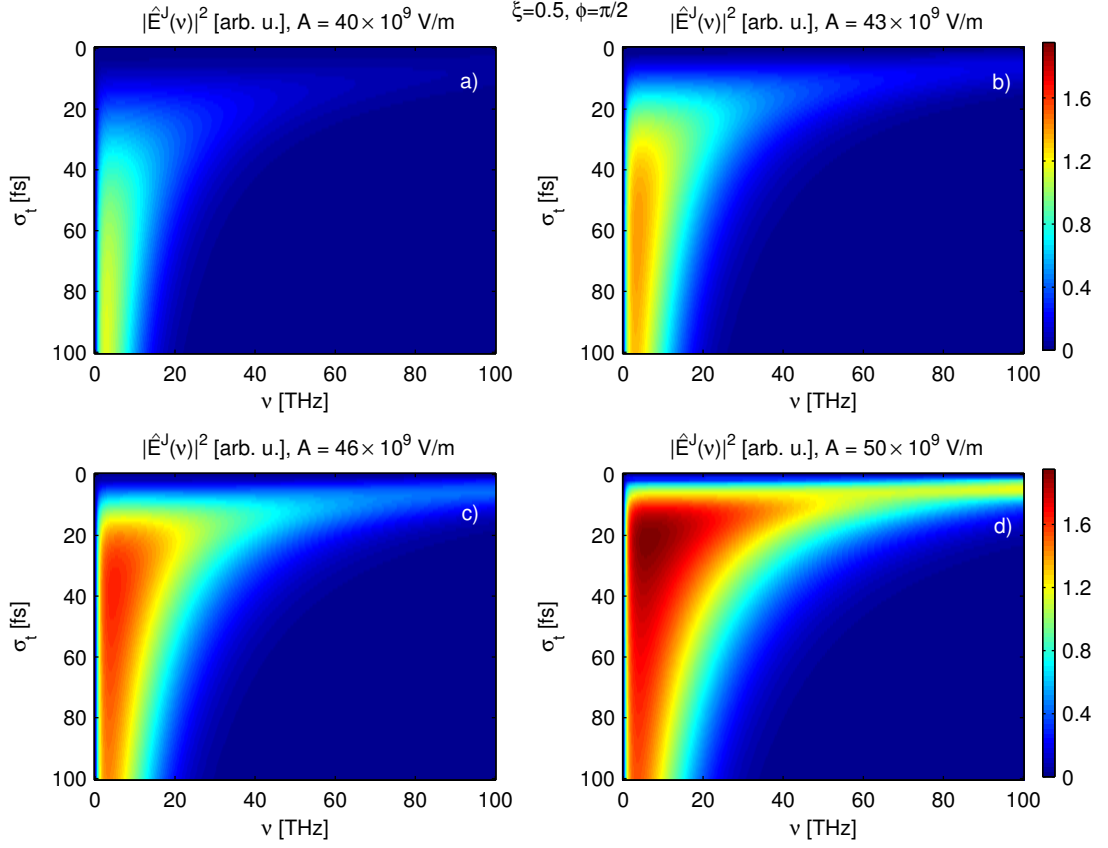


**Figure 3.7.:** Spectral intensity  $|\hat{E}^J(\nu)|^2$  for different input pulse durations  $\sigma_t$  and input pulse amplitudes  $A$ . The spectral width in a)-d) is inversely proportional to the input pulse duration. In d) the maximal spectral intensity clearly features a maximum around  $\sigma_t = 25$  fs, in contrast to a)-c) where it stays rather constant over a broad range of  $\sigma_t$ .

Finally, we want to get an impression of how small detunings  $\delta\nu$  between fundamental and second harmonic affect the spectral shapes. Without loss of generality, we impose the detuning on the second harmonic. The results are shown in Figure 3.8, where we varied the second harmonic frequency  $2\omega_0 + 2\pi\delta\nu$  for  $\delta\nu = -30\text{THz} \dots + 30\text{THz}$ , with anticipated values for  $\delta\nu$  from observations in Section 3.5.3. In Figure 3.8 a), we observe a clear asymmetry. For positive  $\delta\nu$  the spectrum gets depleted, whereas it shifts its peak to higher frequencies for negative  $\delta\nu$ . With increasing input amplitude, this effect weakens. Again, Section 3.3.2 details on that observation.

In this section, we studied the dependencies of THz spectra radiated by a two-color current on the parameters of the two color input field by means of observations. In the first part, we learned that choosing a relative amplitude  $\xi = 0.5$  and relative phase  $\phi = \pi/2$  ensures optimal THz yield for high enough input amplitudes, in our

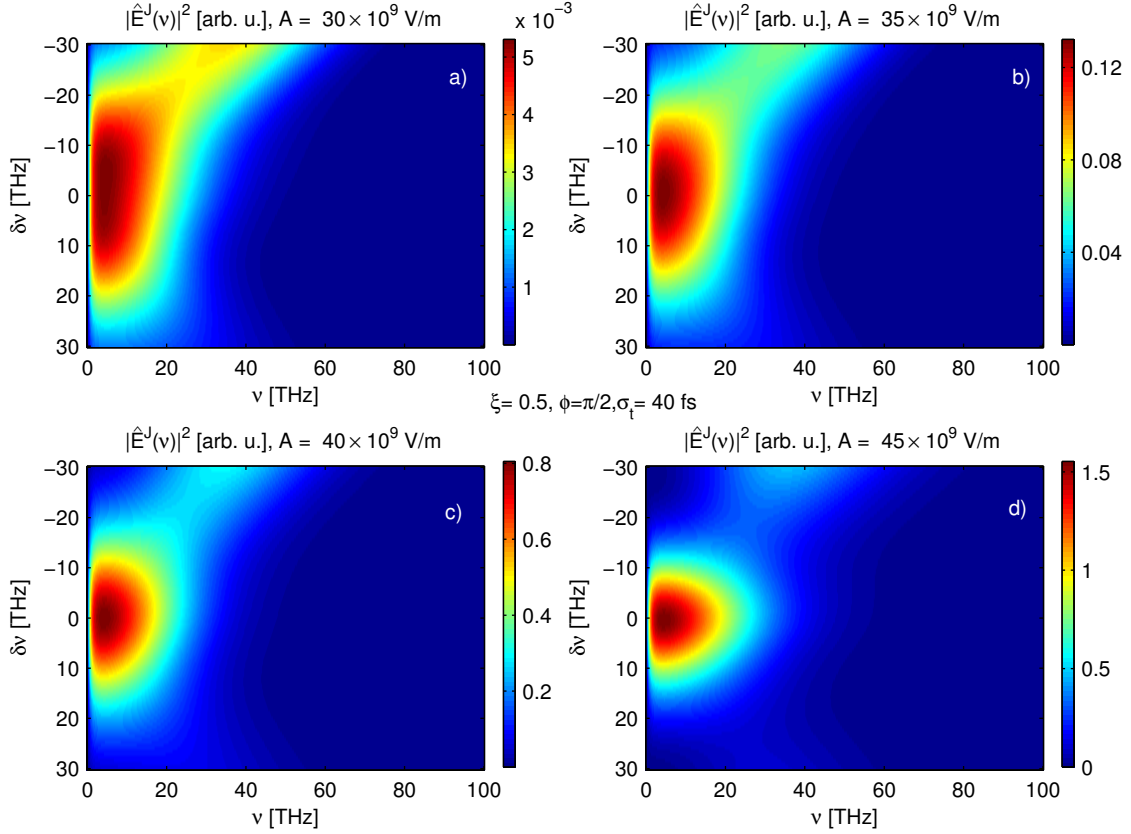


**Figure 3.8.:** The Spectral intensity  $|\hat{E}^J(\nu)|^2$  for different input pulse amplitudes  $A$  depends on small frequency shifts  $\delta\nu$  in the second harmonic. This dependence is asymmetric with regard to the sign of  $\delta\nu$ . For negative values the spectral maximum shifts to higher frequencies, whereas the spectrum gets depleted for positive  $\delta\nu$ . This clearly visible effect in a) and b) weakens for higher input field amplitudes  $A$  in c), d).

case  $A \gtrsim 50$  THz for argon gas. After fixing  $\xi = 0.5$  and  $\phi = \pi/2$  to their optimal values, we further revealed the spectra to have their maxima at frequency of  $\approx 8$  THz and a width inversely proportional to the input pulse duration. That is, short pulse durations ensure a large yield. However, these considerations do not reveal the physical mechanisms responsible for the observations. That is the aim of the following chapter.

### 3.3.2. Analytical spectral shapes

In this chapter, we want to reveal the physical mechanism responsible for the observations presented above. We resort to the photo-current mechanism for THz generation and our aim is the analytical description of the radiated field of the two-color current. For clarity, we repeat the main steps of THz generation by the photo-current. First, our two-color input field generates charge through ionization of the medium. This charge is accelerated in the present two-color field, building up a current. The resulting current emits radiation, with contributions in THz regime. For an analytical description, the steps we have to undertake are obvious: First, we derive a reasonable analytical approximation for the input field. Then, we are able to infer approximate expressions for the generated charge and subsequently for the current. Finally, we obtain results for the local spectra of the radiated field [78].

We stay in our local approximation of an input field depending exclusively on time. For mathematical convenience, we assume a slightly different two-color input pulse than Equation (3.1):

$$E(t) = \mathcal{E}(t) \left[ \cos(\omega_0 t) + \sqrt{r} \cos(2\omega_0 t + \phi) \right], \quad (3.27)$$

where  $\mathcal{E}(t)$  is a Gaussian envelope. We model charge generation by tunnel ionization, the respective ionization rate we recall from Equation (3.9) in Section 3.2.3.1

$$w_{\text{st}}(E) = 4\omega_a r_H^{5/2} \frac{E_a}{|E|} \exp\left(-\frac{2r_H^{3/2} E_a}{3|E|}\right). \quad (3.28)$$

We also know, that the charge obeys

$$\partial_t \rho_e(t) = w_{\text{st}}(E) (\rho_{\text{at}} - \rho_e(t)) \quad (3.29)$$

and increases stepwise at the instants of time  $t_n$ , where the field is maximal (see Figure 3.9). We recall, that this stepwise increase of the charge at separated instants of time was experimentally observed for intensities around 100 TW/cm<sup>2</sup> (amplitude  $\sim 30$  GV/m) [68,69], since this stepwise character is the crucial feature in the following. For the field given in Equation (3.27) the ionization events occur at times

$$\omega_0 t_n \approx \pi n - 2(-1)^n r \sin(\phi). \quad (3.30)$$

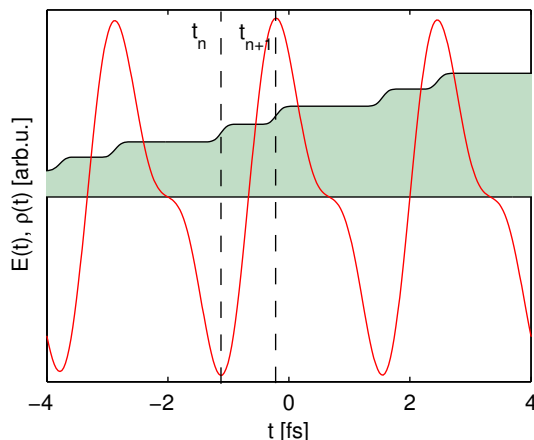


**Figure 3.9.:** Schematic illustration of the two-color input field (red line) and the generated charge (filled green area). The charge increases in  $\simeq 200$  attoseconds long steps located at times  $t_n$ , when the input field has a maximal absolute value.

Around these times  $t_n$ , the maxima of the field can be approximated by its Taylor expansion

$$E(t) \approx E_0 + E_2(t - t_n)^2 \quad (3.31)$$

with  $E_0 = E(t_n)$  and  $E_2 = \partial_{tt}E(t_n)/2$ . Using this approximate expression for the field and assuming  $\rho_{at} \gg \rho$  in Equation (3.29), we can express the ionization rate  $w_{st}$  as

$$w_{st}(E(t)) \approx w_{st}(E(t_n)) \exp(-\sigma^2(t - t_n)^2/4) \quad (3.32)$$

with  $\sigma = 8r_H^{3/2} E_a |E_2|/3|E_0|^2$ . Of course,  $\sigma$  varies for different single ionization events at different  $t_n$ . However, these deviations are on the percent level, thus we assume a typical value of  $\sigma = 10 \text{ fs}^{-1}$  from now on. We use this universal  $\sigma$  in Equation (3.29) for the charge and obtain

$$\rho(t) = \sum_n \delta\rho_n H(t - t_n) \quad (3.33)$$

with

$$H(t - t_n) \propto \int_{-\infty}^t \exp(\sigma^2(\tau - t_n)^2/4) d\tau \propto \frac{1}{\sigma} \left[ 1 + \operatorname{erf} \left( \frac{\sigma(t - t_n)}{2} \right) \right]. \quad (3.34)$$

That is, the charge is a superposition of contributions from single ionization events, each having an amplitude  $\delta\rho_n$  and the shape  $H(t - t_n)$ . This shape is assumed to be the same for all ionization events in our approximation. The current reads (see Equation (3.11) and (3.22) from Section 3.2.3.1, also [79])

$$J(t) = q \int_{-\infty}^t [\partial_\tau \rho(\tau)] [v(t) - e^{1/\tau_c(\tau-t)} v(\tau)] d\tau. \quad (3.35)$$

Including the charge from Equation (3.33) transforms this expression into

$$J(t) \cong q \sum_n \delta\rho_n H(t - t_n) [v(t) - e^{1/\tau_c(t_n-t)} v(t_n)] d\tau. \quad (3.36)$$

The field radiated by a current is given by Jefimenko's equation ([77], also Section 3.2.3.2), which reads in Fourier space

$$\hat{E}^J(\omega) = gi\omega\hat{J}(\omega), \quad (3.37)$$

with  $g = \frac{\Delta V}{4\pi\epsilon_0 c^2 r} \exp(i\omega \frac{r}{c})$ . Here,  $\Delta V$  is the small gas volume we consider in our local current approximation and  $r$  is the distance between emission and recording of the radiated field. Plugging in our approximated current Equation (3.36) gives for the emitted field

$$\hat{E}^J(\omega) = \sum_n [\hat{A}_n(\omega) - C_n \hat{B}(\omega)] e^{i\omega t_n}, \quad (3.38)$$

with

$$\hat{A}_n(\omega) = -iq_e g \omega \delta\rho_n \mathcal{FT} \{H(t)v(t + t_n)\}, \quad (3.39)$$

$$\hat{B}(\omega) = -ig\omega \mathcal{FT} \{H(t)e^{-t/\tau_c}\}, \quad (3.40)$$

$$C_n = q_e \delta\rho_n v(t_n), \quad (3.41)$$

where  $\mathcal{FT}$  means Fourier transformation. Obviously, the superposition of ionization events in the charge density carries over to the radiated field. According to Equation (3.38) the radiated field's total spectrum is composed of a linear superposition of contributions  $[\hat{A}_n(\omega) - C_n \hat{B}(\omega)] \exp(i\omega t_n)$ , which are radiated by a single ionization event at  $t_n$ . This is illustrated in Figure 3.10 a). The red shaded line represents the total spectrum  $\hat{E}^J(\omega)$ . It is the sum of partial contributions represented by gray lines, which are the spectra corresponding to  $n = 20$  single ionization events occurring at  $n = 20$  different ionization times  $t_n$ . The spectrum of one ionization event is characterized by a large spectral width and its shape is determined by the coefficients  $\hat{A}_n(\omega)$  and  $C_n \hat{B}(\omega)$ . The spectral dependence of  $\hat{A}_n(\omega)$  and  $C_n \hat{B}(\omega)$  is presented in Figure 3.10 b). The coefficient  $\hat{A}_n(\omega)$  depends non-trivially on the frequency, whereas  $C_n \hat{B}(\omega)$  is constant over large frequency intervals in the order of hundreds of THz. More important is the fact of  $\hat{A}_n(\omega)$  being negligible against  $C_n \hat{B}(\omega)$  in the for us interesting frequency range of  $\approx 2 - 100$  THz. Both,  $\hat{A}_n(\omega)$  being negligible against  $C_n \hat{B}(\omega)$  as well as  $C_n \hat{B}(\omega)$  being constant in the interesting frequency regime can be exploited for simplifying Equation (3.38) even further.

First, we analytically confirm  $\hat{B}(\omega) \approx \text{const.}$  by performing the Fourier transform of  $H(t)e^{-t/\tau_c}$  in Equation (3.40). Neglecting a slowly varying phase term  $\exp(-2i\omega/\tau_c\sigma^2)$ ,  $\hat{B}(\omega)$  can be reasonably approximated by

$$\hat{B}(\omega) \sim \frac{\omega}{\omega - i/\tau_c} e^{-\frac{\omega^2}{\sigma^2}}. \quad (3.42)$$

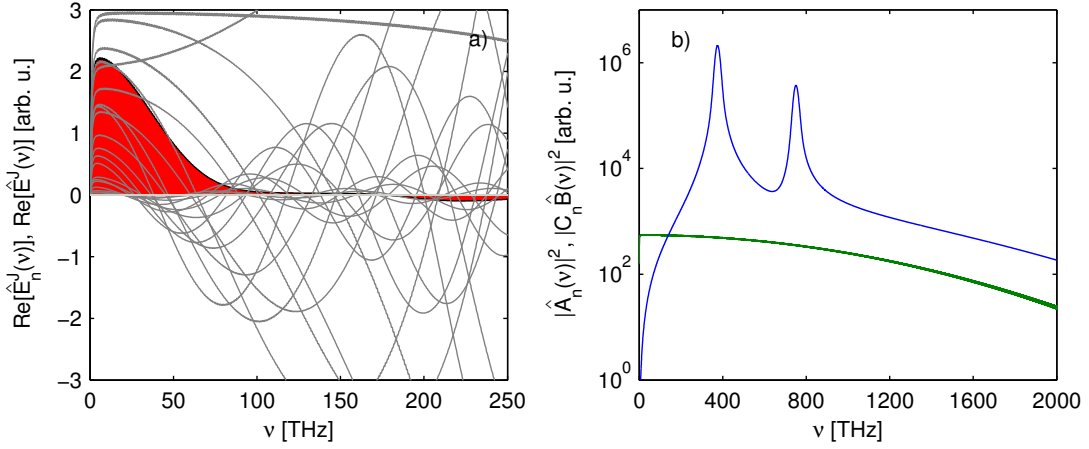


**Figure 3.10.:** a) real part of the spectra from the single  $n$ th ionization event  $\text{Re}[\hat{E}_n^j(\nu)]$  for  $-10 \leq n \leq 10$  (gray lines) and real part of the summed spectrum  $\text{Re}[\hat{E}^j(\nu)]$  (filled red curve). The spectra from different ionization events (gray lines) interfere to the total spectrum (red curve). b) Coefficients  $\hat{A}_n(\nu)$  (blue line) and  $C_n \hat{B}(\nu)$  (green line) for  $n = 0$  on a large frequency scale.

Thus,  $\hat{B}(\omega)$  features two clearly different frequency scales, determined by  $\sigma$  and  $\tau_c$ . For low frequencies  $\omega \lesssim 1/\tau_c$  we have  $\hat{B}(\omega) \propto \omega$ , whereas for frequencies of  $\approx 2 - 100$  THz  $\hat{B}(\omega) \approx \text{const.}$

In addition, we neglect  $\hat{A}_n(\omega)$ . Then, Equation (3.38) can be substantially simplified to

$$\hat{E}^J(\omega) = \hat{B}(\omega) \sum_n C_n e^{i\omega t_n} \sim \sum_n C_n e^{i\omega t_n}. \quad (3.43)$$

That is, the spectral shape of the radiated field is mainly determined by spectral interference caused by the phases  $e^{i\omega t_n}$ , since the  $C_n$  are not frequency dependent. In time domain this corresponds to attosecond-short emissions of radiation at times  $t_n$  with amplitude  $C_n$  and shape  $\partial_t[H(t - t_n)e^{1/\tau_c(t_n - t)}v(t_n)]$  (compare second terms in Equation (3.36) and Equation (3.38)).

At this point, let us summarize our findings. We have shown, that the total THz spectrum is a simple linear superposition of independent single spectra. These single spectra correspond to radiation, which is coming from the electrons generated at the well defined maxima of the two-color input field at instants of time  $t_n$ . The values of  $t_n$  define phase factors of the single spectra. Since the phase factors determine the total spectral shape, the temporal distribution of the ionization events at  $t_n$  is characterizing the total THz spectrum.

Lets now interpret the observations from the last chapter within this framework. In Figure 3.5 in the last chapter, we observed a sensitive dependence of the overall THz yield on the relative phase  $\phi$  of the fundamental and second harmonic. This can readily be explained by having a look at the factors  $C_n$  occurring in Equation (3.43). They

are displayed for the two extremal cases of  $\phi = 0$  and  $\phi = \pi/2$  in Figure 3.11 a) and b), respectively. For  $\phi = 0$  these coefficients are about one order of magnitude smaller than in the case for  $\phi = \pi/2$ . Additionally, for  $\phi = 0$  the  $C_n$  are not sign definite, thus even canceling each other for small frequencies  $\omega \approx 0$  in Equation (3.43). Thus, the radiated field is much stronger for  $\phi = \pi/2$ , where all  $C_n$  have the same sign.

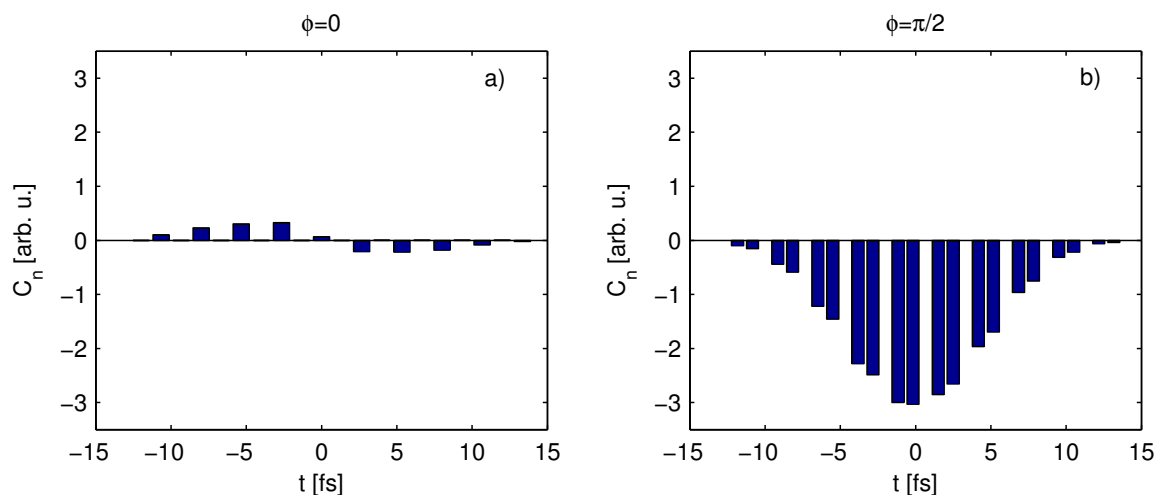


**Figure 3.11.:** The coefficients  $C_n$  at their respective ionization events at  $t_n$  for a relative phase of the input field a)  $\phi = 0$  are not sign definite and about one order of magnitude smaller than in b) for a relative phase of  $\phi = \pi/2$ .

A second important observation was the decrease of the spectral width for increasing pulse duration. Again, Equation (3.43) explains this effect. For longer pulse durations, more field maxima occur at different  $t_n$ . Therefore, for a fixed frequency, more ionization events contribute, leading to a larger number of interfering spectra, which cause a more efficient destructive overlapping. This situation is analogue to far-field interference patterns of diffractive gratings. Here, the ionization events play the role of the slits and the THz spectrum corresponds to the zeroth diffraction order. For THz spectra the interference takes place in frequency domain rather than in position space. There, the width of the spectral line is inversely proportional to the number of slits, which translates into the THz spectral width being inversely proportional to the number of ionization events, that is pulse duration.

Finally, the shift of the maximum spectral value for small frequency shifts in the second harmonic is made plausible (compare Figure 3.8 in Section 3.3.1). It turns out, that for small second harmonic shifts  $\delta\nu$  the factors  $C_n$  are not sign definite. This leads to destructive interference for frequencies  $\omega \cong 0$ . This destructive interference is partially compensated for slightly higher frequencies ( $\omega \approx 2\pi \times 30$  THz in our example in Figure 3.8) for negative detuning  $\delta\nu$ , thus the spectral maximum is shifted to higher frequencies. The lack of that partial compensation for negative  $\delta\nu$  is due to the finite duration of the input pulse [78].



## 3.4. Extended plasma source

The preceding section explained the mechanism of generation of radiation in the THz regime and introduced the fundamental properties. In particular, the strong dependence on the pump pulse parameters was demonstrated. However our analysis was restrained to a single point in space. In realistic setups, we deal with propagating pulses which lead to spatially extended sources. Thus, our aim is the description of THz radiation from extended sources. In Section 3.4.1 we introduce the tool which allows us to extract THz spectra from arbitrarily shaped sources and apply it to a simplified though generic setup in Section 3.4.2. Since the geometry of the source is closely related to the changing parameters of the propagating input pulse, we already include linear propagation of the input pulse in Section 3.4.3, but neglect any feedback originating from generated charge and THz radiation.

### 3.4.1. Jefimenko's equation

The Jefimenko approach makes use of the fact, that the electric and magnetic fields can be derived directly from Maxwell's equations for any given charge  $\rho_f(\mathbf{r}, t)$  and current  $\mathbf{J}(\mathbf{r}, t)$  distribution, provided that the electro-magnetic field does not change  $\rho_f(\mathbf{r}, t)$  and  $\mathbf{J}(\mathbf{r}, t)$  in turn. This relation was introduced by Jefimenko [77] and reads

$$\mathbf{E}^{\text{rad}}(\mathbf{r}, t) = \frac{1}{4\pi\epsilon_0} \int \left( \frac{\rho_f(\mathbf{r}', t_R)}{|\mathbf{R}|^3} \mathbf{R} + \frac{\partial_t \rho_f(\mathbf{r}', t_R)}{|\mathbf{R}|^2 c} \mathbf{R} - \frac{\partial_t \mathbf{J}(\mathbf{r}', t_R)}{|\mathbf{R}| c^2} \right) d^3 r', \quad (3.44)$$

$$\mathbf{B}^{\text{rad}}(\mathbf{r}, t) = \frac{\mu_0}{4\pi} \int \left( \frac{\mathbf{J}(\mathbf{r}', t_R)}{|\mathbf{R}|^3} \times \mathbf{R} + \frac{\partial_t \mathbf{J}(\mathbf{r}', t_R)}{|\mathbf{R}|^2 c} \times \mathbf{R} \right) d^3 r', \quad (3.45)$$

with the retarded time  $t_R = t - \frac{|\mathbf{R}|}{c}$  and  $\mathbf{R} = \mathbf{r} - \mathbf{r}'$ . We model non-relativistic electrons, rendering the influence of the magnetic field negligible. Furthermore, we consider the ionized electrons on a background of the positively charged ions giving a macroscopic neutral medium, i.e.  $\rho_f(\mathbf{r}, t) \equiv 0$ . Finally, accounting for linearly polarized light along the  $x$ -axis in the paraxial approximation leads to the scalar version of Jefimenko's equation, where we skip the vector arrows and the index  $x$  of the remaining  $x$ -component of the fields. For numerical convenience, we transfer to the reference frame moving with  $1/k_1$  ( $k_1$  inverse group velocity, see Section 2.3) along the positive  $z$ -axis giving

$$E^{\text{rad}}(\mathbf{r}, t) = -\frac{1}{4\pi\epsilon_0} \int \frac{\partial_t J(\mathbf{r}', t_R - k_1(z' - z))}{|\mathbf{R}| c^2} d^3 r', \quad (3.46)$$

where  $z, t$  are the coordinates in the co-moving frame.

In order to understand the spectra emitted by an extended source, we start with looking at the spectrum a single point source located at  $\mathbf{r}_0$  is emitting. Without loss of generality, we place our point source in the origin  $\mathbf{r}_0 = 0$ , thus our current distribution

is

$$J(\mathbf{r}', t) = \delta(\mathbf{r}')j(t). \quad (3.47)$$

Applying the Fourier transform to Jefimenko's Equation (3.46) with the above given current distribution gives

$$\hat{E}^{\text{rad}}(\mathbf{r}, \omega) = -\frac{1}{4\pi\epsilon_0} \frac{1}{r} i\omega \hat{j}(\omega) \exp\left(i\omega \frac{r}{c}\right) \quad (3.48)$$

where  $r = |\mathbf{r}|$  is the distance between the emitting point  $\mathbf{r}_0 = 0$  and the position  $\mathbf{r}$  at which the spectrum is recorded. It is obvious, that the temporal retardation  $\sim r/c$  leads to a phase factor in Fourier domain. In particular Equation (3.48) reveals, that no direction of emission is preferred and the recorded spectrum is the local one  $i\omega j(\omega)$ , only with decreased amplitude  $\sim 1/r$ .

We now proceed to compound plasma sources, consisting of many point emitters. Then, the spectrum

$$\hat{E}^{\text{rad}}(\mathbf{r}, \omega) = -\frac{1}{4\pi\epsilon_0} \int d^3r' \frac{i\omega \hat{J}(\mathbf{r}', \omega)}{|\mathbf{r} - \mathbf{r}'|} \exp\left(i\omega \frac{|\mathbf{r} - \mathbf{r}'|}{c}\right) \quad (3.49)$$

is a superposition of local point spectra located at  $\mathbf{r}'$  with different phase factors for each single emitter. In principle spectra for all current distributions  $\hat{J}(\mathbf{r}', \omega)$  can be calculated in this way. However, the integral (3.49) has to be evaluated numerically.

### 3.4.2. Simplified generic setup

Let us now start with the description of THz spectra from an extended source, generated by a propagating input pulse. The propagation of the input pulse introduces a distinguished spatial direction, namely its propagation direction. The first question that arises is whether and to which extent that distinction carries over to the emitted THz fields. Therefore, this first section focuses on the direction of THz emission. We introduce a forward (FW, in propagation direction of the input pulse) and backward (BW, against propagation direction of the input pulse) direction. We are particularly interested in the two extremal cases, i.e. the radiation is emitted exactly in FW or BW direction.

First, we develop a simple picture to explain the main difference between FW and BW emitted fields [80]. A simplified but generic setup is shown in Figure 3.12. Since in focused geometries, the generated plasma volume is usually small in transverse directions (see following Sections 3.4.3, 3.5.2, 3.5.3 and Figure 3.14), we assume a plasma line-source of length  $L$  on the  $z$ -axis, which is meant to be produced by a laser pulse propagating in positive  $z$ -direction (FW). At each point, the pump pulse ionizes the medium, the generated free electrons are accelerated in the laser field and thus build up a current  $J(t)$ , which in turn emits electromagnetic radiation. Due to the propagation of the ionizing pump pulse, points with smaller  $z$ -coordinates emit radiation

earlier than the ones with larger  $z$ -coordinates. If all propagation effects (diffraction, dispersion, etc.) are neglected, the pulse moves unchanged and all constituent points along the plasma line emit the same field, but shifted in time. This is illustrated in Figure 3.12(a), where a snapshot of the emitting plasma line is shown. Each blue circle is centered around a different point-source, representing a plane of constant phase of an elementary spherical wave for one wavelength  $\lambda$ . To record the resulting spectra on a screen located before (BW) or behind (FW) the line, Jefimenko's Equation (3.46) is used.

In our simplified setup, we assume an emitting line source of length  $L$  centered around 0 on the  $z$  axis with all points on the line emitting the same spectrum. Thus the current distribution is given by

$$J(\mathbf{r}', t) = \delta(x')\delta(y') [\Theta(z + L/2) - \Theta(z - L/2)] j(t), \quad (3.50)$$

where  $\Theta$  stands for the step function. We restrict ourselves to the calculation of on-axis spectra, since on-axis spectra correspond to fields emitted exactly in FW or BW direction. Then the spectra can be obtained analytically and differences in FW and BW spectra become apparent. As outlined before, we assume a moving pump pulse leading to temporally shifted emissions from different points along the line. These lead to additional phase factors in Fourier domain. If we define these temporal shifts to be zero for a point located at  $z = 0$  the spectrum reads

$$\hat{E}^{\text{rad}}(z, \omega) = -\frac{1}{4\pi\epsilon_0} \int_{-L/2}^{L/2} dz' \frac{i\omega \hat{j}(\omega)}{|z - z'|} \exp\left(i\omega \frac{|z - z'|}{c}\right) \exp\left(i\omega \frac{z'}{c}\right). \quad (3.51)$$

In forward direction we have  $(z - z') > 0$ , therefore

$$\hat{E}(z, \omega) = -\frac{1}{4\pi\epsilon_0} \int_{-L/2}^{L/2} dz' \frac{i\omega \hat{j}(\omega)}{z - z'} \exp\left(i\omega \frac{z - z'}{c}\right) \exp\left(i\omega \frac{z'}{c}\right) \quad (3.52)$$

$$= -\frac{1}{4\pi\epsilon_0} \ln \left| \frac{z + L/2}{z - L/2} \right| i\omega \hat{j}(\omega) \exp\left(i\omega \frac{z}{c}\right) \quad (3.53)$$

That is, the temporal delays due to different distances of emitters along the line to the screen are canceled by the retardation due to the moving pump pulse and therefore all contributions add up constructively for all wavelength  $\lambda = 2\pi c/\omega$ . Thus we end up with an amplitude-scaled local point spectrum (compare Equation (3.48)) shown in Figure 3.12 (c).

In backward direction, we have  $(z - z') < 0$ , thus

$$E(z, \omega) = -\frac{1}{4\pi\epsilon_0} \int_{-L/2}^{L/2} dz' \frac{i\omega \hat{j}(\omega)}{-(z - z')} \exp\left(-i\omega \frac{z - z'}{c}\right) \exp\left(i\omega \frac{z'}{c}\right) \quad (3.54)$$

$$= -\frac{1}{4\pi\epsilon_0} i\omega \hat{j}(\omega) f(\omega) \exp\left(i\omega \frac{z}{c}\right) \quad (3.55)$$

where we introduced the wavelength  $\lambda = 2\pi c/\omega$  dependent form factor

$$f(\lambda^{-1})^* = \text{Ei} \left[ \frac{i4\pi}{\lambda}(z - L/2) \right] - \text{Ei} \left[ \frac{i4\pi}{\lambda}(z + L/2) \right] \quad (3.56)$$

involving the exponential integral  $\text{Ei}(x) = \int_{-\infty}^x \frac{e^t}{t} dt$ . Thus the backward spectrum of the line source significantly differs from the single point spectrum, as radiation from different emitters is superimposed with different temporal delays. That is the backward spectrum is connected to the single point spectrum through  $f(\lambda^{-1})\hat{E}(\lambda^{-1})$ . Then it is evident (see Figure 3.12(b)) that the BW spectrum gets depleted for wavelengths  $\lambda \ll L$ , whereas it coincides with the FW spectrum for  $\lambda \gg L$ , because for these wavelengths the plasma line appears as a point source.

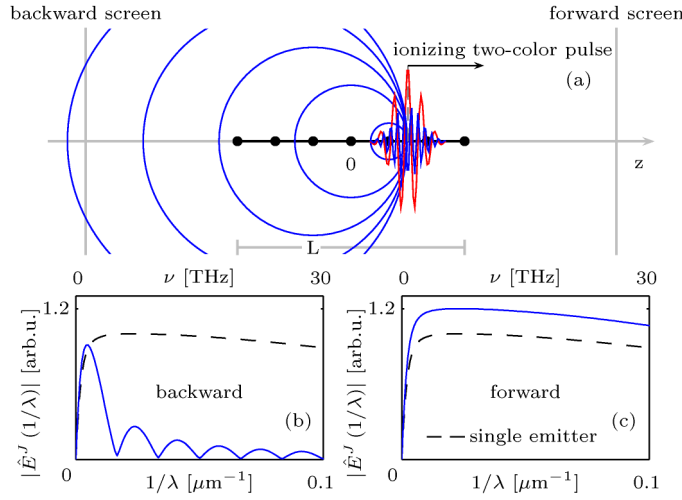


**Figure 3.12.:** (a) Schematic illustration of the interference being responsible for shaping FW and BW emission. A plasma line-source of length  $L$  created by a propagating two-color pump pulse emits radiation. Blue circles centered around exemplary point-sources represent planes of constant phase of elementary spherical waves. In FW direction (c), spherical waves interfere constructively for all wavelengths and the resulting on-axis spectrum is proportional to the single emitter spectrum. In BW direction (b), the spectral form-factor Equation (3.56) depletes wavelengths smaller than the source length (here  $L = 30 \mu\text{m}$ ).

### 3.4.3. Three dimensional Jefimenko approach

Let us now go one step further than the approximation of all emitting points of a compound plasma source radiating the same spectrum. That is, we now include linear propagation effects for the input field, but still neglect any feedback of generated plasma and THz radiation on the linear propagating pump. First, we characterize the linear propagation and then present numerical results.

We assume a two-color input pulse

$$E(z=0, r_{\perp}, t) = A\sqrt{1-\xi}\mathcal{E}_1(0, r_{\perp}, t)\cos(\omega_0 t + \phi_1) + A\sqrt{\xi}\mathcal{E}_2(0, r_{\perp}, t)\cos(2\omega_0 t + \phi_2), \quad (3.57)$$

with the according envelopes

$$\mathcal{E}_1(0, r_{\perp}, t) = \exp\left(-\frac{t^2}{\sigma_{t,1}^2}\right)\exp\left(-\frac{r_{\perp}^2}{w_1^2}\right)\exp\left(-i\frac{k(\omega_0)r_{\perp}^2}{2f}\right) \quad (3.58)$$

$$\mathcal{E}_2(0, r_{\perp}, t) = \exp\left(-\frac{t^2}{\sigma_{t,2}^2}\right)\exp\left(-\frac{r_{\perp}^2}{w_2^2}\right)\exp\left(-i\frac{k(2\omega_0)r_{\perp}^2}{2f}\right) \quad (3.59)$$

being focused (focal length  $f$ ) into the medium. Here,  $\mathbf{r}_{\perp} = (x, y)$ . Again, we assume the input pulse duration  $\sigma_{t,2}$  of the second harmonic to be smaller by a factor of  $\sqrt{2}$  compared to the fundamental  $\sigma_{t,1}$ . The same assumption is made for the input width  $w_2 = w_1/\sqrt{2}$ . The envelopes are propagated according to the linear Maxwell's equations. We assume our pulse to propagate in  $z$ -direction and moderate focusing lengths in the sense, that the paraxiality assumption  $k(\omega)^2 \gg k_{\perp}^2 = k_x^2 + k_y^2$  always holds. Then the envelopes of our pump pulse at any spatio-temporal position  $(\mathbf{r}, t)$  are given by ( $j = 1/2$  for fundamental/second harmonic) [81]

$$\mathcal{E}_j(z, r_{\perp}, t) = 8\pi^3 \sqrt{\frac{\sigma_{t,j}(0)w_j(0)}{\sigma_{t,j}(z)w_j(z)}} \exp(i\phi_j(z)) \quad (3.60)$$

$$\times \exp\left(-\frac{r_{\perp}^2}{w_j(z)^2} - i\frac{k(j\cdot\omega_0)r_{\perp}^2}{2R_j(z)}\right) \quad (3.61)$$

$$\times \exp\left(-\frac{t^2}{\sigma_{t,j}(z)^2} - iC_j(z)\frac{t^2}{\sigma_{t,j}(0)^2}\right) \quad (3.62)$$

with beam width  $w_j(z)$  and curvature  $R_j(z)$

$$w_j(z) = w(0)\sqrt{\left(\frac{z-f}{f}\right)^2 + \left(\frac{2z}{L_{b,j}}\right)^2}, \quad R_j(z) = z\frac{\left(\frac{L_{b,j}}{2f}\right)^2\left(\frac{f-z}{z}\right)^2 + 1}{\left(\frac{L_{b,j}}{2f}\right)^2\left(\frac{f-z}{z}\right) - 1}, \quad (3.63)$$

pulse duration  $\sigma_{t,j}(z)$  and chirp  $C_j(z)$

$$\sigma_{t,j}(z) = \sigma_{t,j}(0)\sqrt{1 + \left(\frac{2z}{L_{d,j}}\right)^2}, \quad C_j(z) = \frac{2z}{L_{d,j}} \left[1 + \left(\frac{2z}{L_{d,j}}\right)^2\right]^{-1}, \quad (3.64)$$

dispersion length  $L_{d,j}$  and diffraction length  $L_{b,j}$

$$L_{d,j} = \frac{\sigma_{t,j}(0)^2}{k_{2,j}}, \quad L_{b,j} = k(j \cdot \omega_0)w_j^2(0), \quad (3.65)$$

and the phase  $\phi_j(z) = \phi_{a,j}(z) + \phi_{b,j}(z) + \phi_{c,j}(z)$  given by

$$\tan[\phi_{a,j}(z)] = -\frac{L_{b,j}}{2f}, \quad \tan[\phi_{b,j}(z)] = \frac{L_{b,j}(f-z)}{2f^2} - \frac{2z}{L_{b,j}}, \quad (3.66)$$

$$\phi_{c,j}(z) = \frac{1}{2} \arctan \left[ \frac{2z}{L_{d,j}} \right]. \quad (3.67)$$

The real-valued electric field for the propagated two-color pulse in the co-moving reference frame is then obtained by

$$E(z, r_{\perp}, t) = A\sqrt{1-\xi} \operatorname{Re} [\mathcal{E}_1(z, r_{\perp}, t) \exp(i(k(\omega_0)z - \omega_0(t + k_1(\omega_0)z)))] \\ + A\sqrt{\xi} \operatorname{Re} [\mathcal{E}_2(z, r_{\perp}, t) \exp(i(k(2\omega_0)z - \omega_0(t + k_1(2\omega_0)z)))] . \quad (3.68)$$

Once the two-color field is given for any spatio-temporal point, we can apply Equation (3.10) and Equation (3.23) for calculation of the charge and current distribution. Then we use Jefimenko's Equation (3.46) and calculate the radiated field. At this point, we emphasize our main approximation again: the radiated field is completely separated from the pump field, since no feedback of the radiated field on the linear propagation of our input field is allowed.

The linear propagation is characterized in Figure 3.13 for a typical input pulse with amplitude  $A = 4.5$  GV/m, phases  $\phi_1 = 0$ ,  $\phi_2 = \pi/2$ , relative strength  $\xi = 0.2$ , width  $w = 25$   $\mu\text{m}$  and pulse duration  $\sigma_t = 34$  fs being focused with a focal length of  $f = 125$   $\mu\text{m}$  into argon gas.

The beam widths for the fundamental and second harmonic are plotted in Figure 3.13 a) versus propagation distance  $z$ . The widths reach their minimum of  $\approx 2$   $\mu\text{m}$  at the focal point at  $z = 125$   $\mu\text{m}$ . Accordingly, due to the spatial focusing the maximum amplitude of the electric field is found at  $z = f$  (Figure 3.13 c)).

Figure 3.13 b) illustrates the constant pulse durations for fundamental and second harmonic over the whole propagation distance. Dispersive broadening does not occur on that length scale due to the very large dispersion length of  $L_d = 55$  m.

Finally, in Figure 3.13 d) the behavior of the phases  $\phi_1$  of the fundamental and  $\phi_2$  of the second harmonic is presented. When passing the focal point at  $z = 125$   $\mu\text{m}$ , both phases experience the so-called Guoy phase jump of  $-\pi$ . Importantly, when considering the relative phase  $\phi = \phi_2 - 2\phi_1$  (shown as red line), a phase jump of  $\pi$  is found.

These observations lead to the following conclusions. As we learned before, for significant THz emission a high electric field amplitude is necessary, due to the fact of the charge generation depending highly nonlinear on the field amplitude. That

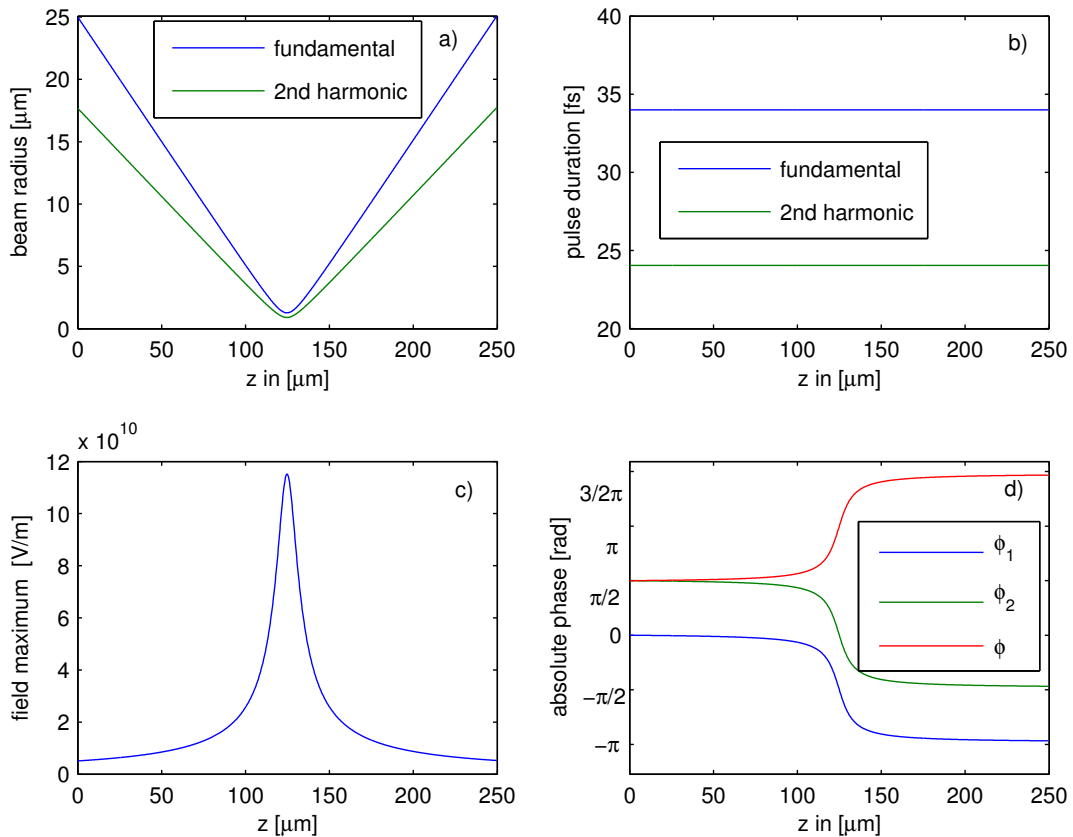


**Figure 3.13.:** Characterization of pulse parameters for a linearly propagated input pulse with amplitude  $A = 4 \times 10^9 \text{ V/m}$ , phases  $\phi_1 = 0$  and  $\phi_2 = \pi/2$ , initial width  $w = 25 \times 10^{-6} \text{ m}$  and  $w = 25/\sqrt{2} \times 10^{-6} \text{ m}$  and duration  $\sigma_t = 34 \text{ fs}$  for a focal length of  $f = 125 \mu\text{m}$ . The widths in a) are minimal in the focus at  $z = 125 \mu\text{m}$ , causing maximal field amplitudes in the focal region in c). Pulse durations in b) stay constant over the whole propagation distance. The phases  $\phi_1$  (blue line) and  $\phi_2$  (green line) in d) undergo the Guoy phase jump, which also occurs for the relative phase  $\phi = \phi_2 - 2\phi_1$  (red line).

is, we expect the main part of the THz radiation to be emitted closely around the focal point. There however, the relative phase  $\phi$  of fundamental and second harmonic quickly changes. We know from Section 3.3, that the radiated spectra crucially depend on the relative phase. Therefore, different points close to the focus emit different spectra, which then interfere to the total spectrum. This raises the question, whether our simple picture for the FW and BW spectra from above still holds, since there we assumed all contributing points to radiate the same spectrum. We answer that question in the following.

First, we confirm the assumption of the previous Section 3.4.2 of the emitting volume being a line source to be reasonable. Since the plasma is emitting the THz radiation,

we calculate the charge distribution of our focused input beam and investigate its shape. Figure 3.14 shows the iso-electron-density surface for a density of 10% of the maximum electron density  $\rho_{at}$  (single ionization), thus displaying the plasma volume, which is mainly emitting THz radiation. Having a length of about  $30 \mu\text{m}$  and a width

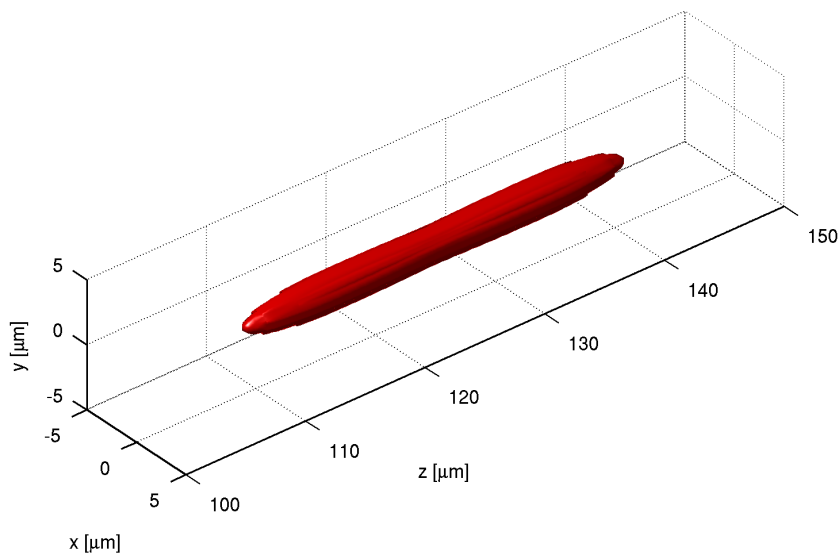


**Figure 3.14.:** Iso-electron-density surface for a density of  $0.1\rho_{at}$ . The plasma channel is obtained with the 3D Jefimenko approach for an input pulse with amplitude  $A = 4 \text{ GV/m}$ , phases  $\phi_1 = 0$  and  $\phi_2 = \pi/2$ , initial waist  $w = 25 \times 10^{-6} \text{ m}$  and initial duration  $\sigma_t = 34 \text{ fs}$  being focused with  $f = 125 \times 10^{-6} \text{ m}$  into argon gas. The plasma channel's transverse extension of  $\approx 2 \mu\text{m}$  is small compared to its length of  $\approx 30 \mu\text{m}$ .

of  $2 \mu\text{m}$  clearly justifies the radiating plasma source to be a line.

Lets now confront the prediction from the previous chapter with numerical results for our exemplary input beam. We place screens  $75 \mu\text{m}$  before and behind the focus and record the spectrum in a plane transverse to the propagation direction by using Jefimenko's equation. The result can be found in Figure 3.15. In excellent agreement with our predictions, the backward spectrum in Figure 3.15 a) is very narrow compared to the forward one in Figure 3.15 b). Moreover, estimating the length  $L \simeq 30 \mu\text{m}$  of the plasma channel (Figure 3.14) and evaluating Equation (3.56) leads to a backward spectral  $1/e$  width of  $\Delta\nu = 5 \text{ THz}$ , which coincides with the numerical obtained one in Figure 3.15 a). This agreement between analytical prediction and numerical evaluation of Equation (3.49) also holds for various plasma channel lengths, as can be seen in Figure 3.17 c). So also for a linearly propagating input pulse, interference is the governing effect shaping the backward spectrum. Due to the narrow spectral



extent of the backward spectrum, the ratio of on-axis backward and forward emitted field amplitudes is only about 0.1 for the input pulse parameters from above. We deduce, that THz radiation is mainly emitted in forward direction.

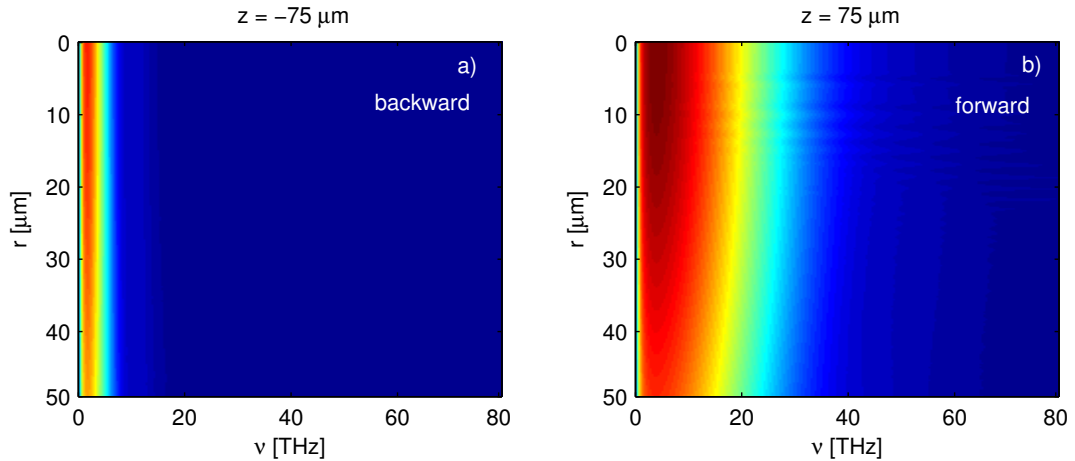


**Figure 3.15.:** 3D Jefimenko approach: The spectrum in a) backward direction is narrow due to destructive interference, in contrast to b), where the forward emitted spectrum is governed by constructive interference. We used an input pulse with amplitude  $A = 4.5 \times 10^9$  V/m, relative phase  $\phi = \pi/2$ , initial waists  $w = 25 \times 10^{-6}$  m and  $w = 25/\sqrt{2} \times 10^{-6}$  m, duration  $\sigma_t = 34$  fs and focal length  $f = 125 \times 10^{-6}$  m.

### 3.5. Propagated terahertz spectra

So far, we are able to model the spectrum of extended plasma sources. Moreover, we already described linear propagation of the pump pulse under the assumption that generated plasma and THz radiation is not affecting the pump pulse in turn. We now advance further by including feedback on the pump pulse. Furthermore, we do not only include the analytically easily describable linear propagation effects of dispersion and diffraction, which temporally and spatially broaden the pulse, but also account for Kerr and plasma nonlinearities. The nonlinear propagation of the pump and generated THz fields is no longer tractable in an analytical way. Thus, our aim is a numerical description of THz radiation generated by propagating input pulses. Further on, we want to characterize the influence of propagation effects on the THz spectrum.

The mathematical propagation models are introduced in Section 3.5.1. They are applied in Section 3.5.2 and 3.5.3, where we evolve our understanding of THz spectra from propagating input pulses. Finally we successfully compare numerical results to a real experiment.

### 3.5.1. Modeling the fields

We present two models for describing the emission of THz radiation from propagating two-color input pulses. In contrast to the linear propagation of the input pulse in the previous Section, we additionally include nonlinear propagation effects. Furthermore, we do not exclusively propagate the pump, but also include nonlinear evolution of the generated electric fields. In particular, the generated fields feed back on the pump, which was neglected before.

#### 3.5.1.1. Unidirectional pulse propagation equation

The unidirectional pulse propagation equation (UPPE) Equation (2.31) derived in Section 2.2 models forward propagating fields beyond the paraxial and slowly varying envelope approximation [64], when ignoring any z-components of the fields. It is valid for all frequencies, including the optical and THz frequencies that are important in the following. The UPPE for the Fourier transform of the electric field  $\hat{E}(k_x, k_y, z, \omega)$  reads

$$\partial_z \hat{E} = i\sqrt{k^2(\omega) - k_x^2 - k_y^2} \hat{E} - \frac{\mu_0}{2k(\omega)} (\omega \hat{J}_f - i\omega^2 \hat{P}_{\text{NL}}). \quad (3.69)$$

The first term describes linear diffraction and dispersion, included via  $k(\omega) = \omega n(\omega)/c$  with the refractive index  $n(\omega)$  for the here considered argon gas from [82]. In the second term, we replaced  $\sqrt{k(\omega)^2 - k_\perp^2} \rightarrow k(\omega)$  (compare to Equation (2.31)) by dropping the dependence of the prefactor on transverse wave numbers  $k_x, k_y$ . We checked them to be of minor influence for the upcoming simulations in Figure 3.16. The ratio  $k(\omega)/\sqrt{k(\omega)^2 - k_\perp^2}$  in a) visualizes the factor we are missing when neglecting  $k_\perp^2 = k_x^2 + k_y^2$ . These error have to be considered along with Figure 3.16 b), where the nonlinear term  $(\omega \hat{J}_f - i\omega^2 \hat{P}_{\text{NL}})$  is shown in the  $(\omega, k_\perp)$  plane. It mostly has significant contributions in the  $(\omega, k_\perp)$  region where we make negligible errors, thus our simplification is justified.

The nonlinear polarization

$$P_{\text{NL}}(x, y, z, t) = \frac{4}{3} \frac{n_0^2}{c\mu_0} \left( n_2 \frac{\rho_{\text{at}} - \rho_e}{\rho_{\text{at}}} \right) \varepsilon_0 E(x, y, z, t)^3 \quad (3.70)$$

accounts for the optical Kerr effect with the nonlinear refractive index  $n_2$  [75]. The current density consists of two contributions  $J(x, y, z, t) = J_e + J_{\text{loss}}$ . The free electron current  $J_e$  is given by Equation (3.23)

$$\dot{J}_e(x, y, z, t) + \frac{1}{\tau_c} J_e(x, y, z, t) = \frac{q_e^2}{m_e} E(x, y, z, t) \rho_e(x, y, z, t). \quad (3.71)$$

The additional current density  $J_{\text{loss}}(x, y, z, t)$  is introduced to account for losses due to ionization of the medium and therefore ensures total energy conservation. The

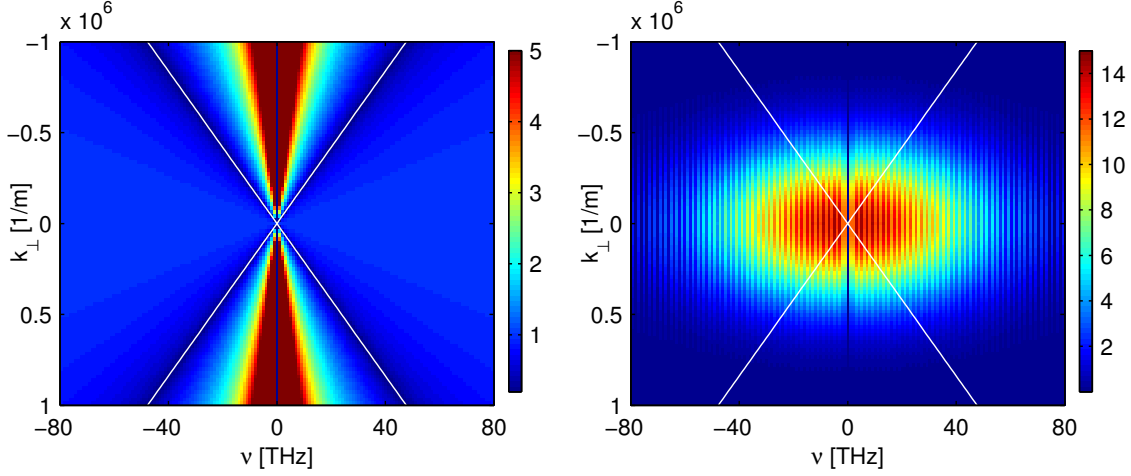


**Figure 3.16.:** a) The ratio  $k(\omega)/\sqrt{k(\omega)^2 - k_{\perp}^2}$  displays the missing factors, when replacing  $\sqrt{k(\omega)^2 - k_{\perp}^2} \rightarrow k(\omega)$ . b) The nonlinear term  $(\omega\hat{J}_f - i\omega^2\hat{P}_{NL})$  is negligible in erroneous  $(\omega, k_{\perp})$  regions. In particular, fields emitted in forward and backward direction ( $|k_{\perp}| \ll k(\omega)$ ) are correctly described. The white lines depict  $|k(\omega)| = |k_{\perp}|$ , where  $k(\omega)/\sqrt{k(\omega)^2 - k_{\perp}^2}$  is diverging. We used a typical two-color pulse with  $\omega_0 = 2\pi \times 375$  THz,  $A = 30$  GV/m,  $\xi = 0.2$ ,  $\phi = \pi/2$ ,  $w = 25$   $\mu\text{m}$ ,  $\sigma_t = 34$  fs.

energy consumed by ionization per volume and time unit is  $w_{st}(\rho_{at} - \rho_e)U_i$ , where  $U_i$  is the ionization energy of the gas under consideration. The according change of energy density per time unit is  $J_{loss}E$ , thus

$$J_{loss}(x, y, z, t) = \frac{w_{st}(E(x, y, z, t))(\rho_{at} - \rho_e(x, y, z, t))U_i}{E(x, y, z, t)}. \quad (3.72)$$

Summarizing, the UPPE models forward propagating fields for all frequencies and accounts for linear and nonlinear propagation effects. However, we deal with electric field propagation in a partially ionized gas. The present charge introduces the plasma frequency  $\nu_p$ . The plasma is opaque for fields with frequencies below the plasma frequency, i.e. fields with frequencies  $\nu < \nu_p$  are damped and can not propagate through the plasma. Since (forward) propagating fields are the crucial assumption for the derivation of the UPPE, it is not able to correctly describe these damped fields. We have to be aware of these plasma damped fields when modeling pulse propagation with the UPPE.

### 3.5.1.2. Finite-differences time-domain approach

In the Finite-differences time-domain (FDTD) approach ([83,84] and Appendix A), we directly solve Maxwell's equations. The FDTD method applies for fields emitted in

all directions and is not limited by paraxial or slowly varying envelope approximations. Due to computational limitations we resort to two spatial dimensions, where we model the evolution of transversely polarized electric (TE) fields by

$$\begin{aligned} \mu_0 \frac{\partial H_x}{\partial t} &= \frac{\partial E_y}{\partial z}, & -\mu_0 \frac{\partial H_z}{\partial t} &= \frac{\partial E_y}{\partial x}, \\ \frac{\partial D_y}{\partial t} + J_e &= \frac{\partial H_x}{\partial z} - \frac{\partial H_z}{\partial x}. \end{aligned} \quad (3.73)$$

Linear dispersive properties of argon are included via  $\hat{D}_y(\omega) = \varepsilon_0 n^2(\omega) \hat{E}_y(\omega)$ , where we use the refractive index  $n(\omega)$  given in [82]. In all FDTD calculations we neglect Kerr nonlinearities, because they play a minor role for THz generation in the upcoming simulations. In contrast to UPPE, the FDTD approach naturally includes plasma opacity and can be used for cross-checking results from UPPE.

### 3.5.2. Nonlinear propagation in the two dimensional finite-difference time-domain approach

So far, we modeled the propagation of the pump laser pulse in linear approximation. In particular, we did not consider any feedback of the generated plasma on the pump. Let us now check, whether the inclusion of nonlinear propagation effects and feedback on the pump pulse changes the characteristic differences for FW and BW fields from Section 3.4. In order to be able to describe both FW and BW fields, we model the 2D TE field evolution by means of the finite-difference time-domain method (previous Section 3.5.1.2). As outlined before, only plasma nonlinearities are included, since Kerr nonlinearities are of minor influence in the present setup. Results are to be compared to the ones obtained in Section 3.4.3, where we linearly propagated the pump pulse without any feedback. For having comparable situations, that is in order to obtain a comparable radiating plasma channel, we adjust in our input pulse Equation (3.57)

$$\begin{aligned} E(z=0, r_\perp, t) &= A \sqrt{1 - \xi} \mathcal{E}_1(0, r_\perp, t) \cos(\omega_0 t + \phi_1) \\ &\quad + A \sqrt{\xi} \mathcal{E}_2(0, r_\perp, t) \cos(2\omega_0 t + \phi_2) \end{aligned} \quad (3.74)$$

$$\mathcal{E}_1(0, r_\perp, t) = \exp\left(-\frac{t^2}{\sigma_{t,1}^2}\right) \exp\left(-\frac{r_\perp^2}{w_1^2}\right) \exp\left(-i \frac{k(\omega_0) r_\perp^2}{2f}\right) \quad (3.75)$$

$$\mathcal{E}_2(0, r_\perp, t) = \exp\left(-\frac{t^2}{\sigma_{t,2}^2}\right) \exp\left(-\frac{r_\perp^2}{w_2^2}\right) \exp\left(-i \frac{k(2\omega_0) r_\perp^2}{2f}\right) \quad (3.76)$$

the amplitude to  $A = 13.6$  GV/m, the pulse width to  $w = 32$   $\mu\text{m}$  and keep all other parameters unchanged.

A general overview is shown in Figure 3.17 d), where a snapshot of the emitted THz fields ( $\nu < 100$  THz) is shown. It illustrates the strong/weak emission in forward/backward direction, again with a THz field amplitude ratio between backward

and forward fields of about 0.1. Additionally, the generated plasma line is shown, whose length can be estimated to  $L \simeq 30 \mu\text{m}$ . The resulting spectra are recorded at screens located  $60 \mu\text{m}$  before and behind the focal point and are presented in Figure 3.17 a) and b). Once more, we observe a very narrow spectrum in backward direction compared to the broad one in forward direction. Estimating the on-axis backward spectral width gives again  $\Delta\nu \simeq 5 \text{ THz}$ , in excellent agreement with the widths estimated by linear propagation in Section 3.4.3 as well as by the simple line source setup in Section 3.4.2. Moreover, this agreement also holds for different plasma channel lengths, as shown in Figure 3.17 c).

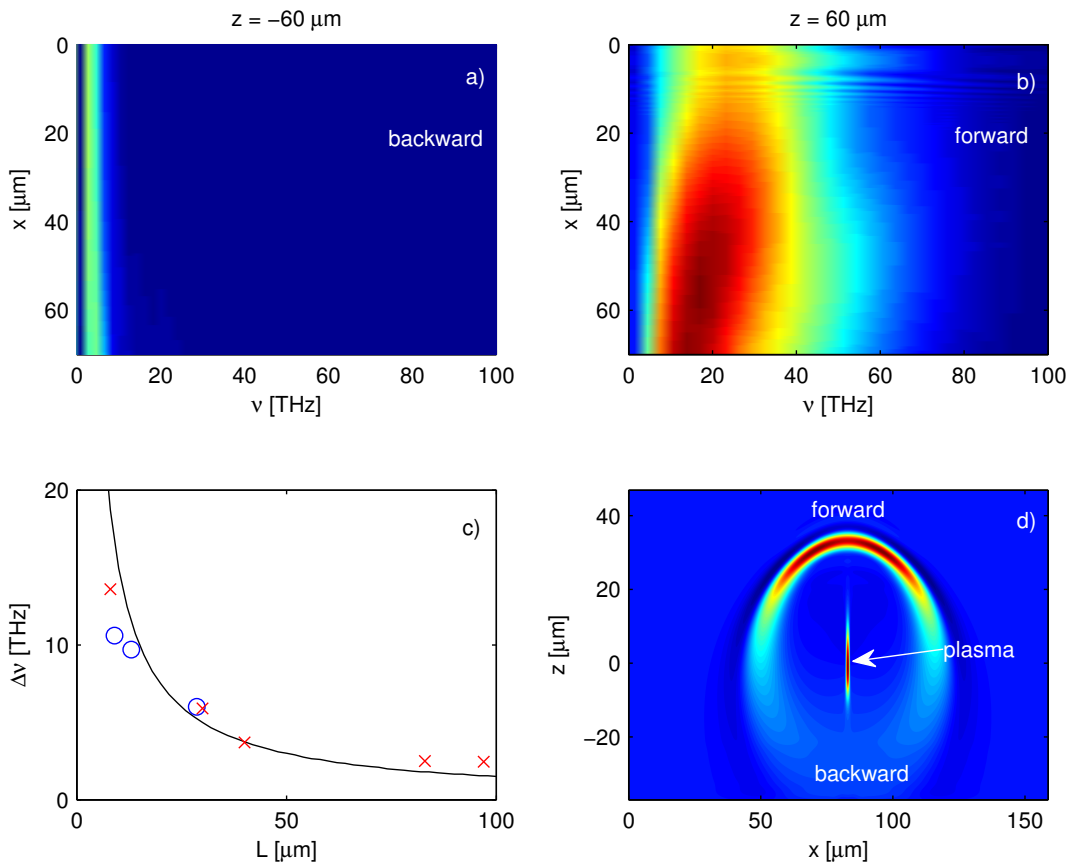


**Figure 3.17.:** 2D FDTD simulations: tera-hertz spectra  $|\hat{E}(\nu)|$  of a) BW and b) FW emitted fields. c) On-axis BW spectral width vs. plasma channel length  $L$  from Equation (3.56) (solid line), 2D FDTD calculations (blue circles), and 3D Jefimenko approach (red crosses). d) Snapshot of the emitted THz fields ( $< 100 \text{ THz}$ ) and the plasma channel, illustrating the strong (weak) emission in FW (BW) direction. The input pulse is characterized by amplitude  $A = 13.6 \text{ GV/m}$ , phases  $\phi_1 = 0$  and  $\phi_2 = \pi/2$ , initial waist  $w = 32 \times 10^{-6} \text{ m}$ , pulse duration  $\sigma_t = 34 \text{ fs}$  and focal length  $f = 125 \times 10^{-6} \text{ m}$ .

In conclusion, by solving Maxwell's equations we found that THz radiation is mainly

emitted in forward direction. The emission in backward direction is about one order of magnitude smaller in amplitude. We previously showed that this difference in forward and backward direction is due to destructive interference of radiation originating from different points in the plasma line source. Here, we confirmed that neither linear nor nonlinear propagation effects change that mechanism. Therefore, resorting to model forward propagating fields only is justified. By doing so, the numerical effort can be significantly reduced.

### 3.5.3. Results from the unidirectional pulse propagation equation

Since THz radiation is mainly emitted in forward direction, we now resort to modeling forward propagating fields only to reduce numerical costs. We use the unidirectional pulse propagation Equation (3.69) from Section 3.5.1.1. Before doing so, we will validate UPPE results against FDTD calculations, because of the following considerations. In contrast to the FDTD method applied above, UPPE does not correctly describe the opacity of the electron plasma for frequencies below the plasma frequency  $2\pi\nu_p = \sqrt{\rho_e q_e^2 / \varepsilon_0 m_e}$ . Therefore, the question arises, what impact the opacity of the plasma has when modeling the fields with the UPPE equation. While plasma opacity is of little influence for the IR pump, it is important in the THz regime.

For the (with regard to plasma opacity) correctly treated 2D setups above, we find a plasma frequency of  $\nu_p \approx 45$  THz, which reaches well into the spectral range of our THz spectra. Despite that, the THz spectra seem not to be influenced by the plasma opacity. Since the radiating plasma channel was found to be small in transverse direction (about  $2 \mu\text{m}$ ) and the emitted THz radiation is strongly diffracting (diffraction length  $L_b \simeq 3 \mu\text{m}$  at 40 THz and a width of  $2 \mu\text{m}$ ), a possible explanation is that THz radiation can just diffract around the narrow opaque region and the observed interference still governs the spectral shapes.

Nevertheless, we want to check the influence of possibly broader plasma channels. Therefore, we change our setup to the extreme case of one dimension, where diffraction in transverse directions around the opaque regions is not possible. Thus we neglect all transverse spatial dependencies. We launch two-color pump pulses into a vacuum followed by a 1 mm thick argon layer. This allows us to record backward spectra in FDTD simulations. In addition, we compare results obtained with FDTD to those from the UPPE approach, since plasma opacity is not included in the UPPE. This gives an impression of the kind of error we make when incorrectly treating opaque plasma. In UPPE we will also include third order polarization responsible for the optical Kerr effect, which was neglected in FDTD simulations.

Figure 3.18 shows pump pulses with  $\sigma_t = 34$  fs,  $\xi = 0.2$ ,  $\phi = \pi/2$  and amplitudes  $A = 34.7$  GV/m and  $A = 51.4$  GV/m launched into argon at pressure  $p = 1$  bar (atomic number density  $\rho_{at} = 2.7 \times 10^{25} \text{ m}^{-3}$ ) and  $p = 5$  bar (atomic number density  $\rho_{at} = 13.5 \times 10^{25} \text{ m}^{-3}$ ), respectively. The plasma, generated in the 1 mm long argon layer, is opaque for frequencies below  $\nu_p = 22$  THz ( $A = 34.7$  GV/m,  $\rho_e^{\text{max}} = 6 \times 10^{24} \text{ m}^{-3}$ ) and  $\nu_p = 104$  THz ( $A = 51.4$  GV/m,  $\rho_e^{\text{max}} = 13.5 \times 10^{25} \text{ m}^{-3}$ ). It

turns out that for the forward emitted THz radiation the opacity of the plasma plays almost no role, we obtain excellent agreement between FDTD and UPPE simulations [see Figure 3.18(a,b)]. The reason for this effect is detailed in Figure 3.18(c): the THz field is emitted before the plasma builds up, thus no damping influences its further forward propagation. In contrast, in BW direction plasma-opacity is important and only frequencies above the corresponding plasma frequencies can propagate through the already built up plasma. Therefore, in 1D geometry Equation (3.56) which is describing the interference is applicable only for freely propagating frequencies above  $\nu > \nu_p$ . Calculating the spectral shape according to Figure 3.12 and Equation (3.56) for a plasma length of 1 mm and considering frequencies  $\nu > \nu_p$  only, entirely destructive interference is expected. Indeed, this can be seen from the cutoffs of the backward spectra at the corresponding plasma frequencies in Figure 3.18(d). Below these frequencies  $\nu_p$ , radiation originates from the front-side of the plasma layer only, since contributions from deeper inside are damped away. Therefore, for these frequencies the effective plasma length is much shorter than 1 mm, leading to broader spectra as depicted in Figure 3.18(d).

### 3.5.3.1. Confrontation with experiment

After convincing ourselves, that the UPPE approach is well suited for describing THz emission, let us confront simulation results with a real experimental setup [26]. In the experiment, a Ti:sapphire laser system produces 40 fs pulses with a repetition rate of 1 kHz at central wavelength 800 nm and energies of  $\sim 300 \mu\text{J}$ . These pulses with 8 mm diameter are focused by an achromatic lens with a focal length of 40 mm. At 7 mm before the focus a 0.1 mm thin  $\beta$ -barium borate (BBO) crystal cut for type I second harmonic generation is inserted into the beam. This whole setup is placed in an chamber filled with argon at pressures between 1 and 1000 mbar. THz radiation emitted from the plasma volume in the focal spot is collected by a parabolic mirror of 25.4 mm diameter at a distance equal to its focal length of 12.7 mm. The intensity interferograms were recorded with a mercury cadmium telluride (HgCdTe) detector by varying the path difference between the two arms of a Michelson interferometer. THz spectra were then derived by Fourier transformation.

The experimental situation is modeled by considering two-color Gaussian input beams of the form of Equation (3.74) with waist  $w = 100 \mu\text{m}$ , duration  $\sigma_t = 14.1 \text{ fs}$  ( $\hat{=}$ 40 fs FWHM) and central wavelength  $\lambda = 800 \text{ nm}$ . The relative strength of the second harmonic at 400 nm is estimated from the experiment to  $\xi = 0.1$ , its pulse duration and waist are by a factor of  $\sqrt{2}$  smaller than the ones of the fundamental. The energy was 300  $\mu\text{J}$ . The relative phase is chosen  $\phi = 0$  initially and, of course, changes upon propagation. We numerically focus the pulse into argon with a focal length  $f = 0.5 \text{ mm}$ , in order to have comparable  $w/f$  ratios in experiment and simulation.

A numerical illustration of the situation at pressure  $p = 200 \text{ mbar}$  is given in Figure 3.19. The evolution of the plasma density is shown in a), where the input field exceeds the ionization threshold shortly after the starting point of the simulation at

### 3. Terahertz Generation by Ionizing Two-Color Laser Pulses

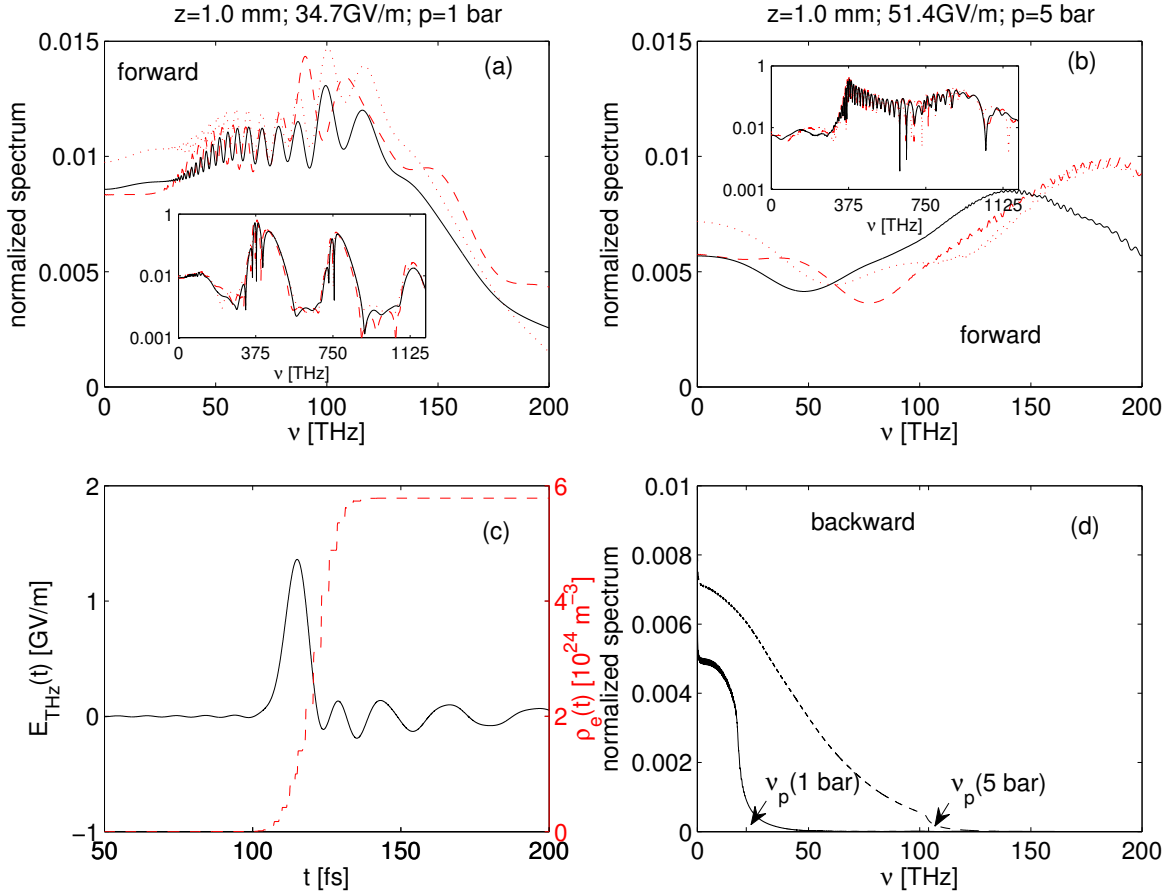


**Figure 3.18.:** 1D simulations: FW tera-hertz spectra for (a)  $A = 34.7$  GV/m at 1 bar and (b)  $A = 51.4$  GV/m at 5 bar from FDTD simulations (black solid line) and UPPE simulations with (dashed red line) and without (dotted line) third order nonlinear polarization included. The insets show the complete spectra. (c) UPPE results illustrate that tera-hertz emission (solid black line) takes place mainly at the ionization front (dashed red line). (d) shows BW tera-hertz spectra for parameters used in (a) (solid line) and (b) (dashed line), both obtained from FDTD simulations. All spectra are normalized to  $|\hat{E}_{\text{in}}(\nu = 375 \text{ THz})|$ .

$z = 0$  mm and forms a narrow, 0.7 mm long plasma channel. The present THz fields ( $\nu < 80$  THz) at the beginning ( $z = 0.2$  mm) and after the plasma channel ( $z = 1.0$  mm) are shown in Figure 3.19 b) and c), respectively. We deduce, that THz fields are generated inside the plasma channel in the focal region, where they reach amplitudes of the order of GV/m. Upon propagation they do strongly diffract.

The dependence of the THz spectra on gas pressure is shown in Figure 3.20. The measured spectra for pressures between 0 and 1000 mbar are shown in Figure 3.20 a) for frequencies the HgCdTe detector is sensitive for, that is for frequencies ranging from 20 THz to 170 THz. For the comparison of experiment with simulation, this high frequency part of the spectra is the most relevant one, since the spectral



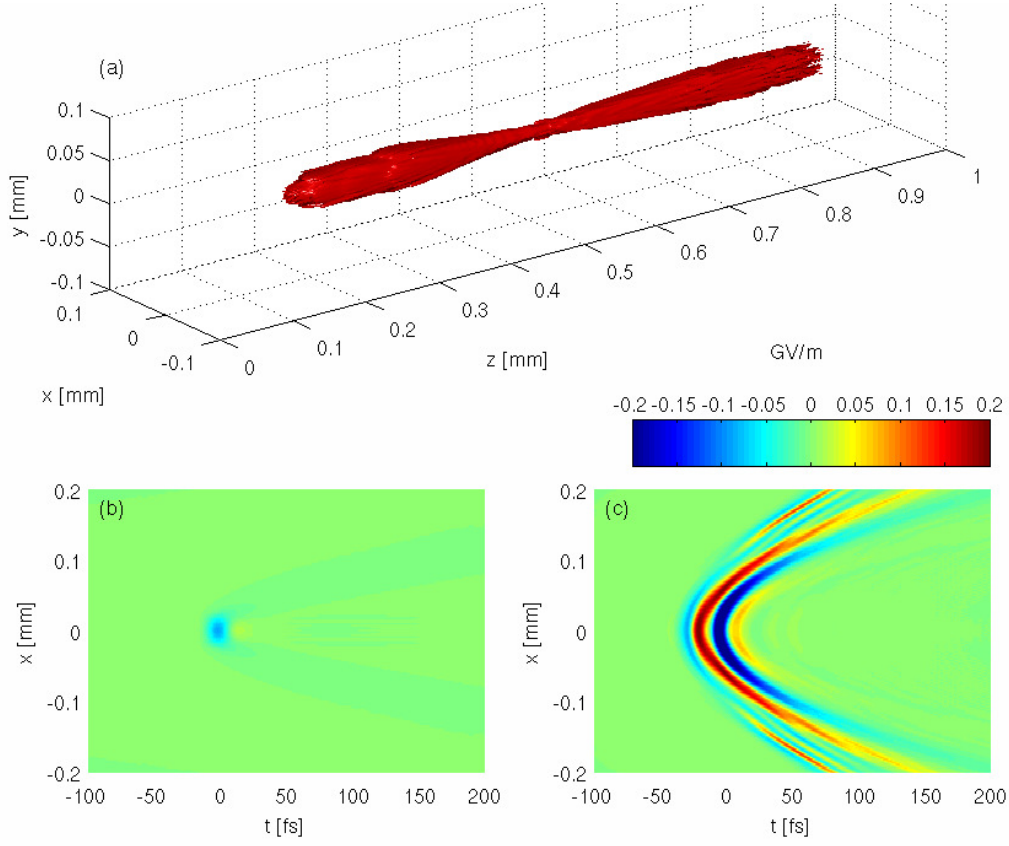


**Figure 3.19.:** a) The plasma channel. The iso-electron-density surface at  $\rho = 5 \times 10^{17} \text{ cm}^3$  is shown for 200 mbar gas pressure and confirms the line shape of the plasma channel. The computed THz fields for  $\nu < 80 \text{ THz}$  at b)  $z = 0.2 \text{ mm}$  and c)  $z = 1.0 \text{ mm}$  show the THz radiation being emitted in the plasma channel.

shape depends on the gas pressure for these frequencies. These spectra correspond to fields emitted in the focal region of length  $\lesssim 0.3 \text{ mm}$  of the parabolic mirror. The depleted spectra for small pressures indicate the plasma and not the sum frequency process being responsible for THz generation. For rising pressures up to 300 mbar, the spectra are broadening significantly. From 500 mbar onwards, the spectral width stays rather constant. The overall THz yield is depicted in Figure 3.20 e), showing a linear increase, before saturating at 400 mbar. An exemplary low frequency spectrum measured by electro-optic sampling at 1000 mbar (Figure 3.20 c)) possesses a characteristic maximum at 5 THz, matching the numerical one (Figure 3.20 d)).

These findings are compared to simulation results in Figure 3.20 b) and d). The spectra are computed by integrating over the transverse coordinates  $x, y$ . Excellent agreement with the experiment can be reported for pressures below 500 mbar and fields generated at propagation distance  $z \approx 0.2 \text{ mm}$ . THz fields generated at larger propagation distance are spectrally much broader, therefore we deduce, that the parabolic

mirror in the experiment images the leading part of the plasma channel. The overall THz yield matches the experimental one Figure (3.20 e)) for pressures up to 400 mbar. The numerical yield is calculated directly at  $z = 0.2$  mm, in contrast to the experiment, where THz losses due to further propagation towards the mirror are probably responsible for the observed saturation.

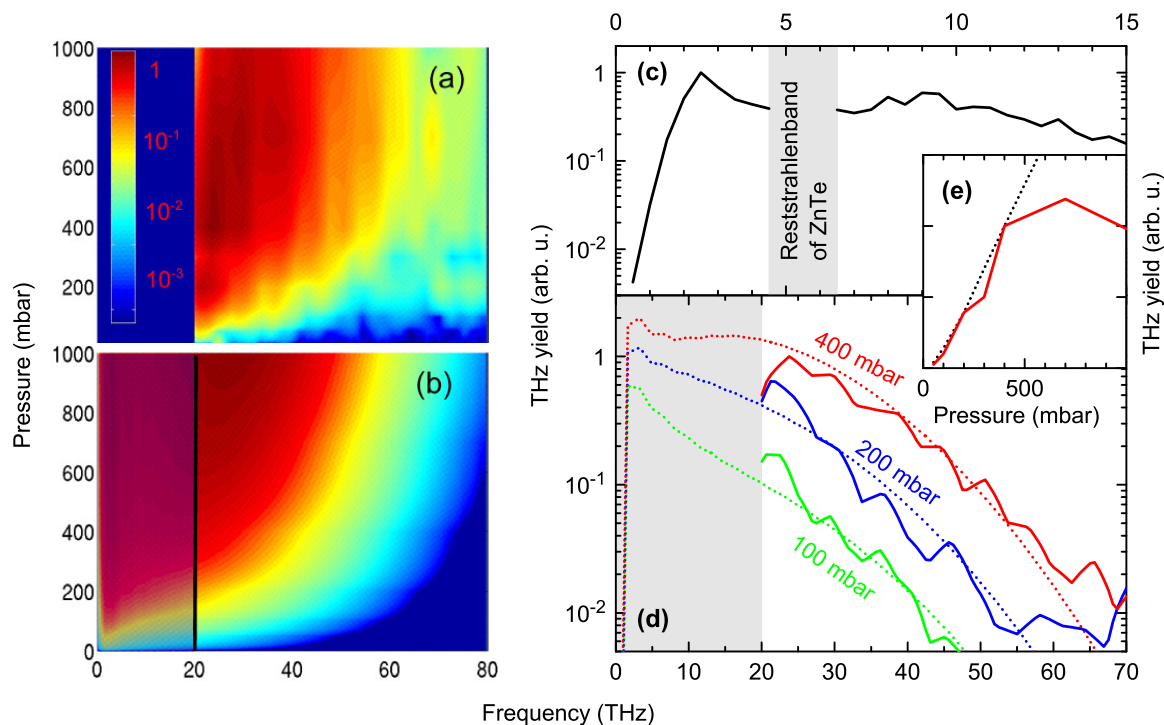


**Figure 3.20.:** THz spectra from experiment a) and from simulations b) for pressures between 1 and 1000 mbar. c) depicts an experimental low-frequency spectrum at 100 mbar measured by electro-optic sampling in ZnTe, corrected for the frequency dependent detector response [85]. d) compares experimental (solid lines) and theoretical (dashed lines) spectra for different pressures. The dependence of the overall THz yield on pressure is shown in e) for experiment (solid line) and simulation (dashed line). The shaded regions in a)-d) represent regions where no experimental data are available.

Let us finally interpret the experimental and numerical finding of the strong pressure dependence of THz spectra. It can not be explained within our local current approximation, since there, varying the pressure would lead to a mere amplitude scaling of the current. Therefore, it must emerge from pressure dependent nonlinear propagation effects. It turns out, that the spectral broadening of the fundamental and second harmonic is too small to explain the strong pressure dependence. However, due to the generated plasma, a change in the nonlinear refractive index is induced. This change causes small blue shifts in the central frequencies [86,87]. These shifts are about 1 THz in the fundamental and 0.4 THz in the second harmonic at a propagation

distance  $z = 0.2$  mm for 400 mbar and strongly depend on the generated plasma, i.e. gas pressure. As we learned in a previous section, these frequency shifts can cause the spectral maximum to shift to higher frequencies. However, the needed spectral shifts of  $\delta\nu \gtrsim 20$  THz for a significant shift of the spectral maximum in the local spectrum approximation are much larger than the shifts observed here. But the local spectrum approximation does not take any feedback of generated radiation into account, thus different values are not surprising. Furthermore, upon propagation, the relative phase between fundamental and second harmonic changes, which again can alter the spectral shape. Thus in the present setup, different spectral shapes originating from different spatial points are added and averaged, leading to the strong spectral broadening.

### 3.6. Summary and outlook

We characterized the THz radiation that is generated when focusing an ionizing two-color pulse into a gas. We demonstrated, that the physical process of frequency conversion as well as the process of a radiating plasma current are able to generate THz radiation in such a setup. We confirm that the plasma current is the governing mechanism and therefore focus on the analysis of this mechanism. In the local spectrum approximation, we were able to analytically deduce, that the radiated THz spectrum is an interference of many single spectra. These single spectra correspond to short burst of radiation. This radiation is emitted during short, well separated periods of time close to an ionization event at which the charge density increases step-wise. This understanding allowed us to explain the observed local spectra. In a next step, we considered extended sources and subsequently included propagation effects of the input pulse as well as of the radiated THz field. By advancing from merely shifting the input pulse along an assumed propagation direction in Section 3.4 via directly solving Maxwell's equations with the FDTD method in Section 3.5.2 to the evolution of the fields with the unidirectional pulse propagation equation UPPE in Section 3.5.3 we revealed the propagation direction of the input pulse to be the main direction of THz emission. Finally, we confronted experimental results with simulation results obtained from the UPPE approach and observed excellent agreement. In summary, we are able to make well-grounded, reliable predictions for THz spectra with the UPPE approach and above all are able to explain their structure within the framework of the photo-current mechanism.

A point for further improvement would be to go beyond considering linearly polarized light only. Then, vectorial effects in the propagation of the fields have to be accounted for. These can lead to emission of THz radiation not only in forward direction. Thus, on the one hand the UPPE approach renders inapplicable and a treatment with the FDTD method is mandatory. There, room for advancement lies in the implementation of demanding numerics. On the other hand, accounting for vectorial effects opens new possibilities for optimization of the THz yield, or for engineering the spectral shape. One can think of, e.g. radially polarized light. Moreover, the analytical

### *3. Terahertz Generation by Ionizing Two-Color Laser Pulses*

---

description can be refined to handle the new challenges that arise in such setups.

# 4. Self-Compression of Ultra-Short UV-Pulses in a Self-Defocusing Gas

## 4.1. Introduction

The common property of laser pulse compression schemes is the utilization of nonlinear effects the pulse undergoes upon propagation. The omnipresent idea of these schemes is to broaden the pulse spectrum and ensure a flat spectral phase at the same time. Among others, such as frequency conversion in filaments [32] or cascading quadratic nonlinearities [33–35], the spectral broadening ability of self phase modulation (SPM) is often exploited in the guided configuration (waveguides, fibers). The resulting phase can be compensated by applying some post compression mechanisms such as Bragg gratings and chirped mirrors or, even more convenient, by a counteracting term on the phase contributions, that is in our case the group velocity dispersion (GVD).

The simplest model that captures both processes is expressed by the famous nonlinear Schrödinger (NLS) equation for the slowly varying envelope of an optical pulse  $\mathcal{E}(z, t)$ :  $\partial_z \mathcal{E} = -ik_2 \mathcal{E}_{tt}/2 + i\gamma |\mathcal{E}|^2 \mathcal{E}$ . Here,  $k_2 = \partial^2 k(\omega)/\partial \omega^2|_{\omega=\omega_0}$  is the GVD coefficient at center frequency  $\omega_0$  and  $\gamma = n_2 \omega_0/c$  is the Kerr coefficient with index  $n_2 \propto \chi^{(3)}$  defined by the relevant diagonal element of the third-order susceptibility tensor  $\chi^{(3)}$ . The standard case described above would be anomalous GVD ( $k_2 < 0$ ) counteracting on positive Kerr response ( $\gamma > 0$ ), since a negative second derivative of the wave number  $k_2$  is more common than a negative  $\gamma$ . Trying to transfer this "solitary compression mechanism" to the unguided bulk setup gives rise to problems due to self-focusing and subsequent collapse of the beam in the transverse spatial directions. Resolving this problem and still sticking to the "solitary compression" (phase cancellation due to different signs of GVD  $k_2$  and SPM  $\gamma$ ) means to ensure a negative  $\gamma$ . Indeed, negative values for the Kerr response can be found, e.g., in the UV near two photon resonances in Xe [41]. However, the strong dispersion of the nonlinearity near these resonances questions the compression mechanism which is based on a constant nonlinearity. Nevertheless, it was shown recently [44] and will be elucidated in more detail in this chapter, that the basic compression mechanism survives these obstacles. Moreover, we will present an alternative scenario where pulse compression is actually caused by the nonlinear dispersion, while the Kerr index  $n_2$  approaches zero at center wavelength.

We start with the presentation of the basic "solitary compression" scheme within the NLS framework and will introduce fundamental terms in Section 4.2. Then, the governing equation for the following analysis is derived in Section 4.3, where we particularly concentrate on the dispersive property of the nonlinearity  $\sim \chi^{(3)}$ . In Section 4.4 we deal with a purely temporal setup in order to reveal the influence of nonlinear dispersion on pulse dynamics. In a last step, we analyze self-compression in the full spatio-temporal setup in Section 4.5 and finally conclude in Section 4.6.

## 4.2. Basic idea of self-compression

Here, we introduce the "solitary compression" scheme, which constitutes the fundamental idea for the following sections. The simplest model that describes compression is based on the NLS equation (2.55), whose derivation is already given in Section 2.4. A more detailed justification can be found in Section 4.4. We proceed with the explanation of the basic idea by explaining the spectral broadening capability of the SPM mechanism in Section 4.2.1. Then the inherent problem of standard setups is demonstrated in Section 4.2.2: transverse spatial collapse of the laser pulse. A possibility to resolve that obstacle is presented by example in Section 4.2.3.

### 4.2.1. Self phase modulation

In the following, we briefly review the mechanism for temporal compression in the NLS. For that purpose we neglect any transverse spatial dependencies and normalize by

$$\mathcal{E}(z, t) = \sqrt{I_0} e(z, \tau) \quad t = \tau_0 \tau. \quad (4.1)$$

Here,  $\mathcal{E}_0$  and  $\tau_0$  are the envelope amplitude and duration, respectively. Then, we deal with the dimensionless one dimensional NLS

$$\partial_z e = -i \frac{\text{sgn}(k_2)}{L_d} \partial_t^2 e + i \frac{\text{sgn}(n_2)}{L_{\text{NL}}} |e|^2 e, \quad (4.2)$$

where we introduced the dispersion length  $L_d$  and the nonlinear length  $L_{\text{NL}}$

$$L_d = \frac{2\tau_0^2}{|k_2|} \quad L_{\text{NL}} = \frac{c}{\omega_0 |n_2| I_0}. \quad (4.3)$$

$L_d$  and  $L_{\text{NL}}$  provide the length scales over which dispersive and nonlinear effects become important. We use that property to illustrate how the pulse evolution is affected by either the dispersion or the nonlinear term.

For  $L_d \gg L_{\text{NL}}$  the dispersion term is negligible and pulse evolution is dominated by the nonlinear term. Then, the NLS is solved by

$$e(z, \tau) = e(0, \tau) \exp(i\phi_{\text{NL}}(\tau)) \quad \phi_{\text{NL}}(\tau) = |e(0, \tau)|^2 \frac{z}{L_{\text{NL}}}. \quad (4.4)$$

We learn, that the temporal profile  $e(z, \tau)$  keeps its initial shape  $e(0, \tau)$  for all propagation distances and only a self similar, time dependent phase  $\phi_{\text{NL}}(\tau)$  is accumulated upon propagation. Therefore, this effect is termed self phase modulation (SPM). The SPM induced time dependent phase leads to spectral broadening in Fourier domain, as shown in Figure 4.1 b). This gets clear, when considering instantaneous frequency shifts given by

$$\delta\omega = \partial_\tau \phi_{\text{NL}}(\tau) = \frac{z}{L_{\text{NL}}} \partial_\tau |e(0, \tau)|^2. \quad (4.5)$$

With increasing propagation distance these shifts grow, that is new frequency components are continuously generated upon propagation. Such a broadened spectrum is a prerequisite for a short pulse in time domain. Unfortunately, the newly generated spectral components exhibit different spectral phases as shown in Figure 4.1 d). Only a flat spectral phase ensures that all frequency components are present at the same time and form a short pulse in time domain. In particular, the sign of the spectral phases depends on the sign of  $n_2$ , as it enters the solution via  $L_{\text{NL}}$ .

When  $L_d \ll L_{\text{NL}}$  then the pulse evolution is purely dispersive. Without the nonlinear term, the NLS is readily solved by

$$\hat{e}(z, \omega) = \hat{e}(0, \omega) \exp\left(i \frac{\text{sgn}(k_2)}{L_d} \omega^2 z\right) \quad (4.6)$$

in Fourier domain. It is obvious, that the spectral shape stays constant (see Figure 4.1 a)). Only a spectral phase is added upon propagation (see Figure 4.1 c)). Similarly as before,  $\text{sgn}(k_2)$  determines the sign of the spectral phases.

Knowing these two effects the dispersive and nonlinear term have on pulse evolution renders the mechanism for pulse compression obvious: SPM is used to broaden the spectrum. The resulting spectral phases are canceled by spectral phase contributions from the dispersive term. For that, we have to ensure different signs of  $k_2$  and  $n_2$ . In particular, when adjusting pulse parameters  $\mathcal{E}_0$  and  $\tau_0$  correctly the length scales  $L_d$  and  $L_{\text{NL}}$  are on the same order. Additionally choosing a special input shape  $e(z = 0, \tau)$  leads to a situation, where phase contributions from the nonlinear and dispersive term cancel and the input pulse propagates with constant shape. These extraordinary pulses are called solitons. However, there exists a whole class of soliton solutions, e.g. whenever the ratio between dispersion and nonlinear length matches certain integer numbers  $N$ , the pulse shape undergoes periodic modulations, including compression stages and one speaks of  $N$  soliton solutions (see Section 4.4.3). These special solutions, also based in the interplay of SPM and dispersion reason the term "solitary compression". For ensuring different signs of  $k_2$  and  $n_2$ , the standard case is anomalous GVD  $k_2 < 0$  counteracting on positive  $n_2 > 0$ , since a negative second derivative of the wave number  $k_2$  is more common than  $n_2 < 0$ . However, dealing with  $n_2 > 0$  introduces a serious problem, as demonstrated in the following.

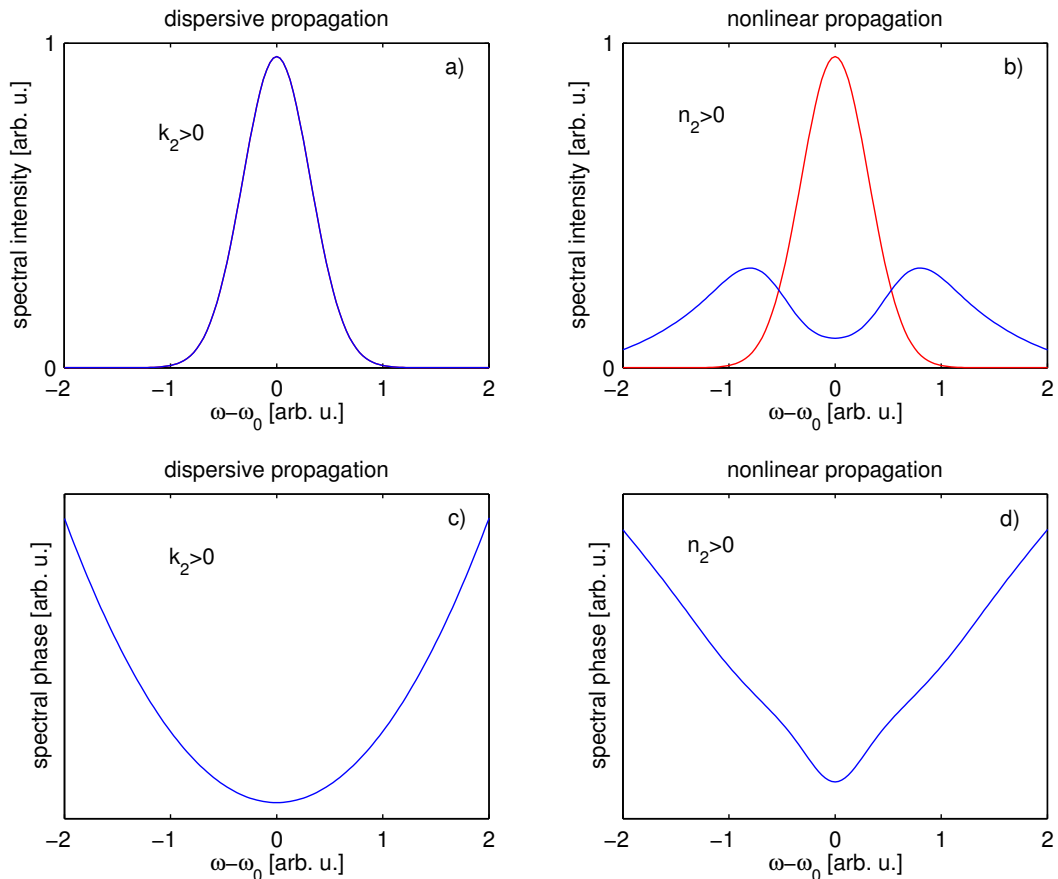


**Figure 4.1.:** Illustration of the effect of dispersion and self-phase modulation on pulse evolution. Purely dispersive propagation: a) The input spectral intensity  $|\hat{e}(z=0, \omega)|^2$  (red line) is identical to the propagated one (blue line). c) Only a quadratic spectral phase is accumulated. In contrast, the exclusively nonlinear propagation: b) The input spectrum (red line) is broadened upon propagation (blue line) with d) a varying phase in Fourier domain.

### 4.2.2. Spatial wave collapse

In the following we introduce the phenomenon of spatial self-focusing and subsequent collapse in the transverse direction. In order to illustrate the mechanism, we may disregard temporal dependencies, thus the dispersion term  $-i\frac{k_2}{2}\partial_t^2\mathcal{E}$  in the NLS Equation (2.55) is neglected and

$$\partial_z\mathcal{E} = \frac{i}{2k_0}\nabla_{\perp}\mathcal{E} + i\frac{\omega_0}{c}n_2|\mathcal{E}|^2\mathcal{E} \quad (4.7)$$

describes the pulse propagation. Comparing the nonlinear term of this three dimensional NLS with the second term on the r.h.s. of the forward Maxwell propagation



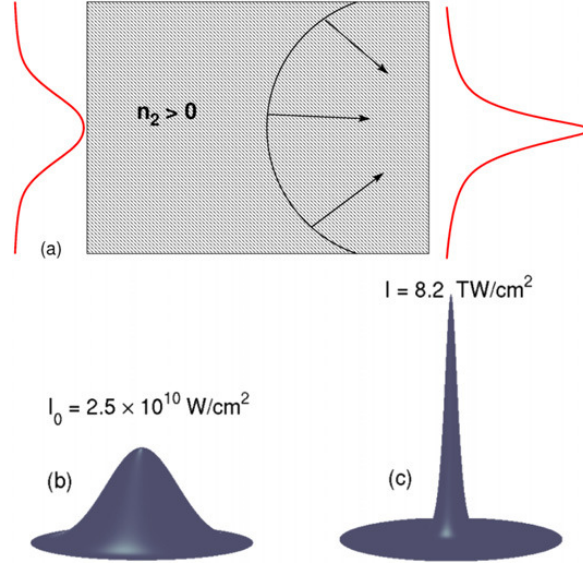


**Figure 4.2.:** a) The intensity dependent refractive index variations are illustrated for  $n_2 > 0$ . b) and c) depict the peak intensity of a Gaussian input pulse and after some propagation, respectively. The picture is taken from [39].

Equation (2.28) reveals, that the nonlinear contribution to the refractive index  $n_2|\mathcal{E}|^2$  is intensity dependent. As depicted in Figure 4.2 a), this intensity dependence leads to index variations proportional to the intensity profile  $|\mathcal{E}|^2$ . For  $n_2 > 0$  the refractive index is increased. Optical rays are diffracted towards high index regions, which leads to transverse compression. On the other hand, the term  $\frac{i}{2k_0}\nabla_{\perp}\mathcal{E}$  is responsible for linear diffraction which eventually broadens the beam in space. However, when the power of the input profile  $P_{in} = \int|\mathcal{E}|^2 d\mathbf{r}$  exceeds a critical power [39, 40]

$$P_{cr} = \frac{3.72\lambda_0^2}{8\pi n_0 n_2}, \quad (4.8)$$

the transverse compression overcomes linear diffraction and the beam self-focuses as illustrated for a Gaussian beam in Figure 4.2 b) and c). The width decreases as the amplitude  $\mathcal{E}$  diverges. Finally, the Gaussian beam reaches (formally) zero width at [40]

$$z_c = \frac{0.367z_0}{\sqrt{\left(\sqrt{\frac{P_{in}}{P_{cr}}} - 0.852\right)^2 - 0.0219 + 0.367\frac{z_0}{f}}} \quad (4.9)$$

where  $z_0 = k_0 w_0^2/2$  and  $f$  are the diffraction and focal length of a Gaussian beam, respectively.

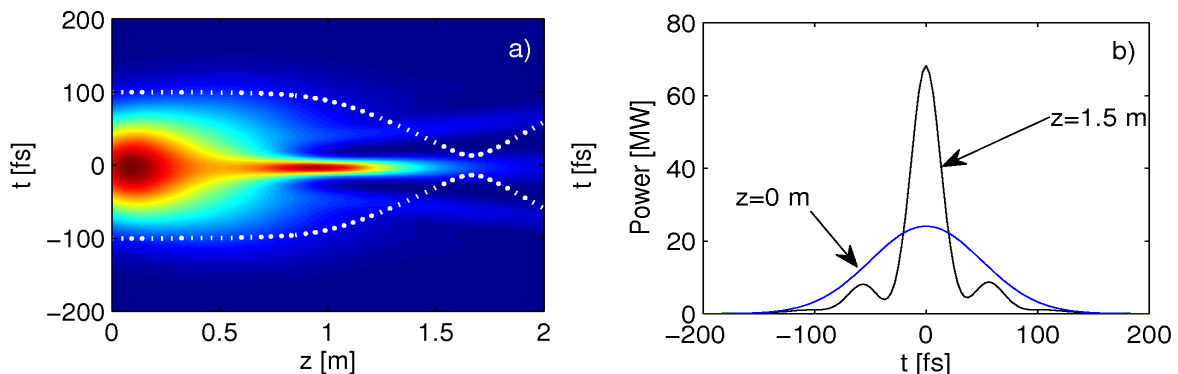


**Figure 4.3.:** Demonstration of the possibility of self-compression for  $k_2 > 0$  and  $n_2 < 0$ . A Gaussian pulse with  $\tau_0 = 100$  fs,  $P_{in} = 24$  MW and width  $w = 0.3$  mm was focused  $f = 1$  m into a medium with  $k_2 = 13.12$  fs<sup>2</sup>/cm,  $n_2 = -1.56 \times 10^{-17}$  cm<sup>2</sup>/W (xenon in NLS approximation at  $\lambda = 243$  nm). The pulse not only temporally compresses on-axis as depicted in a), but also in terms of power as proven in b).

### 4.2.3. Demonstration of bulk self-compression

As we just revealed, compressing pulses with our above compression scheme with  $k_2 < 0$  and  $n_2 > 0$  leads to inevitable spatial collapse. The setup we are looking for has to inhibit spatial collapse and therefore has to ensure  $n_2 < 0$  and  $k_2 > 0$ . This is indeed possible (see Section 4.3.2), but here we assume a given  $n_2 < 0$  and  $k_2 > 0$  and numerically demonstrate the compression scheme. Figure 4.3 demonstrates temporal compression in such a setup. In a) the on-axis intensity is plotted versus propagation distance. The initially long pulse temporally compresses down to  $\sim 15$  fs after 1m of propagation. By plotting the spatially integrated pulse profile, Figure 4.3 b) illustrates that temporal compression not only occurs on-axis, but over the full transverse spatial width.

The promising results motivate the detailed analysis which is performed in the following.

## 4.3. Specification of the governing equation

We specify the basic equation for modeling pulse self-compression as it is used for the considerations in the following Sections. In particular, we provide the material responses to meet the unusual situation of  $k_2 > 0$  and  $n_2 < 0$ .

### 4.3.1. Forward propagation equation for the complex field

We start our derivation with Equation (2.49) for the complex envelope of the forward propagating electric field in the co-moving reference frame. Furthermore, for the intensities in the upcoming analysis ionization is negligible, thus assuming  $\rho_f = 0$

and  $J_f = 0$  is justified.

With regard to the polarization Equation (2.17), we are only interested in contributions having approximately the same frequency  $\omega_0$  as our initial pulse and therefore omit terms responsible for higher order harmonics generation. This is justified, since the higher harmonic frequencies occur with a large phase mismatch, e.g.  $k(3\omega_0) \neq 3k(\omega_0)$  for the third harmonic, and therefore do not contribute to pulse propagation. After introducing the envelopes  $\hat{\mathcal{E}}$  in Equation (2.17), the resulting expression for a dispersive third order nonlinear polarization in Fourier domain is

$$\begin{aligned} \hat{P}_{\text{NL}}(\omega) &= \varepsilon_0 s^{3/2} \iint d\omega_1 d\omega_2 \chi^{(3)}(-\omega; \omega - \omega_1 - \omega_2, \omega_2, \omega_1) \\ &\quad \times 3\hat{\mathcal{E}}(\bar{\omega}_1)\hat{\mathcal{E}}(\bar{\omega}_2)\hat{\mathcal{E}}^*(\bar{\omega}_1 + \bar{\omega}_2 - \bar{\omega})e^{i(k_0+k_1\bar{\omega})z}. \end{aligned} \quad (4.10)$$

Then, the propagation equation for the slowly varying complex envelope reads

$$\begin{aligned} \partial_z \hat{\mathcal{E}} &= \frac{i}{2k(\omega)} \nabla_{\perp}^2 \hat{\mathcal{E}} + i[k(\omega) - k_0 - k_1\bar{\omega}] \hat{\mathcal{E}} + \frac{3i\omega^2 s}{2k(\omega) c^2} \iint d\omega_1 d\omega_2 \\ &\quad \times \chi^{(3)}(-\omega; \omega - \omega_1 - \omega_2, \omega_2, \omega_1) \hat{\mathcal{E}}(\bar{\omega}_1)\hat{\mathcal{E}}(\bar{\omega}_2)\hat{\mathcal{E}}^*(\bar{\omega}_1 + \bar{\omega}_2 - \bar{\omega}). \end{aligned} \quad (4.11)$$

Note, that we explicitly kept the dispersion in the nonlinearity  $\chi^{(3)}$  in order to analyze its influence on pulse compression.

### 4.3.2. Material model

In the following analysis, we take the linear dispersion for Xe from [88], given by

$$k(\omega) = \frac{\omega}{c} \left( 1 + \frac{121.461}{10^6} \left( \frac{25.6}{46.301 - \lambda^{-2}} + \frac{23.8}{59.578 - \lambda^{-2}} + \frac{523.770}{112.860 - \lambda^{-2}} \right) \right), \quad (4.12)$$

where  $\lambda = 2\pi c/\omega$  is in  $10^{-6}\text{m}$ . It results from fitting experimental data with the microscopic Lorentz-Lorenz theory for the polarizability [89, 90]. Its range of validity reaches down to wavelengths of 230 nm, which justifies the application in the following, where we deal with wavelengths  $\sim 240$  nm.

The nonlinear dispersion  $\chi^{-\omega;(3)}(\omega - \omega_1 - \omega_2, \omega_2, \omega_1)$  is taken from [42]:

$$\begin{aligned} \chi^3(-\omega; \omega - \omega_1 - \omega_2, \omega_2, \omega_1) &= \frac{4\pi^3 N_0}{3\varepsilon_0 h^3} \left( \left[ \sum_{\beta \neq 0} \frac{\omega_{0\beta} - \omega_2 - \omega_1 + i\Gamma}{(\omega_{0\beta} - \omega_2 - \omega_1)^2 + \Gamma^2} \right. \right. \\ &\quad \times \left[ \sum_{\alpha} \frac{\mu_{0\alpha}\mu_{\alpha\beta}}{\omega_{0\alpha} - \omega} \right] \left[ \sum_{\alpha'} \frac{\mu_{0\alpha'}\mu_{\alpha'\beta}}{\omega_{0\alpha'} - \omega_1} \right] \\ &\quad \left. \left. - \left[ \sum_{\alpha} \frac{\mu_{0\alpha}\mu_{\alpha 0}}{\omega_{0\alpha} - \omega} \right] \left[ \sum_{\alpha'} \frac{\mu_{0\alpha'}\mu_{\alpha' 0}}{(\omega_{0\alpha'} - \omega_2)(\omega_{0\alpha'} - \omega_1)} \right] \right) \right). \end{aligned} \quad (4.13)$$

parameter	value
intermediate state resonance energy $\omega_{01}$ [ $s^{-1}$ ]	$68045 \times (2\pi c) \times 10^2$
intermediate state resonance energy $\omega_{02}$ [ $s^{-1}$ ]	$83890 \times (2\pi c) \times 10^2$
two photon resonance energy $\omega_{03}$ [ $s^{-1}$ ]	$80119 \times (2\pi c) \times 10^2$
two photon resonance energy $\omega_{04}$ [ $s^{-1}$ ]	$79200 \times (2\pi c) \times 10^2$
two photon resonance energy $\omega_{05}$ [ $s^{-1}$ ]	$78120 \times (2\pi c) \times 10^2$
two photon resonance energy $\omega_{06}$ [ $s^{-1}$ ]	$88843 \times (2\pi c) \times 10^2$
dipole moment $\mu_{01}$ [ $Cm$ ]	$3.4 \times q_{el} \times 10^{-7}$
dipole moment $\mu_{02}$ [ $Cm$ ]	$-2.6 \times q_{el} \times 10^{-7}$
dipole moment $\mu_{13}$ [ $Cm$ ]	$9.9 \times q_{el} \times 10^{-7}$
dipole moment $\mu_{14}$ [ $Cm$ ]	$8.0 \times q_{el} \times 10^{-7}$
dipole moment $\mu_{15}$ [ $Cm$ ]	$1.35 \times q_{el} \times 10^{-6}$
dipole moment $\mu_{16}$ [ $Cm$ ]	$-4.1 \times q_{el} \times 10^{-6}$
dipole moment $\mu_{23}$ [ $Cm$ ]	$-2.8 \times q_{el} \times 10^{-6}$
dipole moment $\mu_{24}$ [ $Cm$ ]	$-4.7 \times q_{el} \times 10^{-7}$
dipole moment $\mu_{25}$ [ $Cm$ ]	$-9.2 \times q_{el} \times 10^{-7}$
dipole moment $\mu_{26}$ [ $Cm$ ]	$-1.85 \times q_{el} \times 10^{-6}$
two photon resonance width $\Gamma$ [ $s^{-1}$ ]	$0.74 \times (2\pi c) \times 10^2$
gas number density $N_0$ [ $m^{-3}$ ]	$2.7 \times 10^{25}$

**Table 4.1.:** Numerical values for the parameters of the nonlinear dispersion according to Equation (4.13)

Here  $\omega_{0\alpha}$  and  $\omega_{0\beta}$  are the single and two-photon resonance frequencies, respectively, and  $\mu_{0\alpha}$  and  $\mu_{\alpha\beta}$  are dipole moments for ground-intermediate and intermediate-final state transitions. Furthermore,  $\Gamma$  denotes the line width and  $N_0$  the atomic density. Numerical values are summarized in Table 4.1. The nonlinear dispersion follows from standard quantum mechanical calculations [45] by additionally accounting for enhancement of the susceptibility due to two-photon resonances in xenon around 249 nm [41]. Equation (4.13) applies to frequencies close to, but not at the resonances. For an exact calculation of the susceptibility the time dependent Schrödinger equation has to be solved (see Section 5). Therefore, the functional dependency and values of  $\chi^{(3)}$  used here are just a semi-qualitative description, allowing to study the effect of nonlinear dispersion on the general compression scheme.

#### 4.4. (1+1)-dimensional setup

In a first approach we want to investigate purely temporal influence of the dispersive nonlinearity on pulse dynamics, thus skipping the transverse spatial derivatives ( $\nabla_{\perp}^2$ )

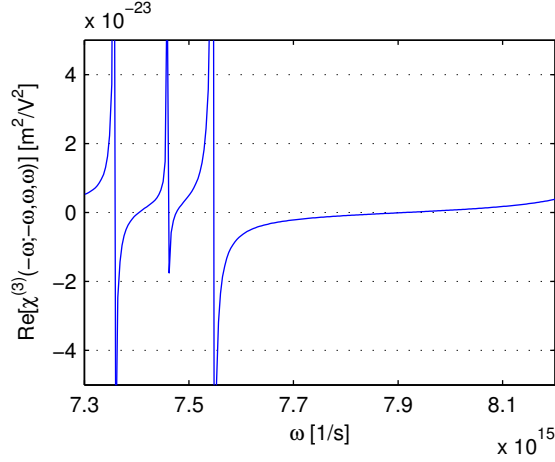


**Figure 4.4.:** Frequency dependence of the nonlinearity

in Equation (4.11). Even if the numerical solution of this equation is straightforward, it does not elucidate the underlying mechanisms for compression. In order to get some deeper insight, we include subsequently increasing orders of nonlinear dispersion, originating from a Taylor expansion around the central frequency  $\omega_0$ :

$$\chi^{(3)}(-\omega; \omega - \omega_1 - \omega_2, \omega_2, \omega_1) = \chi_0^{(3)} + \chi_1^{(3)}\bar{\omega}_1 + \chi_2^{(3)}\bar{\omega}_2 + \chi_3^{(3)}\bar{\omega} + \dots, \quad (4.14)$$

where  $\bar{\omega}_j = \omega_j - \omega_0$  and

$$\begin{aligned} \chi_0^{(3)} &= \chi^{(3)}(-\omega_0; -\omega_0, \omega_0, \omega_0), \\ \chi_{1,2}^{(3)} &= \partial_{\omega_{1,2}} \chi^{(3)}(-\omega; \omega - \omega_1 - \omega_2, \omega_2, \omega_1)|_{\omega_1=\omega_2=\omega=\omega_0}, \\ \chi_3^{(3)} &= \partial_{\omega} \chi^{(3)}(-\omega; \omega - \omega_1 - \omega_2, \omega_2, \omega_1)|_{\omega_1=\omega_2=\omega=\omega_0}. \end{aligned}$$

By doing so, we are able to attribute specific effects to the corresponding orders of nonlinear dispersion. In a first step, we neglect nonlinear dispersion ( $\chi_{1,2,3}^{(3)} = 0$ ) and explain the basic mechanisms of compression occurring in this case. In a second step, first order terms of nonlinear dispersion are included and their influence upon compression is investigated. Finally, the results are compared with the ones obtained from the fully dispersive (1+1)-dimensional model.

As mentioned above, we are interested in setups with negative  $n_2 \sim \chi^{(3)}$ , which can be found near resonances in Xe [see Figure 4.4]. So for the coming simulations, we introduce the abbreviation  $\omega_{--} = 7.73 \times 10^{15} \text{ s}^{-1}$  for the characteristic central frequency ensuring a negative  $n_2$  and additionally  $\omega_{00} = 7.91 \times 10^{15} \text{ s}^{-1}$  for investigations with vanishing  $n_2$ . That is, a laser pulse with central frequency  $\omega_0 = \omega_{--}$  experiences defocusing as well as effects originating from nonlinear dispersion, whereas a pulse with central frequency  $\omega_0 = \omega_{00}$  lacks the usual Kerr effect  $\sim n_2 = 0$  and only undergoes nonlinear dispersive modulations.

### 4.4.1. Model equations

#### 4.4.1.1. The NLS equation

We now summarize approximations to Equation (4.11) without the transverse Laplacian and here deal with the one dimensional nonlinear Schrödinger (NLS) equation. First, only the leading order of linear dispersion is kept, that is

$$k(\omega) - k_0 - k_1\bar{\omega} \approx k_2\bar{\omega}^2/2. \quad (4.15)$$

Second, we neglect nonlinear dispersion and due to the smallness of the imaginary part  $\text{Im}[\chi_0^{(3)}] \ll \text{Re}[\chi_0^{(3)}]$  (see Table 4.2) we have

$$\chi^{(3)}(-\omega; \omega - \omega_1 - \omega_2, \omega_2, \omega_1) \approx \text{Re}[\chi_0^{(3)}]. \quad (4.16)$$

Finally we neglect the dispersion of the linear refractive index  $n(\omega) \approx n(\omega_0) = n_0$ . Together with the definition of the wave number  $k(\omega) = \omega n(\omega)/c$ , the frequency dependency of the prefactor of the nonlinearity can be omitted:

$$\frac{\omega^2}{c^2 k(\omega)} = \frac{\omega_0 + \bar{\omega}}{cn_0} = \frac{\omega_0}{cn_0}, \quad (4.17)$$

for

$$\omega_0 \gg \bar{\omega}, \quad (4.18)$$

which is the physical condition justifying the applied approximations. Transforming back to time domain gives

$$\partial_z \mathcal{E} = -i \frac{k_2}{2} \partial_t^2 \mathcal{E} + i \frac{\omega_0}{c_0} n_2 |\mathcal{E}|^2 \mathcal{E}, \quad (4.19)$$

where we introduced the nonlinear refractive index  $n_2 = 3\text{Re}[\chi_0^{(3)}]/4n_0^2\epsilon_0 c$ . Equation (4.19) is the well known nonlinear Schrödinger equation. Since the NLS equation offers a rich variety of propagation effects, we have to identify our simulation parameters which lead to the desired compression. We therefore present two well studied effects, which can be used to estimate suitable input conditions for pulse compression. Note that on this strong approximation of the pure NLS equation we will treat the case  $\omega_0 = \omega_{--}$  ( $n_2 < 0$ ) only, since  $n_2$  vanishes for  $\omega_0 = \omega_{00}$ .

#### 4.4.1.2. The NLSND equation

In order to get a qualitative idea of the action of nonlinear dispersion, we use the expansion of the nonlinear susceptibility  $\sim \chi^{(3)}$  up to first order derived in Equation (4.14) and keep all other previously made approximations. It turns out (see Table 4.2) that  $\text{Im}[\chi_i^{(3)}] \ll \text{Re}[\chi_i^{(3)}]$ . Additionally,  $|\chi_3^{(3)}| \ll |\chi_{1,2}^{(3)}|$  and since  $\Delta\bar{\omega} \sim \Delta\bar{\omega}_{1,2}$ , the dispersive

	$\omega_0 = 7.73 \times 10^{15} \text{ s}^{-1}$	$\omega_0 = 7.91 \times 10^{15} \text{ s}^{-1}$
$k_2 \text{ [s}^2/\text{m]}$	$7.6 \times 10^{-28}$	$8.2 \times 10^{-28}$
$\text{Re}[\chi_0^{(3)}] \text{ [m}^2/\text{V}^2]$	$-1.7 \times 10^{-24}$	$-2.2 \times 10^{-26}$
$\text{Im}[\chi_0^{(3)}] \text{ [m}^2/\text{V}^2]$	$1.0 \times 10^{-27}$	$5.0 \times 10^{-28}$
$n_2 \text{ [cm}^2/\text{W]}$	$-0.47 \times 10^{-17}$	$-1.4 \times 10^{-20}$
$P_{cr} \text{ [W]}$	$2.0 \times 10^7$	$6.4 \times 10^9$
$\text{Re}[\chi_1^{(3)}] \text{ [m}^2\text{s}/\text{V}^2]$	$6.0 \times 10^{-39}$	$3.8 \times 10^{-39}$
$\text{Im}[\chi_1^{(3)}] \text{ [m}^2\text{s}/\text{V}^2]$	$-3.0 \times 10^{-42}$	$1.2 \times 10^{-43}$
$\text{Re}[\chi_2^{(3)}] \text{ [m}^2\text{s}/\text{V}^2]$	$6.2 \times 10^{-39}$	$3.7 \times 10^{-39}$
$\text{Im}[\chi_2^{(3)}] \text{ [m}^2\text{s}/\text{V}^2]$	$-3.1 \times 10^{-42}$	$1.8 \times 10^{-44}$
$\text{Re}[\chi_3^{(3)}] \text{ [m}^2\text{s}/\text{V}^2]$	$-1.7 \times 10^{-40}$	$1.2 \times 10^{-40}$
$\text{Im}[\chi_3^{(3)}] \text{ [m}^2\text{s}/\text{V}^2]$	$1.5 \times 10^{-43}$	$1.0 \times 10^{-43}$

**Table 4.2.:** Parameters used in the simulations. At center frequency  $\omega_0 = \omega_{--} = 7.73 \times 10^{15} \text{ s}^{-1}$  we find a strong negative Kerr nonlinearity, whereas at  $\omega_0 = \omega_{00} = 7.91 \times 10^{15} \text{ s}^{-1}$   $n_2$  is almost zero.

nonlinearity can be further simplified to

$$\chi^{(3)}(-\omega, \omega - \omega_1 - \omega_2, \omega_2, \omega_1) \approx \text{Re}[\chi_0^{(3)}] + \text{Re}[\chi_1^{(3)}] \bar{\omega}_1 + \text{Re}[\chi_2^{(3)}] \bar{\omega}_2. \quad (4.20)$$

Furthermore, in the nonlinearity of Equation (4.11) only terms of first order in  $\bar{\omega}$  are kept and  $\bar{\omega} \text{Re}[\chi^{(3)}](-\omega_0; \omega_0, \omega_0, -\omega_0) \ll \omega_0 (\text{Re}[\chi_1^{(3)}] \bar{\omega}_1 + \text{Re}[\chi_2^{(3)}] \bar{\omega}_2)$  holds (see Table 4.2). With these simplifications, transforming back to time domain leads to

$$\partial_z \mathcal{E} = -i \frac{k_2}{2} \partial_t^2 \mathcal{E} + i \gamma |\mathcal{E}|^2 \mathcal{E} - \delta |\mathcal{E}|^2 \partial_t \mathcal{E}, \quad (4.21)$$

where we introduced  $\delta = 3\omega_0 (\text{Re}[\chi_1^{(3)}] + \text{Re}[\chi_2^{(3)}]) / 4n_0^2 c^2 \varepsilon_0$ . The new term  $\sim \delta$  (compared to the NLS equation) is a so-called wave breaking term. It acts like an intensity dependent group velocity and shifts zones with higher intensity stronger to the rear/front of the pulse, depending on the sign of  $\delta$  ( $\pm$ , respectively). It is interesting to note that a similar term can be obtained for non-dispersive nonlinearities beyond slowly varying envelope approximation, but with a much smaller prefactor.

### 4.4.2. Estimating compression parameters via modulational instability (MI)

The phenomenon of modulational instability [91, 92] is responsible for an inherent instability of the propagation of a continuous wave background for certain values of  $k_2$  and  $n_2$ , and originates from the interplay of nonlinear (SPM) and dispersive (GVD) effects. This instability (MI) leads to the splitting of the continuous wave into a train of pulses with a well defined period usually fixed by the maximum of the instability growth rate. That property will be exploited to approximate the simulation parameters needed for compression.

Applying a standard linearization approach [93] to Equation (4.19) and Equation (4.21) for the perturbed steady state

$$\mathcal{E} = \left( \sqrt{I_0} + p(z, t) \right) e^{i\gamma I_0 z}, \quad (4.22)$$

where  $I_0$  is the background intensity and  $p$  the perturbation expressed as

$$p(z, t) = a_1 e^{i(Kz - \Omega t)} + a_2 e^{-i(Kz - \Omega t)} \quad (a_1, a_2 \ll \sqrt{I_0}) \quad (4.23)$$

leads to the dispersion relation for the perturbation wave number  $K$  and perturbation frequency  $\Omega$

$$K = \delta I_0 \Omega \pm \sqrt{\frac{k_2^2 \Omega^4}{4} + k_2 \gamma I_0 \Omega^2}. \quad (4.24)$$

Temporal modulations with  $\Omega$  grow, whenever the corresponding wave number  $K$  possesses imaginary contributions. These define the instability growth rate (or gain)

$$g(\Omega) = \text{Im} \left( \sqrt{\frac{k_2^2 \Omega^4}{4} + k_2 \gamma I_0 \Omega^2} \right), \quad (4.25)$$

which reaches its maximum for

$$\Omega = \Omega_{max} = \pm \sqrt{\frac{2|\gamma|I_0}{k_2}}. \quad (4.26)$$

Since our center frequency  $\omega_0$  determines the values of  $k_2$  and  $\gamma$ , we are able to calculate the necessary intensity for a fixed, desired modulation frequency  $\Omega_{max}$  to occur. To achieve single peaked pulse compression, this frequency  $\Omega_{max}$  should be of the order of the inverse initial pulse duration. Of course, this can only be a rough approximation, because our input pulse is far from a constant background. However, those estimates turn out to be useful and quite reliable when compared to simulation results (see Section 4.4.4).

It is worth noting, that the growth rate  $g(\Omega)$  and therefore also the optimum frequency  $\Omega_{max}$  are equal for both cases of NLS and NLSND. This is approved numerically



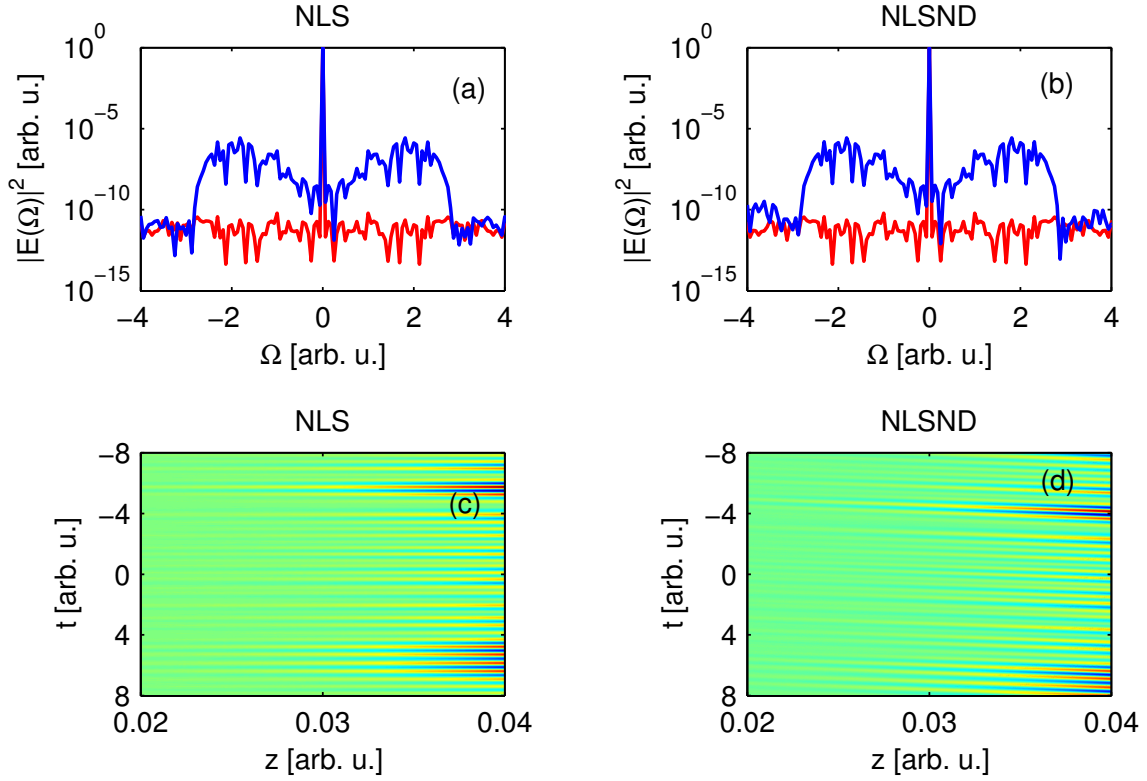


**Figure 4.5.:** Spectral intensity versus perturbation frequency  $\Omega$  for  $z = 0$  (red curves) and at propagation distance  $z = 0.04$  (blue curves) for (a) NLS and (b) NLSND. Evolution of temporal modulations on the constant background for (c) NLS and (d) NLSND. In (d) these modulations shift to later times upon propagation.

by plotting the initial ( $z = 0$ , red curves) and propagated ( $z = 0.04$ , blue curves) spectral intensity for the NLS and NLSND (see Figure 4.5(a) and (b), respectively). The only difference becomes apparent in the dispersion relation Equation (4.24), where the perturbation wave number  $K$  is purely real (propagating perturbations) or purely imaginary (growing perturbations) for the NLS ( $\delta = 0$ ), whereas  $K$  always has a real contribution  $\sim \delta I_0 \Omega$  in the NLSND case. These contributions correspond to additional transverse velocities of the growing perturbations oscillating at  $\Omega$ , resulting in their temporal shift upon propagation, which is numerically demonstrated in Figure 4.5(c) and (d).

Since we are able to tune the laser center frequency  $\omega_0$  and can therefore adjust  $\gamma \sim \omega_0 \chi^{(3)}$ , we can reach propagation regimes, in which the effect of MI does not occur, namely in the case where  $\gamma \approx 0$  ( $\omega_0 = \omega_{00}$ ). Then no statements concerning the pulses dynamics can be derived in the framework of MI theory. Nevertheless, as will be seen below, even in this case pulse self-compression is possible due to soliton formation.

### 4.4.3. Pulse compression via soliton dynamics

Another effect based on the interplay of SPM and GVD is the possibility of soliton formation in the NLS equation (see, e.g., [93]). The solitons with initial sech shape (in dimensionless units  $\varepsilon = \mathcal{E}/\sqrt{I_0}$ ,  $\tau = t/\tau_0$ ,  $\xi = z|k_2|/\tau_0^2$ )

$$\varepsilon(0, \tau) = N \operatorname{sech}(\tau) \quad (4.27)$$

are characterized by a single integer, the soliton order

$$N = \sqrt{\frac{|\gamma| I_0 \tau_0^2}{k_2}}, \quad (4.28)$$

where  $\tau_0$  is the pulse duration. For  $N = 2, 3, \dots$  the evolution patterns are known: the initial shape periodically undergoes several modulations, including compression at certain propagation distances. Moreover, these solitons are stable against perturbations on the soliton order  $N$  [94] as well as against perturbations of the initial pulse shape. That is, a perturbed input pulse  $\sim (N + \varepsilon)(\operatorname{sech}(\tau) + g(\tau))$  relaxes to the evolution pattern of the corresponding soliton upon propagation. So we can make use of the stability by fixing the soliton order  $N$  (and therefore the approximate evolution pattern) and subsequently estimating our input intensity  $I_0$  from Equation (4.28) for given  $\tau_0$ . In order to achieve compression, we want to have single peaked wave forms preserving their shape over long distances of propagation, so we should choose neither a too high  $N$  (strong compression over short propagation distance) nor a too low one (weak compression for long distances). Of course, the obtained intensity  $I_0$  is a lower boundary, since the energy dispersed away during the soliton formation process is no longer available for the soliton itself. The actual estimation is carried out below.

Concerning the NLSND equation, it is known [95] that Equation (4.21) still allows soliton solutions. These solitons naturally coincide with the ones for NLS equation for  $\delta \rightarrow 0$  and are therefore expected to be stable against perturbations as well. In the other limit case with  $\gamma = 0$  (and  $\delta \neq 0$ ) the amplitude of the soliton solution is given by

$$|\mathcal{E}_{\text{sol}}| \sim \sqrt{\frac{\lambda}{\sinh^2 \lambda t + \cosh^2 \lambda t}}, \quad (4.29)$$

with  $\lambda$  the family parameter which determines the intensity peak value and duration. Interestingly, the soliton fluence is a constant and can be evaluated as  $E_{\text{sol}} = \int |\mathcal{E}_{\text{sol}}|^2 dt = 2\pi k_2/\delta$ . An estimate for the minimal input fluence a Gaussian pulse has to carry for exciting a soliton follows from  $E_{\text{Gauss}} > E_{\text{sol}}$ , giving the condition  $\sqrt{2\pi} k_2/\delta < I_0 \tau_0$ .

#### 4.4.4. Simulation results

##### 4.4.4.1. NLS equation

Let us now present some results for the simulation of NLS equation. We assume Gaussian input pulses

$$\mathcal{E}(z = 0) = \sqrt{I_0} \exp\left(-t^2/\tau_0^2\right), \quad (4.30)$$

with intensity  $I_0$  and pulse duration  $\tau_0$  at center frequency  $\omega_0$ . First, we follow the approach to estimate optimum compression parameters via MI, according to Equation (4.26). Choosing  $\omega_0 = \omega_{--}$  and  $\tau_0 = 100$  fs implies  $k_2 = 7.6$  fs<sup>2</sup>/cm and  $\gamma = 1.2 \times 10^{-14}$  m/W. Now we demand  $\Omega_{max} = 2\pi/\tau_0\sqrt{2\ln 2} = 5.3 \times 10^{13}$  s<sup>-1</sup>, which gives  $I_0 = 9.0 \times 10^{13}$  W/m<sup>2</sup> for the initial intensity. Our second estimate is based on Equation (4.28). For  $N = 4$ , we find with the same parameters as above  $I_0 = 1.0 \times 10^{14}$  W/m<sup>2</sup> for the initial intensity.

Compared to numerical simulations, the above estimates give reasonable values for the optimum field intensity. For  $\tau_0 = 100$  fs and  $\omega_0 = \omega_{--}$  we find effective compression at  $I_0 = 2.1 \times 10^{14}$  W/m<sup>2</sup>. Simulation results are summarized in Figure 4.6(a) and 4.6(d). Figure (a) shows the intensity plotted against propagation distance  $z$  and pulse duration  $t$ . The propagation pattern can be determined to correspond to a 4th order soliton, undergoing the typical periodic modulations. Thus the dynamics can be clearly attributed to soliton propagation dynamics, giving that compression scheme its name. Figure 4.6(d) details the intensity of the initial pulse at  $z = 0$  m and after  $z = 1.4$  m of propagation. The full-width at half-maximum (FWHM) intensity is  $\tau_{FWHM} \sim 120$  fs at  $z = 0$  m and  $\tau_{FWHM} \sim 10$  fs at  $z = 1.4$  m, which corresponds to temporal compression by a factor of 12.

##### 4.4.4.2. NLSND equation

Let us now confront the above predictions on NLSND solutions with numerical simulations. As before, we simulate Gaussian input pulses with intensity  $I_0$ , pulse duration  $\tau_0$  and central frequency  $\omega_0$ . First we follow the approach to estimate parameters by MI and as mentioned earlier, obtain the same parameters as in the previous Section 4.4.4.1. For comparability with results from NLS we use again  $I_0 = 2.1 \times 10^{14}$  W/m<sup>2</sup> for the intensity at  $\tau_0 = 100$  fs for the pulse duration and  $\omega_0 = \omega_{--}$  as central frequency. The simulation results are presented in Figure 4.6(b) and 4.6(d). The temporal dynamics in (b) show the evolution pattern for a fourth order soliton which shifts to later times upon propagation, which can be attributed to the action of the wave breaking term  $\sim \delta$ . Figure 4.6(d) shows the initial pulse and the temporal profile at  $z = 1.4$  m. The initial pulse is compressed from  $\tau_{FWHM} = 117$  fs down to  $\tau_{FWHM} = 8$  fs at  $z = 1.4$  m, that is compression by a factor of 15. Again, the action of the additional intensity-dependent group velocity is apparent, since the peak value is occurring at later times. Furthermore, the peak value is somewhat decreased compared to the pure NLS case.

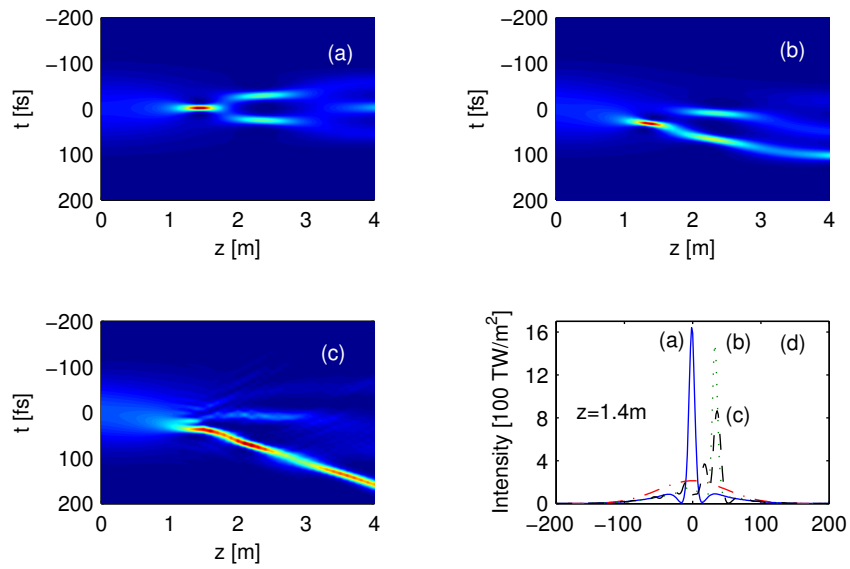


**Figure 4.6.:** (1+1)-dimensional simulation results for a Gaussian input pulse with  $I_0 = 2.1 \times 10^{14}$  W/m<sup>2</sup>,  $\tau_0 = 100$  fs and  $\omega_0 = \omega_{--}$ . Temporal dynamics for (a) NLS, (b) NLSND and (c) the full model. (d) shows the input pulse (red curve) and intensity profiles at  $z = 1.4$  m corresponding to (a) NLS (blue, solid curve), (b) NLSND (green dotted curve) and (c) full equation (black dashed curve).

#### 4.4.4.3. (1+1)-dimensional full model equation

In this section, simulation results for the fully dispersive (linear and nonlinear) wave equation (4.11) without transverse spatial dimensions are presented. The same simulation parameters as in the corresponding setup for NLSND are used.

Figure 4.6(c) and 4.6(d) show results for Gaussian input pulse with intensity  $I_0 = 2.1 \times 10^{14}$  W/m<sup>2</sup>, pulse width  $\tau_0 = 100$  fs at central frequency  $\omega_0 = \omega_{--}$ . Temporal dynamics in Figure 4.6(c) reveal the splitting of the initial pulse into a singly peaked waveform which is undergoing slight modulations in the peak value and shifted to later times upon propagation. According to the last sections, these modulations can be attributed to the soliton character of the evolution, whereas the shift to later times is due to corrections from the nonlinear dispersion. Figure 4.6(d) shows, that the pulse is compressed by a factor of 9 from initially  $\tau_{\text{FWHM}} = 117$  fs down to  $\tau_{\text{FWHM}} = 12.5$  fs at  $z = 1.4$  m.

It is important to underline that, as Figure 4.7(d) and (e) reveal, the pulse has contributions in the spectral range where the nonlinearity exhibits resonances, so that the whole model becomes questionable. Moreover, due to numerical issues, these resonances can not be resolved properly in the simulations, hence the results at propagation distances when the spectrum hits some resonances may not be reliable. Nevertheless, one can estimate the shortest pulse duration for which its spectrum stays in the non-resonant range. Starting from a center-frequency  $\omega_0 = \omega_{--}$  and assuming the allowed spectral width to be twice the distance to the nearest resonance at  $7.54 \times 10^{15}$  s<sup>-1</sup>, we get a minimal pulse duration of  $\tau_{\text{min}} \approx 15$  fs. So what can be claimed is, that upon propagation the pulse shortens at least down to 15 fs.

However, the similarity of the temporal dynamics for NLSND and for the full (1+1)-dimensional equation indicates, that the obtained dynamics are qualitatively correct and the error originating from the resonances is small. Thus, the main action of nonlinear dispersion can be summarized in shifting the maximum intensity region of the pulse to later times without altering the solitary character of the compression scheme.

#### 4.4.5. Pulse compression for vanishing Kerr coefficient

The original situation we are interested in is the propagation regime where  $\gamma \approx 0$ , which corresponds to a central frequency  $\omega_0 = \omega_{00}$  ( $\lambda_0 = 238$  nm as central wavelength).

If we fix the pulse duration to  $\tau_0 = 100$  fs and employ the NLSND model, the above considerations yield an estimate for the minimum intensity of  $I_0 = 1.6 \times 10^{15}$  W/m<sup>2</sup> necessary to trigger soliton formation. This is a lower boundary for the intensity and in order to see the ejection of a soliton from the input pulse we have to choose our initial intensity somewhat higher in the simulations, namely  $I_0 = 1.9 \times 10^{15}$  W/m<sup>2</sup>.

The temporal dynamics obtained in Figure 4.7(a) show the splitting of the initial pulse into a mainly single peaked structure which is shifted to later times upon prop-

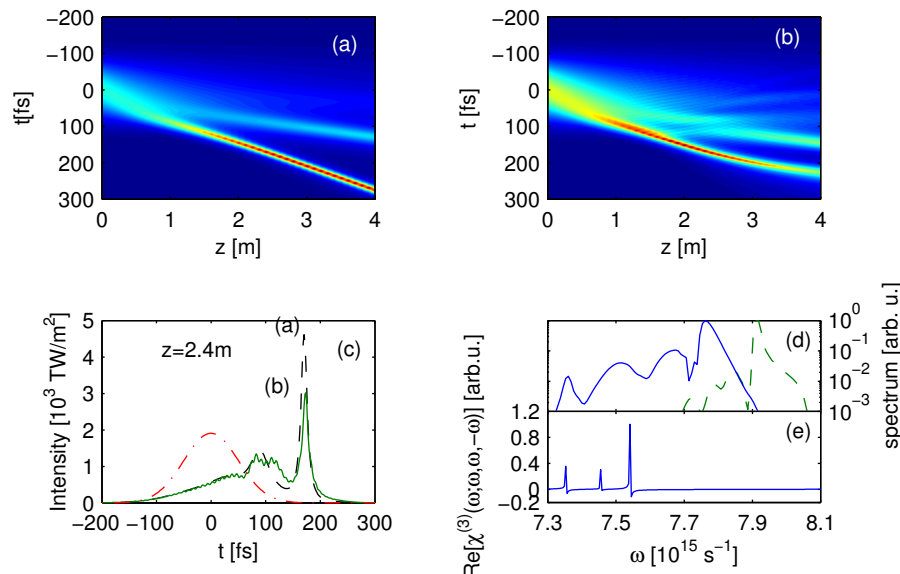


**Figure 4.7.:** Simulation results for Gaussian input with  $I_0 = 1.9 \times 10^{15} \text{ W/m}^2$ ,  $\tau_0 = 100 \text{ fs}$  and  $\omega_0 = \omega_{00}$  ( $\gamma \approx 0$ ). Temporal dynamics for (a) NLSND and (b) full equation. (c) details the input pulse (dash-dotted red line) and cuts for intensity profiles from (a) (dashed black line) and (b) (solid green line). In (d) spectra from the full equation are shown for  $\omega_0 = \omega_{--}$  at  $z = 1.40 \text{ m}$  (solid blue line) and for  $\omega_0 = \omega_{00}$  at  $z = 2.40 \text{ m}$  (dashed green line) (e) Real part of the nonlinearity  $\chi^{(3)}(-\omega; -\omega, \omega, \omega)$ .

agation. From Figure 4.7(c) we estimated the peak intensity and the FWHM pulse duration and compared these with the values for the soliton and were able to validate the assumption of a soliton being emitted from the initial pulse.

Further simulations suggest that it should be possible to produce solitons with shorter widths by just increasing the input intensity. However, at some point Equation (4.21) boards its validity, since for shorter pulses higher order linear and non-linear dispersion start to come into play.

Let us return to the full model equation. Figure 4.7(b) and (c) show the results for Gaussian input with intensity  $I_0 = 1.9 \times 10^{15} \text{ W/m}^2$ , pulse duration  $\tau_0 = 100 \text{ fs}$  at central frequency  $\omega_0 = \omega_{00}$ . The results are in good qualitative agreement with the ones for the NLSND equation. Temporal dynamics in Figure 4.7(b) show the ejection of the soliton whose width is determined from the cut in 4.7(c) at  $z = 2.4 \text{ m}$  to be  $\sim 12.5 \text{ fs}$ . In this setup, the pulse spectral intensity (see Figure 4.7(e), green dashed line) does not reach frequencies where  $\chi^{(3)}$  is resonant, and the found dynamics can be trusted.

Another point concerns the higher order nonlinearities  $P^{(5)} \sim \mathcal{E}^5, \dots$ , since the cubic term  $P^{(3)}$  is considerably smaller in the vicinity of  $\omega_{00}$  at which  $n_2$  almost vanishes. Nevertheless, it can be shown, that the length scales on which specific orders act can be estimated by  $|L_{P^{(3)}}/L_{P^{(5)}}| \simeq |P^{(5)}/P^{(3)}| \simeq |E/E_{at}|^2$  where  $E$  is the laser field

and  $E_{at} = 5 \times 10^{10}$  V/m [96]. We used field strengths  $E \simeq 0.4 \times 10^9$  V/m, giving  $|L_{P^{(3)}}/L_{P^{(5)}}| \simeq 2 \times 10^{-4}$ , so  $P^{(5)}$  is negligible. Furthermore, the pulses launched at  $\omega_{00}$  do have a spectral width, thus experiencing, e.g., a  $n_2 \approx 2.7 \times 10^{-23}$  m<sup>2</sup>/W at the half-maximum frequency due to dispersion of the nonlinearity, which is already comparable to usual values of  $n_2 \sim 1.0 \times 10^{-23}$  m<sup>2</sup>/W. Therefore, neglect of higher order nonlinearities is still justified for center frequencies close to  $\omega_{00}$ .

## 4.5. (3+1)-dimensional setup in radial symmetry

In this section, we want to investigate the full spatio-temporal propagation dynamics of Equation (4.11) in radial symmetry. As before, we use a simplified equation, the (3+1)-dimensional NLS equation, to estimate simulation parameters for the full equation. Once obtained, we check whether temporal compression still occurs with dispersive nonlinearity. Finally, we try to transfer the new compression mechanism found for  $\gamma \approx 0$  in the (1+1)-dimensional case to bulk configuration.

### 4.5.1. Nonlinear Schrödinger equation results

Let us first estimate parameters suitable for pulse compression in Equation (4.11). For this purpose, a simplified (3+1)-dimensional NLS equation is used, whose approximate dynamics can be described analytically by a two scale variational approach, followed by a standard MI (see Section 4.4.2) analysis which finally gives the desired parameters.

The (3+1)-dimensional NLS equation is obtained by including transverse coordinates in Equation (4.19) and accounting for radial symmetry ( $r^2 = x^2 + y^2$ ), giving

$$\partial_z \mathcal{E} = \frac{i}{2k_0 r} \partial_r r \partial_r \mathcal{E} - i \frac{k_2}{2} \partial_t^2 \mathcal{E} + i \frac{\omega_0}{c} n_2 |\mathcal{E}|^2 \mathcal{E}. \quad (4.31)$$

This equation is used to estimate the spatio-temporal dynamics for input Gaussian pulses

$$\mathcal{E} = \sqrt{I_0} \exp \left[ -\frac{t^2}{\tau_0^2} - \frac{r^2}{w_0^2} \right], \quad (4.32)$$

by a variational approach [97]. This approach minimizes the generalized action, leading to the dynamical system

$$\frac{w^3 k_0^2}{4} d_z^2 w = 1 + \frac{p \tau_0}{\sqrt{2} \tau}; \quad \frac{\tau^3}{4 k_2} d_z^2 \tau = k_2 - \frac{p \tau_0 \tau}{\sqrt{2} k_0 w^2}, \quad (4.33)$$

for the beam waist  $w(z)$  and pulse duration  $\tau(z)$ . Here,  $p = P_{in}/P_{cr}$  with the critical power  $P_{cr} = 2\pi c^2/\omega_0^2 n_0 |n_2|$ . The presence of a lens is included by the initial condition  $d_z w|_{z=0} = -w_0/f$ , where  $f$  is the focal length. This is combined with an additional MI analysis for plane waves [98] in the sense, that the maximal intensity resulting from the variational approach  $I_{max}$  serves as background plane-wave intensity. Then,

the growth rate for perturbations with frequency  $\bar{\omega}$  and transverse wave number  $k_{\perp}$

$$g(\bar{\omega}, k_{\perp}) = \text{Re} \left( \Omega \sqrt{2\omega_0 |n_2| I_{max} / c - \Omega^2} \right), \quad (4.34)$$

where  $\Omega^2 = k_2 \bar{\omega}^2 / 2 - k_{\perp}^2 / 2k_0$ , reaches its maximum for  $\bar{\omega}_{max}$  and  $k_{\perp}^{max}$ , being linked by

$$\bar{\omega}_{max} \simeq \sqrt{\frac{2\omega_0 |n_2| I_{max}}{k_2 c} + \frac{(k_{\perp}^{max})^2}{k_0 k_2}}. \quad (4.35)$$

A necessary condition [99] for MI to occur is  $k_{\perp}^{max} > \sqrt{2\pi}/w_0$  and  $\bar{\omega}_{max} > \sqrt{2\pi}/\tau_0$  for any given intensity. Fixing  $k_{\perp}^{max} = \sqrt{2\pi}/w^{min}$ , we use the highest perturbation frequency  $\omega_{high} = \sqrt{2\pi}/\tau^{min}$  to fulfill the condition for compression  $\omega^{high} \simeq \bar{\omega}^{max}$  [44].

In our case where  $\omega_0 = \omega_{-}$ , an optimum set of parameters is  $P_{in} = 5P_{cr}$  for input power ( $I_0 = 7.1 \times 10^{14}$  W/m<sup>2</sup>),  $\tau_0 = 100$  fs for pulse duration,  $w_0 = 0.3 \times 10^{-3}$  m as beam radius and a focal length of  $f = 1$  m.

### 4.5.2. Complete model results

In this section, results for the full model Equation (4.11) will be presented. We assume Gaussian input pulses with the simulation parameters given above. In Figure 4.8 simulation results are summarized, where 4.8(b) details the evolution of the initial Gaussian pulse into a singly peaked structure with minimal FWHM duration of 17 fs [see Figure 4.8(c)], which remains almost constant over propagation distances of  $\sim 0.5$  m. Figure 4.8(d) validates that the compression is not constrained to the on-axis intensity profiles but homogeneous in radial direction. Again, the pulse spectrum reaches regions where the nonlinearity is resonant and the previous discussion of validity has to be considered.

Further on, results for the configuration with  $\gamma \approx 0$  (central frequency  $\omega_0 = \omega_{00}$ ) are presented. As learned before, a MI analysis is not suitable to estimate dynamics in that case. Therefore parameters from the (1+1)-dimensional configuration previously applied to the NLSND model are taken for intensity and pulse width ( $I_0 = 1.9 \times 10^{15}$  W/m<sup>2</sup> and  $\tau_0 = 100$  fs, respectively). In order to keep transverse dynamics at bay, we choose a broad initial beam radius  $w_0 = 3$  mm, implying a long diffraction length of  $L_{diff} \sim 120$  m compared to typical propagation distances  $\sim 5$  m.

As revealed in Figure 4.9(a), the temporal dynamics agree well with the ones obtained in the (1+1)-dimensional setup for propagation distances up to  $z \sim 3$  m, for which the transverse profile remains constant [see Figure 4.9(b)]. Upon further propagation, the blue part ( $\omega > \omega_{00}$ ) of the pulse spectrum, experiencing a positive  $n_2 \sim \chi^{(3)}(-\omega; -\omega, \omega, \omega)$ , self-focuses and finally collapses at  $z \sim 4$  m. This slowly propagating, focusing part of the spectrum appears as high intensity zone at later times in the (on-axis) temporal dynamics plot at  $z \sim 3.5$  m [see Figure 4.9(a)]. Increasing the input intensity would be an option to rise effectivity of the soliton ejection



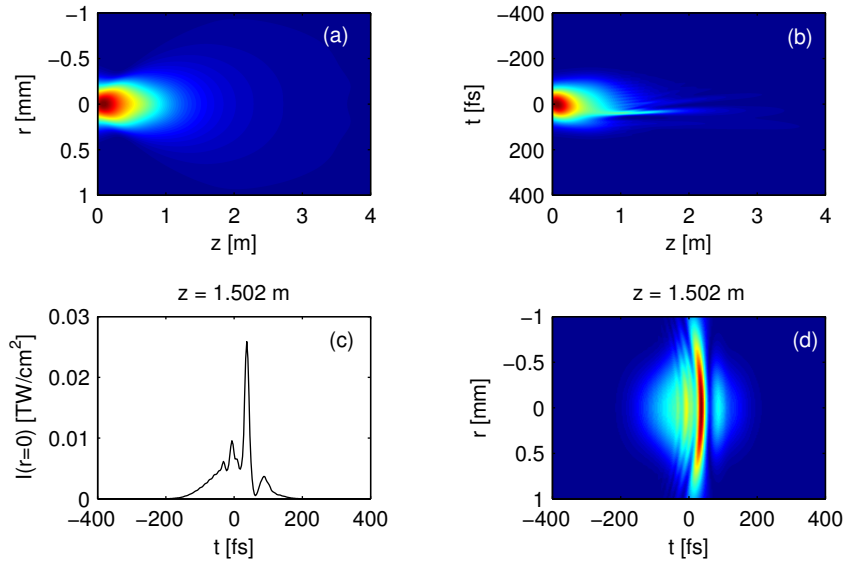


**Figure 4.8.:** Simulation results for the full model equation for Gaussian input pulses with  $P_{in} = 5P_{cr}$ ,  $\tau_0 = 100$  fs,  $w = 0.3$  mm and  $\omega_0 = \omega_{--}$  (243 nm): (a) transverse, (b) temporal dynamics; (c) intensity profile ( $\tau_{FWHM} \sim 17$  fs) and (d) transverse intensity distribution at  $z = 1.5$  m.

(scaling wave-breaking length  $\sim 1/I_0$  against self-focusing length  $\sim 1/\sqrt{I_0}$ ). However, this option is limited by plasma generation setting in, which is not described within our model.

## 4.6. Conclusions

We demonstrated the effect of nonlinear dispersion on solitary compression for normal GVD and negative  $n_2$ . We showed that the main effects of nonlinear dispersion can be captured by using first order Taylor expansion of the nonlinear susceptibility. The resulting shift of high intensity zones to later times does not change the qualitative mechanism of compression being mediated by MI. Because we are able to control MI in the unguided configuration by adjusting, e.g., the laser intensity, this mechanism provides an effective and simple way of compressing laser pulses by just focusing them into a gas cell. In the special case of vanishing  $n_2$  at center frequency, we showed that nonlinear dispersion enables an alternative compression mechanism. However, while working perfectly in purely temporal (1+1)-dimensional configuration, the important influence of spatial dynamics on temporal compression effects is underlined by the pulse self-collapse after soliton ejection in bulk configuration.

The main critique concerns the modeling of the dispersive nonlinearity  $\chi^{(3)}$ . We used a reasonable, albeit approximate expression from the literature. The exact description

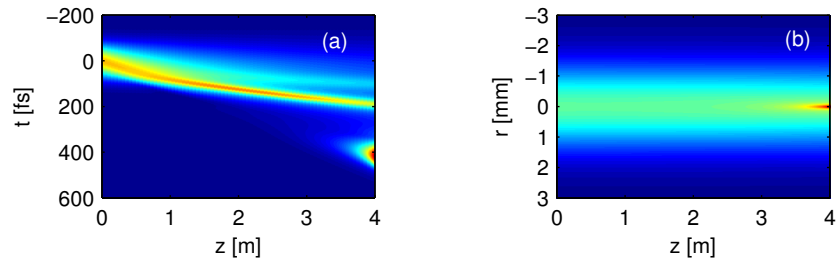


**Figure 4.9.:** Simulation results for full equation for Gaussian input with  $w_0 = 3$  mm and  $\omega_0 = \omega_{00}$  (238 nm),  $P_{in} = 4P_{cr}$  and  $\tau_0 = 100$  fs. (a) Temporal dynamics. (b) Transverse dynamics.

requires a full quantum mechanical simulation of the gas under irradiation of a laser pulse (see Section 5) and would give even quantitatively reliable results.

# 5. Towards a Quantum Mechanical Description of the Medium

## 5.1. Introduction

Accurate modeling of optical nonlinearities is crucial to explain a wide range of physically interesting effects. These include, e.g. sum frequency generation, spectral broadening due to self-phase modulation (see Chapter 4), various ionization processes (Chapter 3) and soliton formation. For incident laser light at low intensity  $I$ , ionization does not occur and the response of the medium is given by the induced polarization of the bound electrons. The polarization is usually expanded in a Taylor series for the electric field amplitude, which is truncated after the first non-linear term. In an isotropic medium, all even order terms vanish, rendering the third order contribution the lowest-order nonlinearity. A third-order nonlinearity leads to the well known optical Kerr effect, where the refractive index of the medium becomes intensity dependent via  $n = n_0 + n_2 I$ . This simple approach already allows to model nonlinear effects such as modulation instability, self focusing and self phase modulation [45], which manifest themselves in soliton formation [46], pulse compression [43] or self similar collapse [47]. The latter demonstrates an inherent problem when modeling laser propagation in two or more spatial dimensions, linked to the formally infinite increase ( $n_2 > 0$ ) of the refractive index for increasing intensity.

However, fundamental phenomena such as laser filamentation [39, 48–51] require saturation of the refractive index [50]. There are two ways to accomplish this saturation. First, in the response of the bound electrons, the third order Kerr term is not the only correction to  $n$  and higher order terms should be included when expanding the response [53, 54]. This assumption is supported by recent measurements of higher order Kerr terms  $n_{2i} I^i$  fulfilling the requirement of being negatively valued in order to saturate the refractive index for increasing intensity [55, 56]. On the other hand, for high enough intensity the medium gets ionized. The free electrons form a plasma, which gives rise to a negatively valued contribution to the refractive index [52] that is responsible for the overall saturation.

The fundamental nature of the question, whether higher order response terms of the bound electrons or the plasma response of ionized electrons saturate the refractive index is underlined by the ongoing controversy in modeling filamentation [60, 61]. Although there have been attempts to clarify the underlying mechanism for the saturation of the nonlinear refractive index [57–59], it is still an open question. Therefore,

the aim of our analysis is to rigorously describe the optical response of a medium under irradiation of a strong laser pulse. Especially in the intensity regime where the medium is partially ionized, strict distinction between responses from bound and ionized electrons has to be provided.

In Section 5.2 we define the problem more precisely, followed by the presentation of the quantum mechanical model for our analysis in Section 5.3. The methods Section 5.4 then gives technical details about numerics and performed calculations. After presentation and discussion of the results in Section 5.5, conclusions and outlook can be found in Section 5.6.

## 5.2. Stating the problem

We are interested in the (nonlinear) polarization of a gas under the influence of a strong laser, in particular in the intensity range where ionization can no longer be neglected. The atoms of the gas are assumed to be non-interacting, which allows us to consider the polarization of a single atom. Then, the total response of the gas is obtained by scaling the results with the number density of atoms in the gas. For simplicity, we investigate the polarization of atomic hydrogen in a linearly polarized laser pulse and restrict our analysis to one dimension. As it turns out, already such a crude simplification may provide fundamental insight into the mechanism that is responsible for saturation of the refractive index. More realistic 3D simulations are currently work in progress and not presented here. The dynamics of the electron are described quantum-mechanically. Then, the time dependent polarization  $P(t)$  of the atomic hydrogen gas is connected to the electronic wave function of the electron  $\Psi(x, t) = \langle x | \Psi(t) \rangle$  by

$$P(t) = \langle \Psi(t) | \hat{x} | \Psi(t) \rangle \rho_{at} q_e, \quad (5.1)$$

where  $\rho_{at} = 2.7 \times 10^{25} \text{ m}^{-3}$  is the atomic density at atmospheric pressure,  $q_e$  the electron charge and  $x$  ( $\hat{x}$ ) the position (operator) along our single dimension.

In order to distinguish between contributions originating from bound and ionized electrons, the wave function  $\Psi(x, t)$  is split into the part accounting for bound electrons  $\Psi_B(x, t)$  and the part accounting for ionized contributions in the continuum  $\Psi_C(x, t)$

$$\Psi(x, t) = \Psi_B(x, t) + \Psi_C(x, t). \quad (5.2)$$

The bound part  $\Psi_B(x, t)$  can be obtained by projecting the full wave function  $\Psi(x, t)$  on the (bound) eigenfunctions  $\phi_n(x)$  of the field free Hamiltonian  $\hat{H}_0$  (see Equation (5.21))

$$\hat{H}_0 \phi_n(x) = \varepsilon_n \phi_n(x) \quad (5.3)$$

$$\Psi_B(x, t) = \sum_n c_n(t) \phi_n(x) \quad c_n(t) = \langle \phi_n | \psi(t) \rangle. \quad (5.4)$$

The continuum part is then given by

$$\Psi_C(x, t) = \Psi(x, t) - \Psi_B(x, t). \quad (5.5)$$

This decomposes the total polarization  $P(t)$  into the following three parts according to Equation (5.1)

$$P(t) = P_{BB}(t) + 2Re[P_{BC}(t)] + P_{CC}(t) \quad (5.6)$$

$$P_{BB}(t) = \langle \Psi_B(t) | \hat{x} | \Psi_B(t) \rangle \rho_{at} q_e \quad (5.7)$$

$$P_{BC}(t) = \langle \Psi_B(t) | \hat{x} | \Psi_C(t) \rangle \rho_{at} q_e \quad (5.8)$$

$$P_{CC}(t) = \langle \Psi_C(t) | \hat{x} | \Psi_C(t) \rangle \rho_{at} q_e \quad (5.9)$$

Thus, once we have determined the electronic wave function  $\Psi(x, t)$ , we easily obtain the quantum-mechanically correct polarization and are provided with the desired distinction between bound and ionized contributions. In particular, we are then able to identify the mechanism responsible for saturation of the nonlinear refractive index. Therefore, our aim is the determination of the electronic wave function  $\Psi(x, t)$ .

In general however,  $\Psi(x, t)$  is not easily accessible, since its calculation is demanding. Thus, phenomenological expressions for  $P(t)$  are employed. All the approaches have in common the perturbative expansion of  $P(t)$  into a linear part  $P_{\text{Lin}}(t) = \varepsilon_0 \chi^{(1)} E(t)$  and a nonlinear part  $P_{\text{NL}}(t)$ :

$$P(t) = P_{\text{Lin}}(t) + P_{\text{NL}}(t), \quad (5.10)$$

where non-dispersive (over the spectral extension of the input field  $E(t)$ ) response coefficients in the linear as well as nonlinear part are assumed. The leading order term  $P_{\text{Lin}}$  is well established, therefore approximations for  $P(t)$  differ only in accounting for the nonlinear part. Three widely used approaches for  $P_{\text{NL}}$  are briefly revisited in the following.

The first approach includes the leading order nonlinear term from a Taylor expansion of  $P(t)$  in terms of the electric field  $E(t)$  via

$$P_{\text{NL}}(t) = \varepsilon_0 \chi^{(3)} E(t)^3. \quad (5.11)$$

Physically, this approach accounts for the optical Kerr effect and third harmonic generation, originating from the response of bound electrons. Thus it boards its validity latest at laser intensities, when charge generation sets in. That is, it is mainly used for modeling the nonlinear medium response for moderate intensities and finds application in describing e.g. soliton formation or pulse compression [43, 46] (also compare to Section 4 for a dispersive  $\chi^{(3)}$ ).

The second approach additionally takes the response of free charges into account

through

$$P_{\text{NL}}(t) = \varepsilon_0 \chi^{(3)} E(t)^3 - \frac{q_e^2}{m_e \omega_0^2} \rho(t) E(t). \quad (5.12)$$

Here,  $\rho(t)$  is the number density of generated charge carriers. This model finds its main applications in modeling laser filaments [39, 50, 51] and will be referred to as 'Standard Model' in the following. Here, the generation of electrons is usually modeled by multi-photon ionization [67]:

$$\partial_t \rho(t) = \sigma_K I^K (\rho_{\text{at}} - \rho(t)), \quad (5.13)$$

where  $K$  is the number of photons with energy  $\hbar\omega_0$  needed to provide the ionization energy.  $\sigma_K$  is the ionization cross-section and  $I$  the laser intensity. For comparison, see Section 3.2.3.1, where a field amplitude dependent ionization rate is used.

The third approach assumes a Taylor expansion of  $P_{\text{NL}}(t)$  in the electric field  $E(t)$  up to high orders

$$P_{\text{NL}}(t) = \varepsilon_0 \chi^{(3)} E(t)^3 + \varepsilon_0 \chi^{(5)} E(t)^5 + \varepsilon_0 \chi^{(7)} E(t)^7 + \varepsilon_0 \chi^{(9)} E(t)^9 + \dots \quad (5.14)$$

being valid for all field strengths. This approach has been proposed recently as an alternative to Equation (5.12) to explain saturation in the filamentation process [60] and will be termed 'High Order Kerr Effect (HOKE)' model throughout this chapter.

The task that naturally arises is to compare the predictions of those three models to the quantum mechanically exact statements from above. By doing so, we are then in the position to state, whether an approximate model for  $P_{\text{NL}}(t)$  can reasonably be applied or if full quantum mechanical calculations are mandatory to correctly describe  $P_{\text{NL}}(t)$ .

### 5.3. Model

We consider the single, non-relativistic electron in a hypothetical one dimensional hydrogen atom. In the center of mass coordinate system and corrected for Doppler shift, the electron's behavior in a linearly in x-direction polarized laser field is described by the Schrödinger equation

$$i\hbar \frac{\partial}{\partial t} \psi(x, t) = \left[ \frac{(\hat{p} - q_e A(x, t))^2}{2m_e} + q_e \phi(x, t) + V(x) \right] \psi(x, t), \quad (5.15)$$

with  $A(x, t)$  and  $\phi(x, t)$  being the vector and the scalar potential of the external electromagnetic field.  $q_e$  and  $m_e$  are the charge and the (reduced) mass of the electron and  $\hat{p} = -i\hbar \partial_x$  denotes the momentum operator in position representation. Since the laser wavelength  $\lambda = 800$  nm applied in the following is much larger than the extension of the atom  $a \approx 0.1$  nm, the dipole approximation [100]  $A(x, t) = A(t)$  and  $\phi(x, t) = \phi(t)$  holds.

When specifying  $A$  and  $\phi$  we have the freedom to choose a gauge. There are two

commonly used gauges, namely the length gauge (LG)

$$A(t) = 0 \quad \phi(t) = -xE(t) \quad (5.16)$$

and the velocity gauge (VG)

$$A(t) = -\int_{-\infty}^t dt' E(t') \quad \phi(t) = 0 \quad (5.17)$$

where  $E(t)$  is the electric field. They lead to Hamilton operators  $\hat{H}_{LG}$  and  $\hat{H}_{VG}$  in length and velocity gauge, respectively. However, the Schrödinger equation is invariant under the choice of gauge, since going over from VG to LG corresponds to a phase transformation for wave functions

$$\psi_{LG}(x, t) = e^{iA(t)x} \psi_{VG}(x, t) \quad (5.18)$$

and operators  $\hat{O}$

$$\hat{O}_{LG} = e^{iA(t)x} \hat{O}_{VG} e^{-iA(t)x}. \quad (5.19)$$

Thus, the observables we are interested in are gauge invariant

$$\langle \hat{O}_{LG} \rangle_{LG} = \langle e^{iA(t)x} \hat{O}_{VG} e^{-iA(t)x} \rangle_{LG} = \langle \hat{O}_{VG} \rangle_{VG} \quad (5.20)$$

We choose to work in VG Equation (5.17), which is motivated by the fact that VG has advantages over the LG in terms of numerical efforts [101]. Furthermore, space coordinate independent terms  $\propto A^2(t)$  in Equation (5.15) can be eliminated by another phase transformation [102]. Using atomic units ( $q_e = -1$ ,  $\hbar = 1$ ,  $m_e = 1$ ) we obtain the Schrödinger equation in velocity gauge

$$i \frac{\partial}{\partial t} \psi(x, t) = [H_0 + H_{\text{int}}] \psi(x, t) \quad (5.21)$$

$$H_0 = -\frac{\partial_x^2}{2} + V(x) \quad (5.22)$$

$$H_{\text{int}} = -iA(t)\partial_x. \quad (5.23)$$

We use a soft core atomic potential [103, 104]

$$V(x) = \frac{-1}{\sqrt{x^2 + \alpha^2}} \quad (5.24)$$

where the parameter  $\alpha$  is adjusted to  $\alpha = \sqrt{2}$  such that the ground state energy of the field free Hamiltonian  $H_0 = -\partial_x^2/2 + V(x)$  matches the ionization energy of hydrogen  $U_H = 0.5$  a.u.

## 5.4. Methods

### 5.4.1. Numerical implementation

The Schrödinger Equation (5.21) is integrated numerically by means of a Crank Nicholson scheme (see Appendix B). We assume the atom to be initially in its ground state obtained from Equation (5.3) and expose it to Gaussian laser pulses

$$E(t) = a_0 \cos(\omega_0 t + \phi) e^{-\frac{t^2}{\tau^2}} \quad (5.25)$$

$$= \frac{a_0}{2} (\exp(i(\omega_0 t + \phi)) + \exp(-i(\omega_0 t + \phi))) e^{-\frac{t^2}{\tau^2}} \quad (5.26)$$

with amplitude  $a_0$ , central frequency  $\omega_0 = 2\pi c/800$  nm, envelope phase  $\phi = \pi/2$  and duration  $\tau$ . In the following numerical analysis we will use three exemplary pulse durations  $\tau = 10$  fs,  $\tau = 20$  fs and  $\tau = 100$  fs. For each duration, we varied the intensity over a broad intensity interval ranging from  $I = 1.3 \times 10^{11}$  W/m<sup>2</sup> up to  $I = 1.3 \times 10^{18}$  W/m<sup>2</sup>. This ensures a purely linear response of the atom for small intensities and partial ionization of the atom for large intensities. Thus we obtain the electronic wave function for several intensities and pulse durations.

The necessary knowledge of the bound eigenfunctions for the distinction of the bound and continuum part is obtained by solving the eigenvalue Equation (5.3) numerically. We used the LAPACK routine 'dsbdr1' to obtain eigenfunctions up to order  $n = 52$ .

For all simulations we used a numerical box for the spatial coordinate of length  $L_x = 4000$  a.u. with  $N_x = 32768$  grid points. The results were numerically converged for a temporal resolution of  $\Delta t = 0.05$  a.u. for simulation times of 4000 a.u., 8000 a.u. and 40000 a.u. for the pulse durations  $\tau = 10$  fs,  $\tau = 20$  fs and  $\tau = 100$  fs respectively. From the results we extract the quantum mechanically correct polarizations.

### 5.4.2. Extracting the linear response $\chi^{(1)}$

We use the fact that for low intensity the linear polarization dominates over the non-linear part in Equation (5.10), since consecutive orders of a perturbative expansion of  $P(t)$  scale like  $|P^{(n+1)}/P^{(n)}| \simeq |E/E_{at}|$  for laser frequencies far from any resonances [96]. For our lowest intensity  $I = 1.3 \times 10^{11}$  W/m<sup>2</sup> we have  $E = 1 \times 10^7$  V/m and  $E_{at} \simeq 5 \times 10^{10}$  V/m. That is, for these low intensities the polarization is given by the linear term in Equation (5.10)

$$P_{\text{Lin}}(t) = P^{(1)}(t) = \epsilon_0 \chi^{(1)} E(t) \quad (5.27)$$

alone (remember non-dispersive coefficient  $\chi^{(1)}$ ). Equation (5.27) is most conveniently evaluated in Fourier space and  $\chi^{(1)}$  can be extracted from the contribution of the



polarization at the central laser frequency  $\omega_0$  via (see Appendix E.1)

$$\hat{P}^{(1)}(\omega_0) = \varepsilon_0 \chi^{(1)} \frac{a_0}{2} \sqrt{\pi \tau} e^{i\phi}. \quad (5.28)$$

### 5.4.3. Nonlinear polarization $P_{\text{NL}}$ and nonlinear refractive index

$n_{\text{NL}}$

Once we have the linear response  $\chi^{(1)}$ , we are able to extract the nonlinear polarization  $P_{\text{NL}}$  from our simulated polarization  $P(t)$

$$P_{\text{NL}}(t) = P(t) - \varepsilon_0 \chi^{(1)} E(t) \quad (5.29)$$

in time domain, or

$$\hat{P}_{\text{NL}}(\omega_0) = \hat{P}(\omega_0) - \varepsilon_0 \chi^{(1)} \frac{a_0}{2} \sqrt{\pi \tau} e^{i\phi} \quad (5.30)$$

in Fourier space at central laser frequency  $\omega_0$  (see Appendix E.1). Additionally we can define a nonlinear refractive index  $\hat{n}_{\text{NL}}(\omega_0)$ . We are inspired by the definition of the linear refractive index  $n$  in the field propagation Equation (2.28), where the second term on the right hand side  $i \frac{\omega}{c} \hat{n} \hat{E}(\omega)$  accounts for contributions linear in  $\hat{E}$ . We cast the nonlinear polarization term into an equivalent structure  $i \frac{\omega}{c} \frac{\hat{P}_{\text{NL}}}{2\varepsilon_0 n \hat{E}(\omega)} \hat{E}(\omega)$  and extract the nonlinear refractive index  $n_{\text{NL}}$  as

$$\hat{n}_{\text{NL}}(\omega_0) = \frac{\hat{P}_{\text{NL}}(\omega_0)}{2\varepsilon_0 n \hat{E}(\omega_0)}. \quad (5.31)$$

Furthermore, we can distinguish between contributions from bound, continuum and bound-continuum contributions in the nonlinear polarization according to Equation (5.6). Thus, this distinction carries over for the nonlinear refractive index

$$\hat{n}_{\text{NL},\alpha}(\omega_0) = \frac{\hat{P}_{\text{NL},\alpha}(\omega_0)}{2\varepsilon_0 n \hat{E}(\omega_0)} \quad (5.32)$$

where  $\alpha = \text{'BB'}$ ,  $\text{'BC'}$  or  $\text{'CC'}$ , where  $\text{'BB'}$  stands for bound-bound,  $\text{'BC'}$  for bound-continuum and  $\text{'CC'}$  for continuum-continuum contributions. Note, that the linear refractive index  $n$  results from  $\text{'BB'}$  contributions only.

We are now in the position to monitor the behavior of the nonlinear polarization and refractive index for increasing intensities. Especially, we can observe the expected saturation and change of sign of the nonlinearities and assign them to their respective origin according to the distinction made above. What follows is a comparison of the simulated results with the approximate  $\varepsilon$  models introduced in Section 5.2.

#### 5.4.4. Higher order nonlinearities

After we know the quantum mechanically correct nonlinear polarization, we want to compare it to the values one obtains when applying one of the models for the nonlinear polarization Equations (5.11)-(5.14). That is, we first have to extract parameters for such a description. For that purpose, we assume the Taylor expansion of the nonlinear polarization

$$P_{\text{NL}}(t) = P^{(3)}(t) + P^{(5)}(t) + P^{(7)}(t) + P^{(9)}(t) + \dots \quad (5.33)$$

$$= \varepsilon_0 \chi^{(3)} E(t)^3 + \varepsilon_0 \chi^{(5)} E(t)^5 + \varepsilon_0 \chi^{(7)} E(t)^7 + \varepsilon_0 \chi^{(9)} E(t)^9 + \dots \quad (5.34)$$

to hold, which should be true for low enough intensities. Here, the responses  $\chi^{(2j+1)}$  are taken to be instantaneous (time independent). Then, we use the exact simulation results on the l.h.s. to extract the parameters  $\chi^{(2j+1)}$ . There are two possible ways to do so.

Again, we use the fact, that the higher order responses  $\chi^{(2j+1)}$  will get important subsequently for increasing intensity. In Fourier space, these responses give rise to contributions  $\hat{P}^{(2j+1)}((2j+1)\omega_0)$  at the  $(2j+1)$ th harmonic frequency of  $\omega_0$  in the polarization (see Appendix E.2). We assume these harmonic peaks at  $(2j+1)\omega_0$  in the spectrum to be only due to the according response  $\chi^{(2j+1)}$ . Then, responses of different orders give contributions at different frequencies and the  $\chi^{(2j+1)}$  can be extracted from  $\hat{P}^{(2j+1)}((2j+1)\omega_0)$  by (see Appendix E.2):

$$\hat{P}^{(2j+1)}((2j+1)\omega_0) = \varepsilon_0 \chi^{(2j+1)} \sqrt{\pi} \left( \frac{a_0}{2} \right)^{2j+1} \tau \frac{1}{\sqrt{2j+1}} e^{i(2j+1)\phi}. \quad (5.35)$$

Note, that if one considers a peak in the polarization spectrum at fixed  $(2j_0+1)\omega_0$  which is due to  $\hat{P}^{(2j_0+1)}((2j_0+1)\omega_0)$  and increases intensity further and further, eventually contributions from  $\hat{P}^{(2j_1+1)}((2j_0+1)\omega_0)$  with  $j_1 > j_0$  will appear at that frequency and Equation (5.35) cannot be used. Contributions from  $\hat{P}^{(2j_1+1)}((2j_0+1)\omega_0)$  with  $j_1 < j_0$  play no role, since propagation effects of the input laser pulse are not included, leaving the input spectrum unchanged. Therefore it is important to evaluate Equation (5.35) for increasing intensity to render the initial assumption true. A second, potentially more severe problem is that the responses  $\chi^{(2j+1)}$  are determined at frequency  $(2j+1)\omega_0$ , that is, values of  $\chi^{(2j+1)}$  at frequency  $\omega_0$  may differ because the response is not instantaneous. To check this issue is the purpose of the second approach to calculate the  $\chi^{(2j+1)}$ .

Alternatively, the responses  $\chi^{(2j+1)}$  can be determined from the polarization spectrum at central laser frequency  $\omega_0$ , since all  $\hat{P}^{(2j+1)}$  also contribute to  $\hat{P}(\omega_0)$  (see Appendix E.1). Therefore, we consider Equation (5.34) in Fourier space at central laser frequency  $\omega_0$

$$\hat{P}_{\text{NL}}(\omega_0, I) = \hat{P}^{(3)}(\omega_0, I) + \hat{P}^{(5)}(\omega_0, I) + \dots + \hat{P}^{(2j+1)}(\omega_0, I) \quad (5.36)$$

where the l.h.s. again consists of the simulated nonlinear polarization for a given peak intensity  $I$  and the r.h.s. is given through (see Appendix E.1)

$$\hat{P}^{(2j+1)}(\omega_0, I) = \varepsilon_0 \chi^{(2j+1)} \sqrt{\pi} \tau e^{i\phi} \binom{2j+1}{j} \left(\frac{a_0}{2}\right)^{2j+1} \frac{1}{\sqrt{2j+1}}. \quad (5.37)$$

Here the intensity dependency enters via the the electric field amplitude  $a_0$ . Finally, the calculation of all  $\chi^{(2j+1)}$  corresponds to solving the linear system of equations

$$\hat{P}_{\text{NL}}(\omega_0, I_1) = \hat{P}^{(3)}(\omega_0, I_1) + \hat{P}^{(5)}(\omega_0, I_1) + \dots + \hat{P}^{(2j+1)}(\omega_0, I_1) \quad (5.38)$$

$$\hat{P}_{\text{NL}}(\omega_0, I_2) = \hat{P}^{(3)}(\omega_0, I_2) + \hat{P}^{(5)}(\omega_0, I_2) + \dots + \hat{P}^{(2j+1)}(\omega_0, I_2) \quad (5.39)$$

...

$$\hat{P}_{\text{NL}}(\omega_0, I_j) = \hat{P}^{(3)}(\omega_0, I_j) + \hat{P}^{(5)}(\omega_0, I_j) + \dots + \hat{P}^{(2j+1)}(\omega_0, I_j). \quad (5.40)$$

Here, we obtain the values of  $\chi^{(2j+1)}$  at central laser frequency  $\omega_0$ .

For the Standard Model Equation (5.12), which explicitly includes ionized electrons, the determination of the parameter  $\sigma_K$  in the charge Equation (5.13) remains. For hydrogen (ionization energy  $U_{\text{ion},H} = 0.5$  a.u.) in a  $\lambda_0 = 800$  nm laser we have ( $K\hbar\omega_0 = Khc/\lambda = U_{\text{ion},H}$ )  $K = 9$ .  $\sigma_K$  is adjusted such, that the charge at the end of the laser pulse according to Equation (5.13)  $\rho(t \rightarrow \infty)$  coincides with the charge obtained via  $\int |\Psi_C(x, t = t_{\text{max}})|^2 dx$  in the simulations.

To fix the model parameters  $\chi^{(2j+1)}$  and  $\sigma_K$ , we choose the simulation with peak intensity  $I = 32$  TW/cm<sup>2</sup> and pulse duration  $\tau = 20$  fs for reasons which get obvious in the next section.

## 5.5. Results and discussion

### 5.5.1. Linear response $\chi^{(1)}$

The linear response at central frequency  $\omega_0$  ( $\lambda = 800$  nm) was determined to be

$$\chi^{(1)} = 6.88 \times 10^{-4} + i9.73 \times 10^{-7}. \quad (5.41)$$

This value was obtained independently from simulations with  $\tau = 10$  fs,  $\tau = 20$  fs and  $\tau = 100$  fs for low intensities up to  $I = 5.12 \times 10^{15}$  W/m<sup>2</sup>. For higher intensities  $\hat{P}_{\text{NL}}$  becomes relevant and our approach Equation (5.28) is no longer suited for the extraction of  $\chi^{(1)}$ . Of course,  $\chi^{(1)}$  does not equal the analytical quantum mechanically correct value for hydrogen of  $\chi^{(1)} = 2.3 \times 10^{-4}$  [82] since we use a one dimensional model with a soft-core potential in contrast to the real coulomb potential.

### 5.5.2. Nonlinear polarization $P_{\text{NL}}$ and nonlinear refractive index

$$n_{\text{NL}}$$

The Figures 5.1, 5.2 and 5.3 show the nonlinear polarization  $\hat{P}_{\text{NL}}(\omega_0)$  and the nonlinear refractive index  $\hat{n}_{\text{NL}}(\omega_0)$  plotted against peak intensity for  $\tau = 10$  fs,  $\tau = 20$  fs and  $\tau = 100$  fs, respectively. Apart from the overall nonlinear polarization and refractive index, their constituting parts according to the distinction of bound and ionized contributions are shown. Since the nonlinear polarization and refractive index are closely related by Equation (5.31) and the results for different pulse durations  $\tau$  are qualitatively the same, the following argumentation for  $n_{\text{NL}}$  can be easily transferred to the nonlinear polarization or to different pulse durations.

$\hat{n}_{\text{NL}}(\omega_0)$  is shown in the right column of Figures 5.1, 5.2 and 5.3. We start with the observation that the real part of the total  $\hat{n}_{\text{NL}}(\omega_0)$  (label 'ALL') linearly rises with peak intensity for  $I < 15$  TW/cm<sup>2</sup>. This is more clearly visible in Figures 5.6, 5.7 and 5.8 in the next section.

For peak intensities around  $I \approx 15$  TW/cm<sup>2</sup> the real part of the total  $\hat{n}_{\text{NL}}(\omega_0)$  (label 'ALL') saturates and finally changes sign at intensities  $I \approx 30$  TW/cm<sup>2</sup>. This change of sign occurs at lower intensities for longer pulse durations  $\tau$  and at higher intensities for shorter pulse durations  $\tau$ . This non-instantaneous, i.e. time dependent effect is a first hint for plasma generation, which depends on the pulse duration.

The imaginary part of the total  $\hat{n}_{\text{NL}}(\omega_0)$  (absorption) is close to zero for low intensities (up to  $\sim 16$  TW/cm<sup>2</sup>) and increases when the real part of  $\hat{n}_{\text{NL}}$  changes sign.

An important observation is made at the intensity where the real part of the total  $\hat{n}_{\text{NL}}(\omega_0)$  changes sign. The  $\hat{n}_{\text{NL}}^{\text{BB}}(\omega_0)$  from bound electrons still is positive (see Figures 5.1 d), 5.2 d) and 5.3 d)), whereas  $\hat{n}_{\text{NL}}^{\text{CC}}(\omega_0)$  from the continuum electrons (see Figures 5.1 h), 5.2 h) and 5.3 h)) is negative, with an absolute value large enough to render the total  $\hat{n}_{\text{NL}}(\omega_0)$  negative. The positive contribution of the bound-continuum part does not qualitatively change the situation. This means, the continuum contributions, i.e. from ionized electrons, are responsible for the change of sign of the total  $\hat{n}_{\text{NL}}(\omega_0)$ .

The  $\hat{n}_{\text{NL}}^{\text{BB}}(\omega_0)$  from bound electrons also changes sign but at higher intensities ( $I \approx 40$  TW/cm<sup>2</sup> for  $\tau = 10$  fs and  $\tau = 20$  fs,  $I \approx 25$  TW/cm<sup>2</sup> for  $\tau = 100$  fs) compared to the sign change of  $\hat{n}_{\text{NL}}^{\text{CC}}(\omega_0)$  from continuum electrons. Nevertheless,  $\hat{n}_{\text{NL}}^{\text{BB}}(\omega_0)$ 's absolute value remains smaller than the one of  $\hat{n}_{\text{NL}}^{\text{CC}}(\omega_0)$  from continuum electrons, rendering the nonlinearity of the charge contributions the dominating one.

### 5.5.3. Extraction of higher order responses $\chi^{(2j+1)}$ and ionization cross-section $\sigma_K$

Let us now extract the coefficients  $\chi^{(2j+1)}$  and  $\sigma_K$  for the respective models for the nonlinear polarization  $\hat{P}_{\text{NL}}$ . In order to proceed, the determination of the higher order responses  $\chi^{(2j+1)}$  is performed in the following. First, the higher order Kerr coefficients  $\chi^{(2j+1)}$  are determined from the corresponding harmonic peaks at  $(2j+1)\omega_0$  according

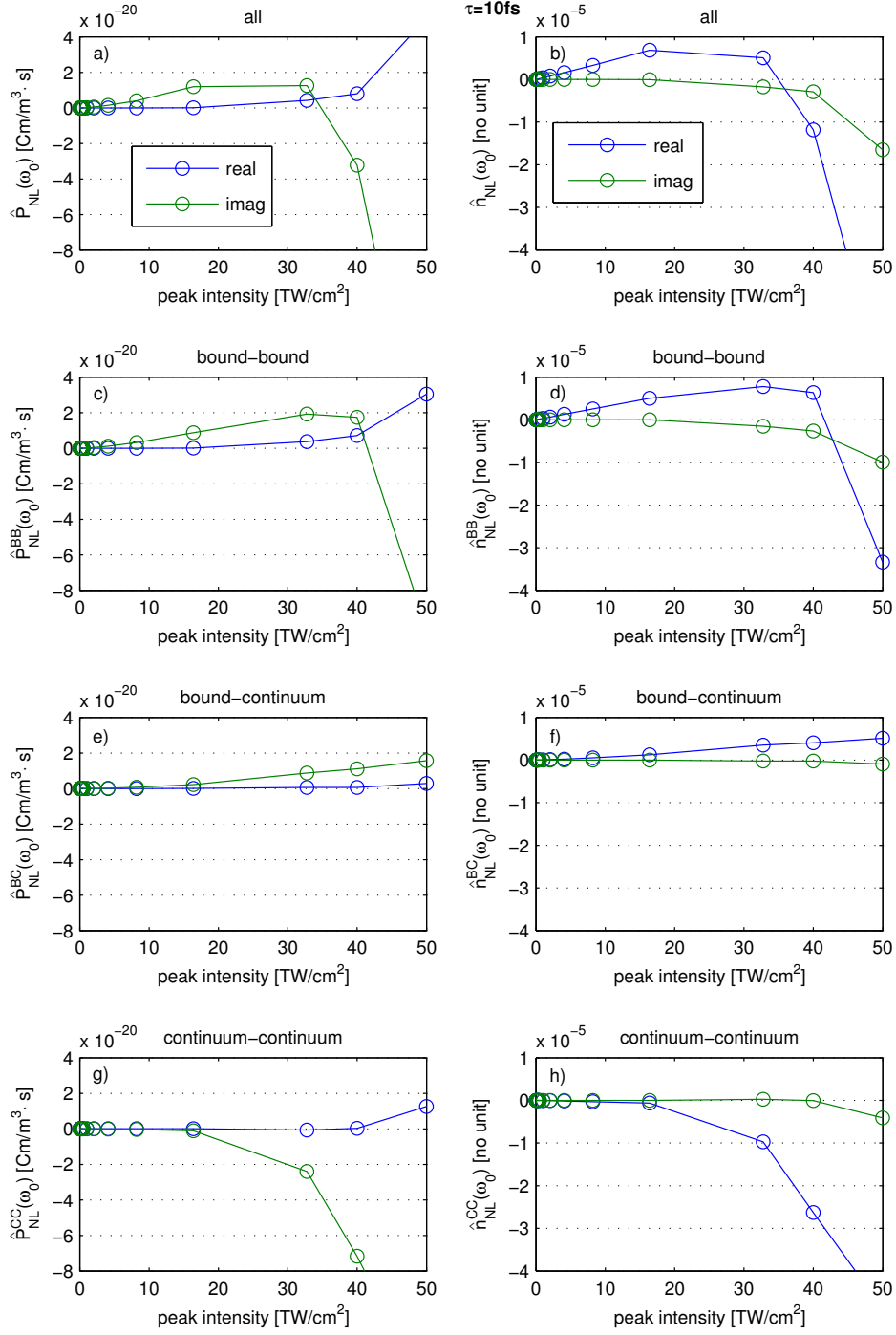


**Figure 5.1:** Quantum mechanical simulation results for nonlinear polarization  $\hat{P}_{NL}(\omega_0)$  and nonlinear refractive index  $\hat{n}_{NL}(\omega_0)$  for a pulse duration  $\tau = 10$  fs plotted against peak intensity. The left column displays the nonlinear polarization, the right column shows the nonlinear refractive index. a), b) show the overall value; c), d) contributions from bound part  $\hat{P}_{NL}^{BB}(\omega_0)$  and  $\hat{n}_{NL}^{BB}(\omega_0)$ ; e), f) contributions from bound-continuum part  $\hat{P}_{NL}^{BC}(\omega_0)$  and  $\hat{n}_{NL}^{BC}(\omega_0)$ ; g), h) contributions from continuum part  $\hat{P}_{NL}^{CC}(\omega_0)$  and  $\hat{n}_{NL}^{CC}(\omega_0)$  of the electronic wave function. Remember that we used an envelope phase of  $\phi = \pi/2$  for the input field, thus the nonlinear polarization appears rotated by  $\phi = \pi/2$  in the complex plane.

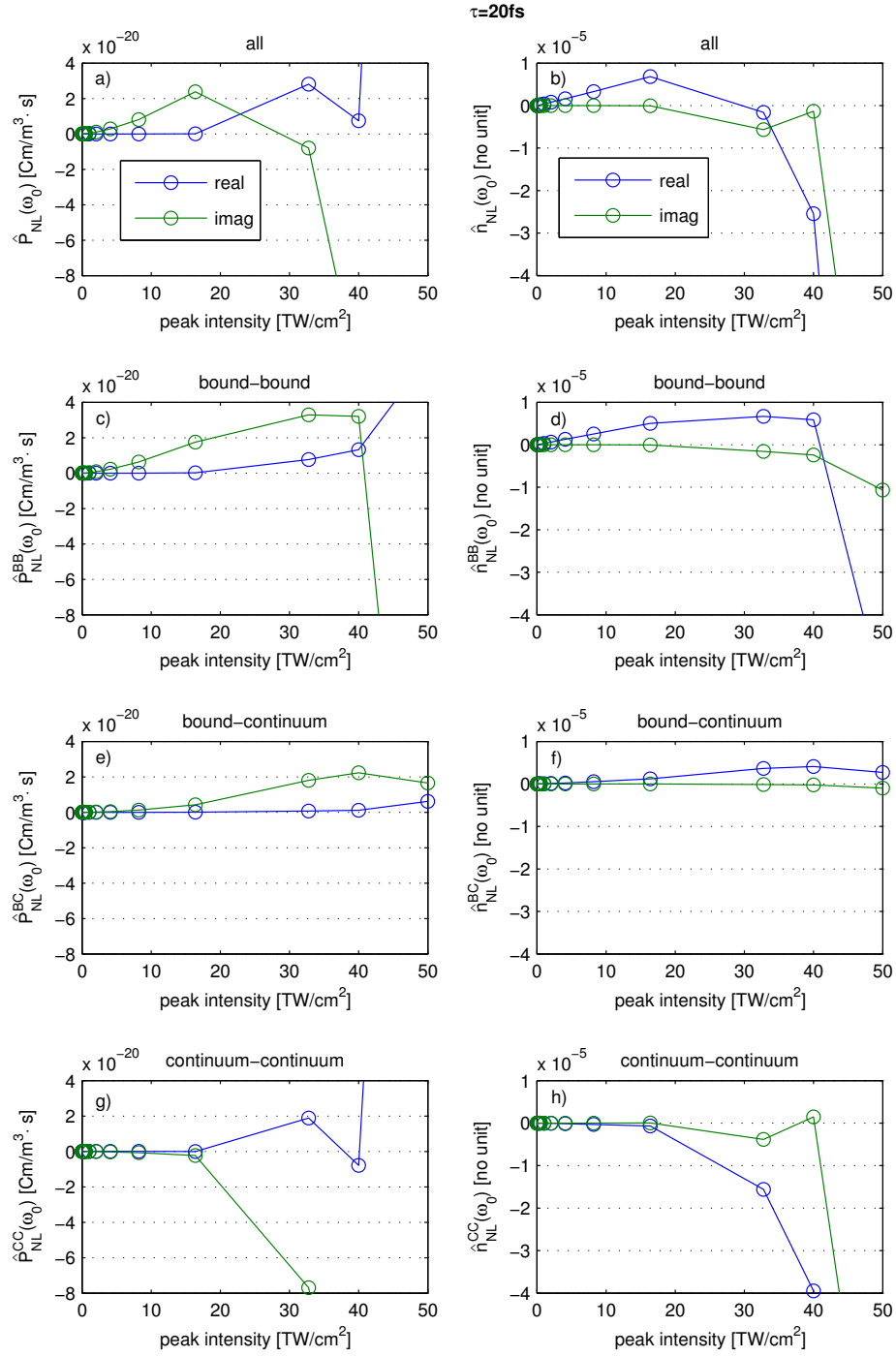


**Figure 5.2.:** Quantum mechanical simulation results for nonlinear polarization  $\hat{P}_{NL}(\omega_0)$  and nonlinear refractive index  $\hat{n}_{NL}(\omega_0)$  for a pulse duration  $\tau = 20$  fs plotted against peak intensity. The left column displays the nonlinear polarization, the right column shows the nonlinear refractive index. a), b) show the overall value; c), d) contributions from bound part  $\hat{P}_{NL}^{BB}(\omega_0)$  and  $\hat{n}_{NL}^{BB}(\omega_0)$ ; e), f) contributions from bound-continuum part  $\hat{P}_{NL}^{BC}(\omega_0)$  and  $\hat{n}_{NL}^{BC}(\omega_0)$ ; g), h) contributions from continuum part  $\hat{P}_{NL}^{CC}(\omega_0)$  and  $\hat{n}_{NL}^{CC}(\omega_0)$  of the electronic wave function. Remember that we used an envelope phase of  $\phi = \pi/2$  for the input field, thus the nonlinear polarization appears rotated by  $\phi = \pi/2$  in the complex plane.

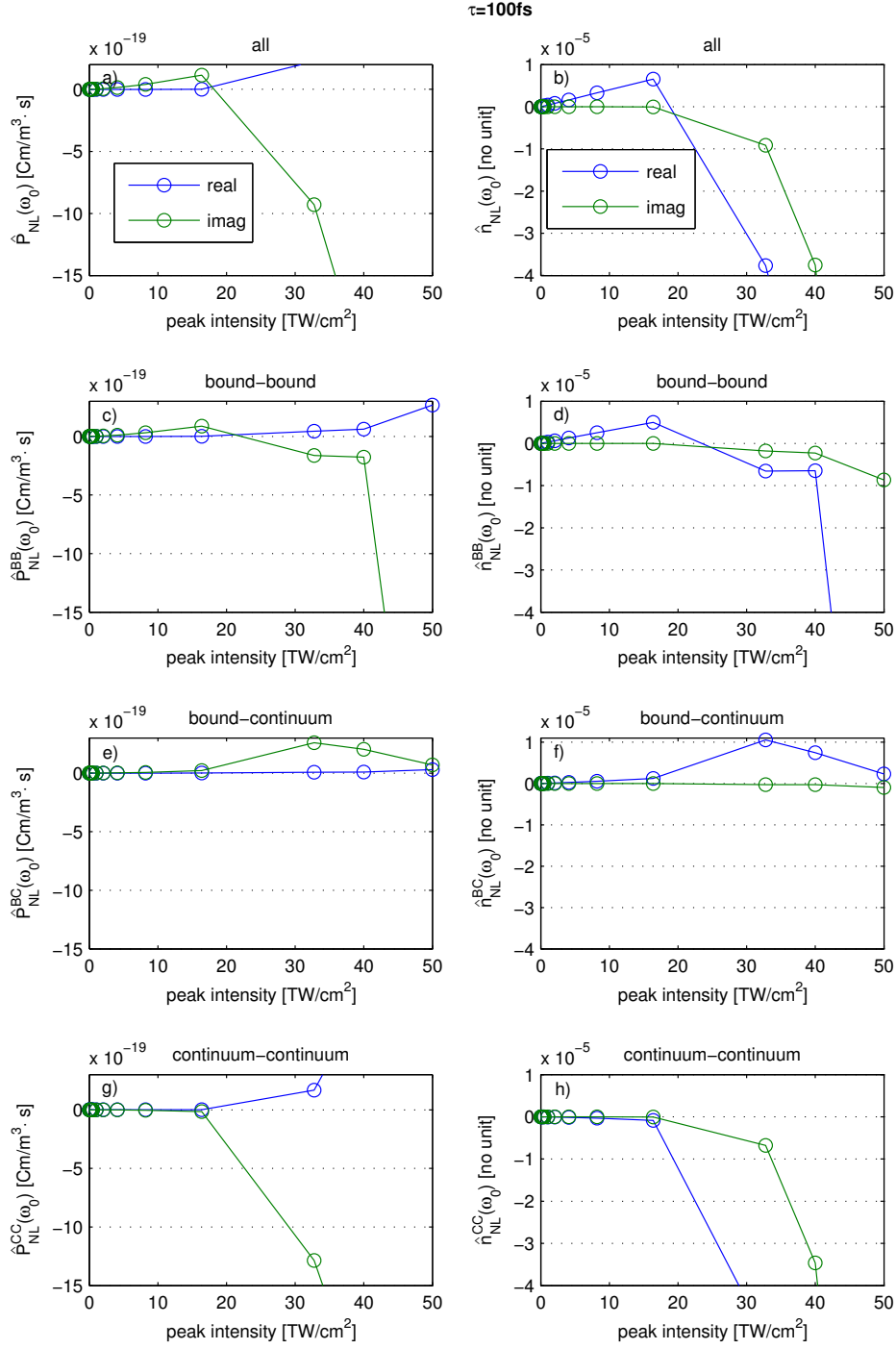


**Figure 5.3.:** Quantum mechanical simulation results for nonlinear polarization  $\hat{P}_{NL}(\omega_0)$  and nonlinear refractive index  $\hat{n}_{NL}(\omega_0)$  for a pulse duration  $\tau = 100$  fs plotted against peak intensity. The left column displays the nonlinear polarization, the right column shows the nonlinear refractive index. a), b) show the overall value; c), d) contributions from bound part  $\hat{P}_{NL}^{BB}(\omega_0)$  and  $\hat{n}_{NL}^{BB}(\omega_0)$ ; e), f) contributions from bound-continuum part  $\hat{P}_{NL}^{BC}(\omega_0)$  and  $\hat{n}_{NL}^{BC}(\omega_0)$ ; g), h) contributions from continuum part  $\hat{P}_{NL}^{CC}(\omega_0)$  and  $\hat{n}_{NL}^{CC}(\omega_0)$  of the electronic wave function. Remember that we used an envelope phase of  $\phi = \pi/2$  for the input field, thus the nonlinear polarization appears rotated by  $\phi = \pi/2$  in the complex plane.

to Equation (5.35). The results are presented in Figure 5.4, which shows the real and imaginary parts of the of the first four nonlinear responses  $\chi^{(3)}$ ,  $\chi^{(5)}$ ,  $\chi^{(7)}$  and  $\chi^{(9)}$ .

We deduce from Figure 5.4 a)-d), that for all pulse durations  $\tau = 10$  fs,  $\tau = 20$  fs and  $\tau = 100$  fs, defining  $\chi^{(3)}$  and  $\chi^{(5)}$  makes sense, since we obtain comparable peak-intensity independent values over a broad intensity range ( $I \sim 1 \times 10^{11} \dots \sim 2 \times 10^{15}$  W/cm<sup>2</sup> for  $\chi^{(3)}$  and  $I \sim 2 \times 10^{13} \dots \sim 2 \times 10^{15}$  W/cm<sup>2</sup> for  $\chi^{(5)}$ ).

Defining  $\chi^{(7)}$  seems to be meaningful for pulse durations  $\tau = 20$  fs and  $\tau = 100$  fs only, since we get intensity independent values over a comparably smaller intensity interval ( $I \sim 2 \times 10^{14} \dots \sim 3 \times 10^{15}$  W/cm<sup>2</sup>). For simulations with pulse duration  $\tau = 10$  fs we already encounter considerable dependence of  $\chi^{(7)}$  on the peak intensity, which renders any Taylor series approach meaningless.

Similarly, intensity independent values are obtained for  $\chi^{(9)}$ , at least for the pulse duration of  $\tau = 100$  fs. In contrast to the previous cases,  $\chi^{(9)}$  is dominated by its imaginary part for all cases  $\tau = 10$  fs,  $\tau = 20$  fs and  $\tau = 100$  fs. Usually, such considerable imaginary parts of the susceptibility, being responsible for absorption, occur close to resonances of the real part. In our case,  $\chi^{(9)}$  is evaluated at frequency  $9\omega_0$ , which corresponds to an energy of 0.511 a.u. This value is just above the ionization energy of 0.5 a.u., therefore just enough for an electron to absorb this energy and get ionized.

We also observe a dependence of the value of the higher order responses on pulse duration (Figure 5.4). Simulations with pulse durations  $\tau = 10$  fs suggest slightly different values than the simulations with  $\tau = 20$  fs and  $\tau = 100$  fs, for which they coincide. This indicates once more, that nonlinear dispersion is not negligible.

In summary, we conclude that the definition of higher order nonlinear responses is only meaningful for the low orders  $\chi^{(3)}$  and  $\chi^{(5)}$ , provided the pulse duration is sufficiently long. For comparison to the usually employed models, we extract the following values from Figure 5.4:

$$\chi^{(3)} = \left(4.3 \times 10^{-25} + i1.8 \times 10^{-27}\right) (m/V)^2 \quad (5.42)$$

$$\chi^{(5)} = -\left(8.1 \times 10^{-45} + i5.7 \times 10^{-47}\right) (m/V)^4 \quad (5.43)$$

$$[\chi^{(7)} = \left(5.8 \times 10^{-65} + i5.7 \times 10^{-67}\right) (m/V)^6]. \quad (5.44)$$

We now follow the alternative approach and extract the higher order responses  $\chi^{(2j+1)}$  at the central laser frequency  $\omega_0$  according to the system of Equations (5.40). Here, in order to determine  $n$  responses, we have to choose  $n$  different intensity values for the evaluation of  $\hat{P}^{(2j+1)}(I, \omega_0)$  on the r.h.s. We are guided by the results from Figure 5.4 to select these intensity values from an intensity range, where the responses we want to determine are peak intensity independent.

However, it turns out, that we are only able to calculate a  $\chi^{(3)}$  which is independent of the choice of used intensity values. We obtain

$$\chi^{(3)} = \left(2.3 \times 10^{-25} + i3.3 \times 10^{-28}\right) (m/V)^2. \quad (5.45)$$



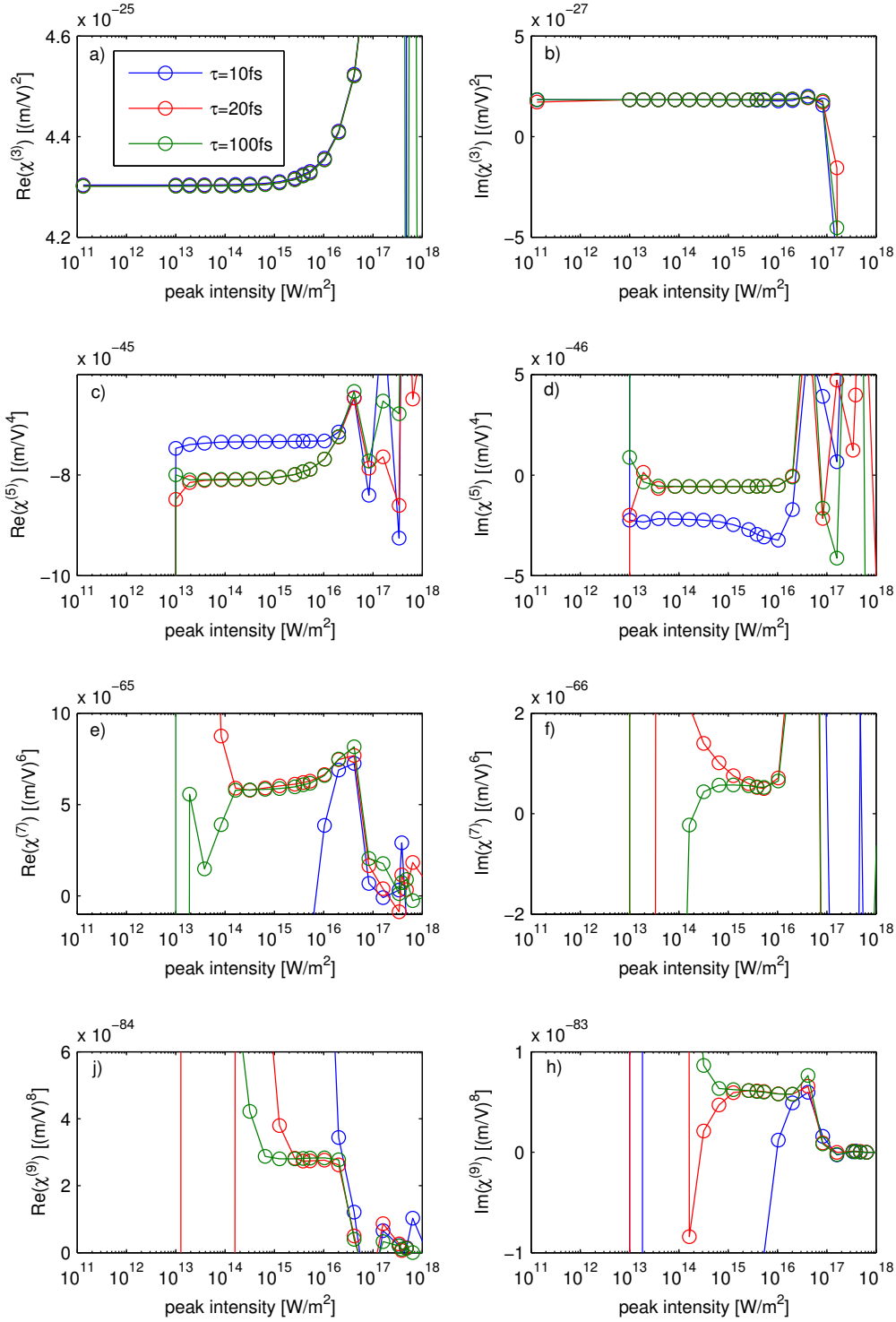


**Figure 5.4.:** Nonlinear responses  $\chi^{(3)}$ ,  $\chi^{(5)}$ ,  $\chi^{(7)}$  and  $\chi^{(9)}$  for different pulse durations plotted against peak intensity. The left/right column depicts real/imaginary parts. The responses  $\chi^{(2j+1)}$  were extracted according to Equation (5.35) at their corresponding frequencies  $(2j+1)\omega_0$ . Circles stand for numerical data connected by lines to guide the eye.

For  $\chi^{(5)}$  results already vary, and we can only constrain its value to the interval

$$\text{Re}(\chi^{(5)}) = (-0.1 \dots - 2.5) 10^{-45} (m/V)^4. \quad (5.46)$$

Calculating even higher order Kerr responses gives results, which strongly depend on the chosen intensities to evaluate the r.h.s. of Equations (5.40). One can speculate that this inconsistency reveals the Taylor expansion of the nonlinear polarization to be invalid.

Additionally, comparing the two values for  $\chi^{(3)}$  and  $\chi^{(5)}$  at  $\omega_0$  from Equations (5.45) and (5.46) with the values given in Equations (5.42) and (5.43) ( $\chi^{(3)}$  at  $3\omega_0$  and  $\chi^{(5)}$  at  $5\omega_0$ ) reveals that the  $\chi$ 's are dispersive, at least over frequency scales of some  $\omega_0$ .

Finally, we extract the ionization cross section  $\sigma_K$ , which appears in the charge Equation (5.13). Thereby,  $\sigma_K$  is determined such that the charge at the end of the laser pulse coincides with the remaining charge in the simulation. Results are shown in Figure 5.5, where  $\sigma_K$  is plotted versus the peak intensity. We observe agreement for all pulse durations  $\tau$ . The initially strong dependency of  $\sigma_K$  on the peak intensity weakens for intensities  $I > 20 \text{ TW/cm}^2$ . In particular, in the intensity range of  $20 \text{ TW/cm}^2 < I < 40 \text{ TW/cm}^2$  where the interesting physics of  $\hat{n}_{\text{NL}}(\omega_0)$  changing its sign happens,  $\sigma_K$  varies by a factor of 10. Since charge contributions were identified to play a crucial role, we want to model the charge generation as good as possible in that intensity interval. Therefore, we extract the value

$$\sigma_K = 2.7 \times 10^{-172} (m/V)^9 \text{ 1/s} \quad (5.47)$$

at an intermediate peak intensity of  $I = 32 \text{ TW/cm}^2$ .

#### 5.5.4. Comparison to phenomenological models for polarization

We are provided with the knowledge of the 'true' nonlinear polarization (and refractive index) for various intensities at central frequency  $\omega_0$  from the simulations and additionally with the values of the higher order nonlinear responses  $\chi^{(2j+1)}$  and the ionization cross section  $\sigma_K$ . Thus we are able to compare simulation results to the usually applied models, which we shortly recall:

1. **Kerr model:**  $P_{\text{NL}}(t) = \varepsilon_0 \chi^{(3)} E(t)^3$  models 3rd order Kerr effect and should be valid in the low intensity regime.
2. **HOKE model:**  $P_{\text{NL}}(t) = \varepsilon_0 \chi^{(3)} E(t)^3 + \chi^{(5)} E(t)^5$ . The next higher order Kerr coefficient  $\chi^{(5)}$  is included. As we learned before, accounting for even higher order coefficients makes no sense.
3. **Standard Model:**  $P_{\text{NL}}(t) = \varepsilon_0 \chi^{(3)} E(t)^3 - \frac{q_e^2}{m_e} FT^{-1} \left\{ \frac{FT\{\rho(t)E(t)\}}{\omega^2} \right\}$  accounts with the Kerr term for the low intensity part from bound electrons and deals with continuum contributions by inclusion of the charge term.

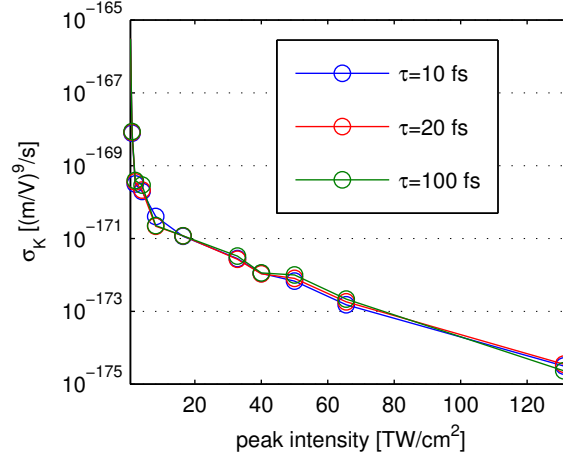


**Figure 5.5.:** Ionization cross section  $\sigma_K$  versus peak intensity for pulse durations  $\tau = 10$  fs,  $\tau = 20$  fs and  $\tau = 100$  fs.  $\sigma_K$  was determined such that the charge according to Equation (5.13) matches the one obtained from quantum mechanical simulations. Charge contributions play a crucial role in the intensity interval  $20 \text{ TW/cm}^2 < I < 40 \text{ TW/cm}^2$ , where the change of sign of  $\hat{n}_{\text{NL}}(\omega_0)$  occurs.

With these models we try to reproduce the nonlinear polarization and refractive index. We therefore choose for the parameters  $\chi^{(3)}$  and  $\chi^{(5)}$  their values at  $\omega_0$  from Equations (5.45) and (5.46) and for the value of the ionization cross section  $\sigma_K$  its value from Equation (5.47):

$$\chi^{(3)} = (2.3 \times 10^{-25} + i3.3 \times 10^{-28}) \text{ (m/V)}^2 \quad (5.48)$$

$$\chi^{(5)} = (-2.5 \times 10^{-45}) \text{ (m/V)}^4 \quad (5.49)$$

$$\sigma_K = 2.7 \times 10^{-172} \text{ (m/V)}^9 \text{ 1/s.} \quad (5.50)$$

Using these values, we can compute the nonlinear polarization and refractive index according to the used models for any intensity. The comparison to simulation results in Fourier domain at  $\omega_0$  is shown in Figures 5.6 - 5.8.

In Figures 5.6 - 5.8 the left column shows the nonlinear polarization  $\hat{P}_{\text{NL}}(\omega_0)$  and the right column the nonlinear refractive index  $\hat{n}_{\text{NL}}(\omega_0)$ .

The first row demonstrates very good agreement between the simulated nonlinear polarization (Figures 5.6 - 5.8 a), black curves, absolute value) and the one calculated (red curve) from the Kerr model  $P_{\text{NL}}(t) = \varepsilon_0 \chi^{(3)} E(t)^3$  in the low intensity regime. Figures 5.6 - 5.8 b) reveal the same for the real part of  $\hat{n}_{\text{NL}}(\omega_0)$ . Thus, in the low intensity regime up to  $I \sim 10 \text{ TW/cm}^2$ , the nonlinearity is excellently described by a third order Kerr term.

The rows 2 and 3 show the nonlinearities in the interesting intensity regime. To avoid confusion, we used blue/green curves for the real/imaginary part of a variable and solid/dashed lines for model/simulation curves. Then the quantum mechanical

simulation result is in dashed lines the same in row 2 and 3.

In Figures 5.6 - 5.8 c), d) comparison of simulation results to the HOKE model  $P_{\text{NL}}(t) = \varepsilon_0 \chi^{(3)} E(t)^3 + \varepsilon_0 \chi^{(5)} E(t)^5$  is shown. We see the real part of  $\hat{n}_{\text{NL}}(\omega_0)$  saturates and changes sign, but at much lower intensity  $I \approx 16 \text{ TW/cm}^2$  as compared to simulation results. Thus this model is not suited to reproduce the saturation and change of sign of  $\hat{n}_{\text{NL}}(\omega_0)$  at the correct intensity values. Of course, for  $\chi^{(5)}$  we employed the largest (absolute value) of its possible values (see Equation (5.46)). This renders the negative nonlinearity the strongest and thus leads to the lowest intensity values for saturation and sign change. However, also for the smallest (absolute value) of  $\chi^{(5)}$ , which leads the largest intensity value for the change of sign, the slope of the HOKE model  $P_{\text{NL}}(t)$  w.r.t. the peak-intensity is too flat to model the steep slope from simulations in the important intensity regime around  $32 \text{ TW/cm}^2$ . Furthermore, as it will get clear later, the HOKE model can not account for the delayed response of the charge contributions, since the HOKE model is instantaneous.

Comparison to the Standard model with the nonlinearity  $P(t) = \varepsilon_0 \chi^{(3)} E(t)^3 - \frac{q_e^2}{m_e} FT^{-1} \left\{ \frac{FT\{\rho(t)E(t)\}}{\omega^2} \right\}$  is shown in Figures 5.6 - 5.8 e), f). We observe good agreement between model and simulation for the intensity values at which the real part of  $\hat{n}_{\text{NL}}(\omega_0)$  saturates and changes sign. That is, this model, although being rather simple, is very well suited for describing the nonlinear response to an external field.

Additionally, we want to compare simulation results to results from the Standard model in time domain. To do so, we choose an interesting intensity of  $I = 32 \text{ TW/cm}^2$ , where bound as well as charge contributions play a role. The results are presented in Figures 5.9, 5.10 and 5.11 for the pulse durations of  $\tau = 10 \text{ fs}$ ,  $\tau = 20 \text{ fs}$  and  $\tau = 100 \text{ fs}$ , respectively.

For readability of the plots, both model and simulation polarizations have been filtered in Fourier domain around  $\omega_0$ . That is, only contributions from the frequency interval  $[0.8 \cdot \omega_0, 1.2 \cdot \omega_0]$  around  $\omega_0$  were kept.

Let us consider Figures 5.9, 5.10 and 5.11. In the upper left plot a), contributions to the nonlinear polarization from charge only  $P_{\text{NL}}^{\text{CC}}(t)$  (from simulations, red line) are compared to the Standard model contributions accounting for charge  $P_{\text{NL},\rho} = -\frac{q_e^2}{m_e} FT^{-1} \left\{ \frac{FT\{\rho(t)E(t)\}}{\omega^2} \right\}$  (blue line) and good agreement is obvious. We stress the fact, that a common  $\sigma_K$  for all pulse durations  $\tau$  was used.

In the upper right plot b), contributions to the nonlinear polarization from bound electrons only ( $P_{\text{NL}}^{\text{BB}}(t)$  from simulations, red line) are compared to the bound electron contributions from the Standard model  $P_{\text{NL},\chi^{(3)}}(t) = \varepsilon_0 \chi^{(3)} E(t)^3$  (blue line). The polarization according to the Standard model gives slightly different amplitude. Note, that in the Standard model we used the parameter  $\chi^{(3)}$  which was obtained from the total nonlinear polarization, that is accounting for all contributions (bound-bound, continuum-continuum, bound-continuum). Contrary, the simulation results plotted display  $P_{\text{NL}}^{\text{BB}}(t)$  (bound-bound contributions) only, so small deviations are not surprising. We emphasize that using one fixed value for  $\chi^{(3)}$  yields excellent agreement for all pulse durations  $\tau$ . Interestingly, at times shortly before  $t = 500 \text{ a.u.}$  ( $\tau = 10 \text{ fs}$ ,

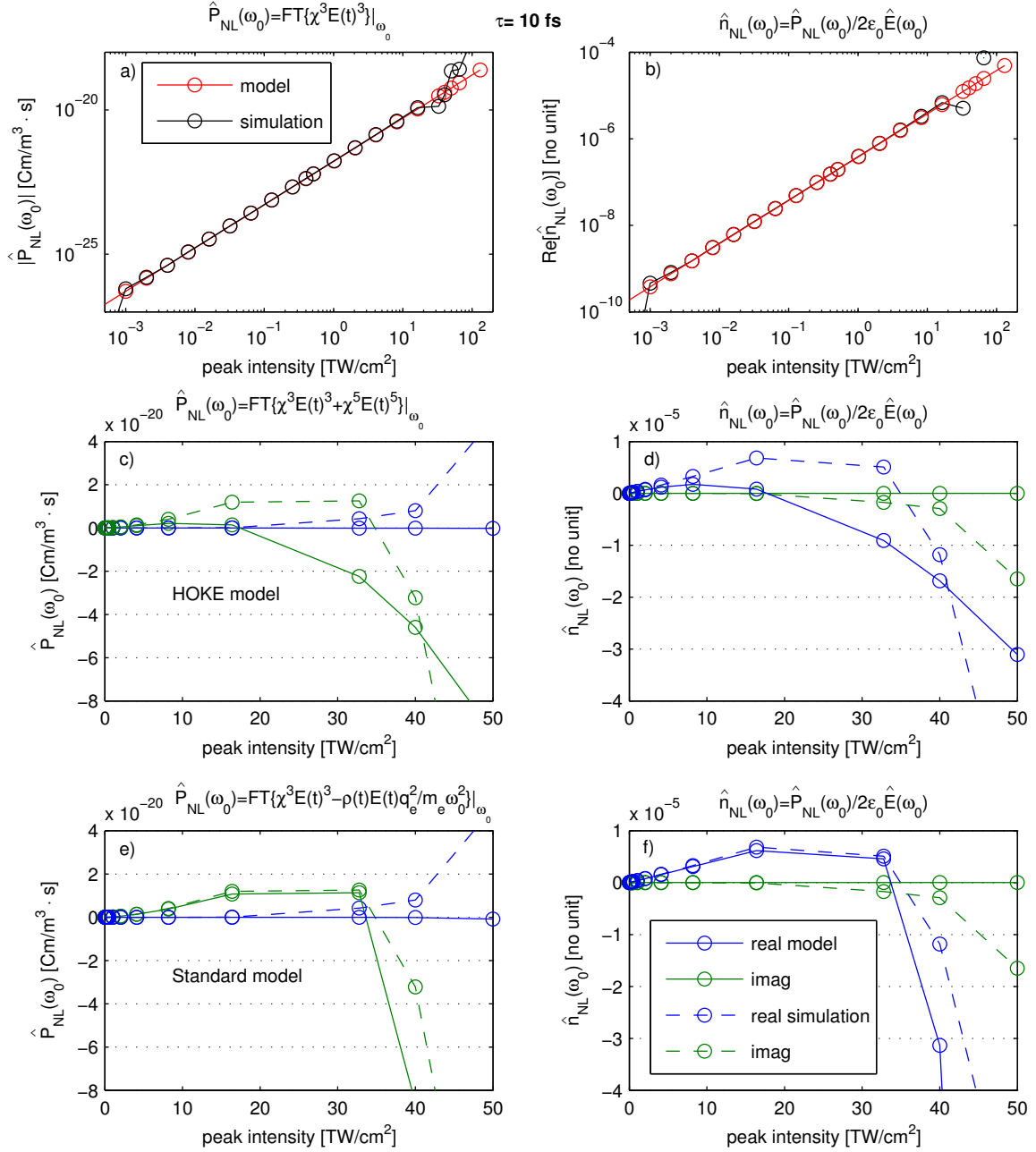


**Figure 5.6.:** Comparison of quantum mechanical simulations with nonlinear polarization models at  $\omega_0$  in Fourier domain for  $\tau = 10$  fs: a), b) compares nonlinear polarization and refractive index from simulations (red line) with predictions from the Kerr model (black line) and reveals agreement in the intensity regime  $I < 10$  TW/cm<sup>2</sup>. Comparison of simulation results (blue/green dashed lines for real/imaginary part) to predictions from the c), d) HOKE and e), f) Standard model (blue/green solid lines for real/imaginary part) reveals the Standard model to be more appropriate.

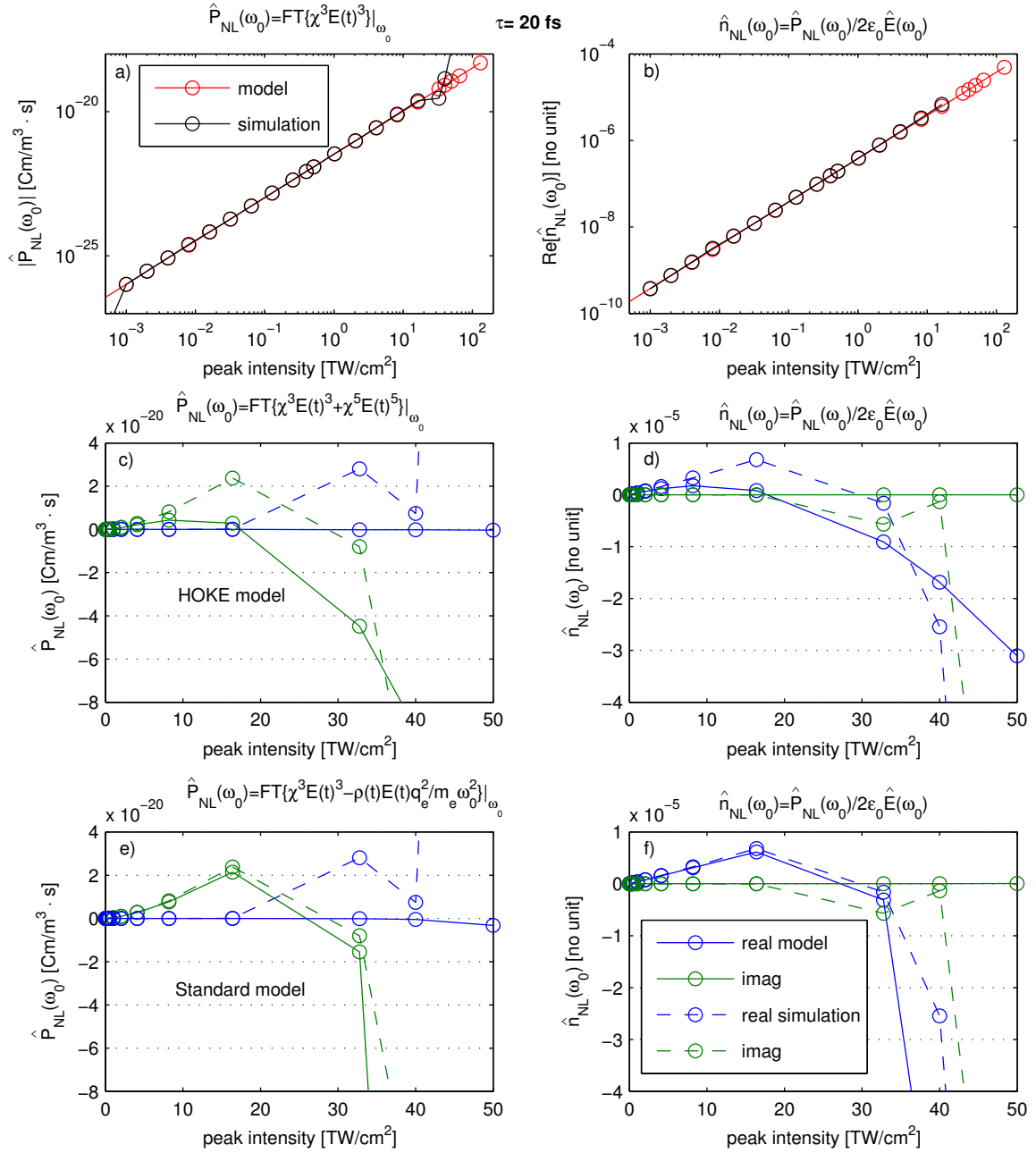


**Figure 5.7.:** Comparison of quantum mechanical simulations with nonlinear polarization models at  $\omega_0$  in Fourier domain for  $\tau = 20$  fs: a), b) compares nonlinear polarization and refractive index from simulations (red line) with predictions from the Kerr model (black line) and reveals agreement in the intensity regime  $I < 10$  TW/cm<sup>2</sup>. Comparison of simulation results (blue/green dashed lines for real/imaginary part) to predictions from the c), d) HOKE and e), f) Standard model (blue/green solid lines for real/imaginary part) reveals the Standard model to be more appropriate.

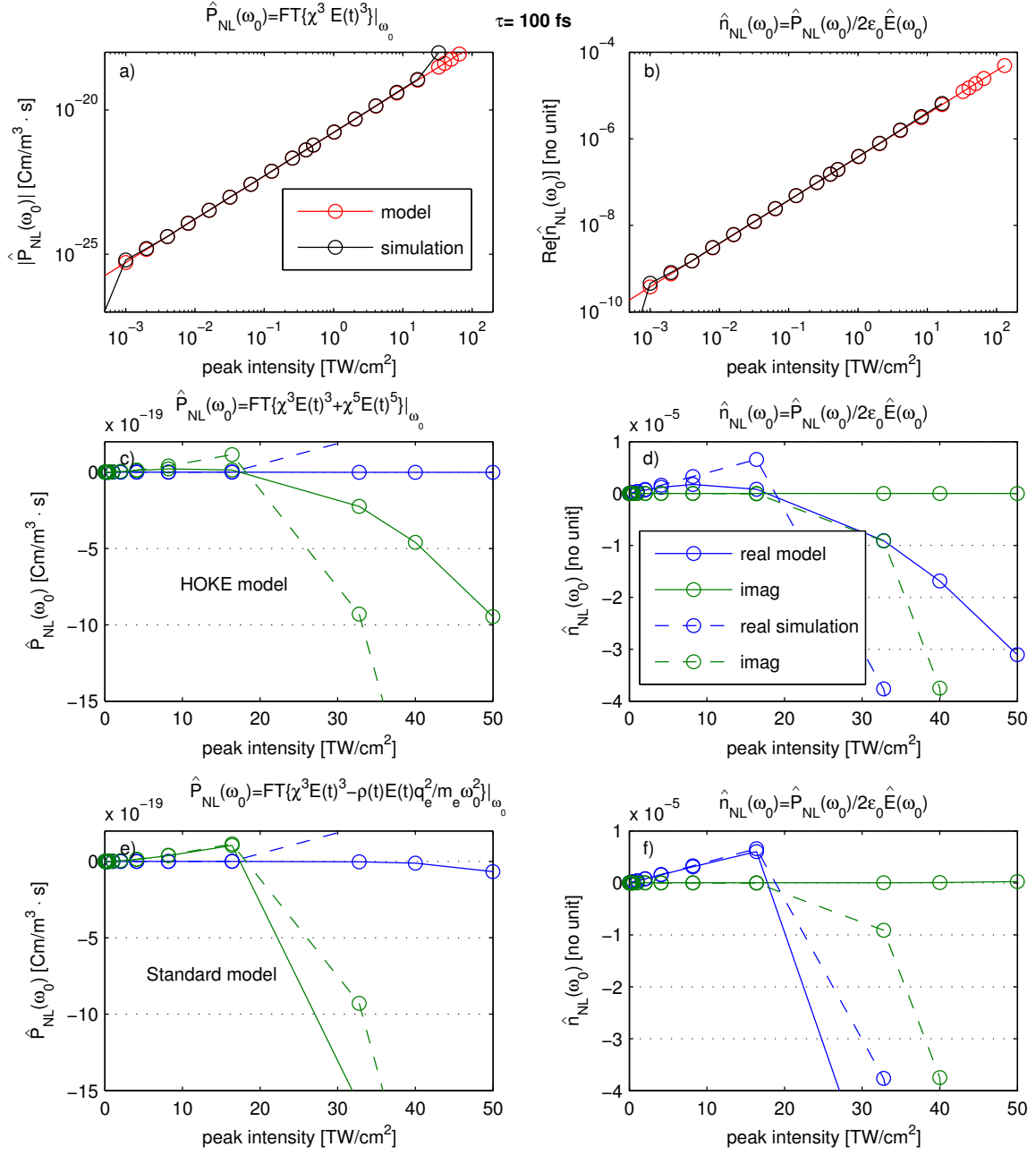


**Figure 5.8.:** Comparison of quantum mechanical simulations with nonlinear polarization models at  $\omega_0$  in Fourier domain for  $\tau = 100$  fs: a), b) compares nonlinear polarization and refractive index from simulations (red line) with predictions from the Kerr model (black line) and reveals agreement in the intensity regime  $I < 10$  TW/cm<sup>2</sup>. Comparison of simulation results ((blue/green dashed lines for real/imaginary part) to predictions from the c), d) HOKE and e), f) Standard model (blue/green solid lines for real/imaginary part) reveals the Standard model to be more appropriate.

Figure 5.9) and  $t = 800$  a.u. ( $\tau = 20$  fs, Figure 5.10) a small contribution with opposite sign (or delay) occurs in the simulation curve. This indicates that the response of the bound electrons also has some small delayed, that is non-instantaneous part.

The lower left plot c) shows the total nonlinear polarization from simulations (red) compared to the full Standard model  $P_{\text{NL}}(t) = P_{\text{NL},\chi^{(3)}}(t) + P_{\text{NL},\rho}(t)$  (blue). The nonlinear polarization at laser frequency  $\omega_0$  is excellently modeled by  $P_{\text{NL}}(t)$  from the Standard model. In particular the different temporal character of bound and ionized contributions gets obvious. The bound part of the polarization instantaneously occurs with the driving field (centered around time  $t = 0$ ), whereas the charge contribution to the polarization occurs retarded. Additionally, the different sign of the polarization of bound and ionized contributions (compare, e.g. Figure 5.2 c) and g)) is confirmed.

Finally, the lower right plot d) presents the charge evolution in simulations (red) and in the Standard model according to Equation (5.13) (blue). The ionized fraction after the pulse agrees. Of course, we used the simulations to fit  $\sigma_K$  with that condition, but note that the same  $\sigma_K$  applies for  $\tau = 10$  fs,  $\tau = 20$  fs and  $\tau = 100$  fs (see Figures 5.9 - 5.11 d)). However, the Standard model does not describe the considerable amount of charge that is temporarily generated. Nevertheless, this temporary charge seems negligible, when considering nonlinear polarization at  $\omega_0$ .

As a last point, let's consider limitations of the simulations and the models.

In Figure 5.11 results for pulse duration  $\tau = 100$  fs at peak intensity  $I = 32$  TW/cm<sup>2</sup> are shown. In that situation, the plasma contributions to the nonlinear polarization prevail (compare a) with b)). The slight oscillations of the envelope of the simulation curves are unphysical and due to absorption at the boundary of the numerical box. The implementation of a larger box is in progress and will remove this artifact.

The reverse situation is encountered in Figure 5.12, where the case for a  $\tau = 100$  fs pulse with  $I = 16$  TW/cm<sup>2</sup> peak intensity is shown. Now, polarization from bound electrons dominates (compare subplot a) with b)). Here, the Standard model significantly underestimates polarization from the ionized electrons as can be seen in a). However, since these are of minor influence, the overall nonlinear polarization shown in c) is modeled satisfactorily.

Finally, we want to illustrate the failure of the HOKE model to describe nonlinear polarization in the intensity regime, where bound as well as ionized contributions play a role. We assume the HOKE model for the nonlinear polarization as  $P_{\text{NL}}(t) = \varepsilon_0 [\chi^{(3)}E(t)^3 + \chi^{(5)}E(t)^5 + \chi^{(7)}E(t)^7 + \chi^{(9)}E(t)^9]$ . In contrast to the considerations before, the instantaneous coefficients  $\chi^{(2j+1)}$  are not tried to be extracted from simulation results. This time, we chose the  $\chi^{(2j+1)}$  such, that the HOKE  $\hat{P}_{\text{NL}}(\omega_0)$  matches the  $\hat{P}_{\text{NL}}(\omega_0)$  from simulations in the interesting intensity regime, where saturation and change of sign occurs. Exemplary applying this procedure to simulation results with pulse duration  $\tau = 20$  fs leads to the situation presented in Figure 5.13 a). We obtain agreement between quantum mechanical simulations (dashed line) and the HOKE model (solid line) for the values of the nonlinear polarization at  $\omega_0$ . In Figure 5.13 b) however, plotting the around  $\omega_0$  filtered nonlinear polarization from



the simulation with peak intensity  $I = 32 \text{ TW/cm}^2$  (red line) and the respective one from the HOKE model (blue line) in time domain reveals the fundamental problem. The temporal character of instantaneous bound and retarded continuum contributions in the quantum mechanical simulation can not be captured by a purely instantaneous HOKE model.

In summary, comparison of the subplots b) of Figures 5.9, 5.10 and 5.12 indicates, that the nonlinear polarization from bound electrons is well described by the respective Standard model term  $P_{\text{NL},\chi^{(3)}}(t) = \varepsilon_0 \chi^{(3)} E(t)^3$  with the values of  $\chi^{(3)}$  determined from our simulations. In situations, where the extracted  $\chi^{(3)}$  does not apply to correctly model bound contributions (see Figure 5.11 b) with the discussion about numerics), these are of minor influence. The nonlinear polarization from ionized electrons is correctly modeled with the Standard model term for continuum contributions  $P_{\text{NL},\rho}(t) = -\frac{q_e^2}{m_e} FT^{-1} \left\{ \frac{FT\{\rho(t)E(t)\}}{\omega^2} \right\}$  as is confirmed in Figures 5.9, 5.10 and 5.11 a). When this description is inadequate (see Figure 5.12 a)), continuum contributions are unimportant. Therefore, the Standard model is well suited for the description of nonlinear polarization originating from bound as well as from ionized electrons. Although already argued to be not applicable earlier, a further attempt to apply the HOKE model failed as illustrated in Figure 5.13.

## 5.6. Conclusion and outlook

We investigated the nonlinear polarization and the nonlinear refractive index of a gas under irradiation of a strong laser pulse. For simplicity, we restricted ourselves to consider the response of the single electron in the one dimensional hydrogen atom. Numerical solution of the underlying Schrödinger equation allowed us to observe saturation and a change of sign of the nonlinear refractive index for increasing peak intensity of the laser. Additionally, rigorous distinction between bound and ionized parts of the wave function revealed the free charge to be responsible for this saturation. On top, we compared our findings to usually employed models for the polarization. These involve a perturbative expansion in terms of the laser field. Our analysis proved that the instantaneous, intensity independent higher order susceptibilities occurring in such an expansion can not be defined reasonably. On the other hand, the simple Standard model for the polarization, accounting for the optical Kerr response and for plasma generation is sufficiently able to reproduce quantum mechanically calculated behavior.

Conclusively, for the here considered one dimensional hydrogen atom, a demanding quantum mechanical calculation for the polarization is inferior to the simple Standard model in terms of application. But without the quantum mechanical simulations, the underlying mechanisms remain hidden.

To further advance our understanding, we plan to investigate not only hydrogen, but also other noble gases such as argon or xenon. There the difficulty appears, that these gases are no longer single electron systems and quantum mechanical modeling

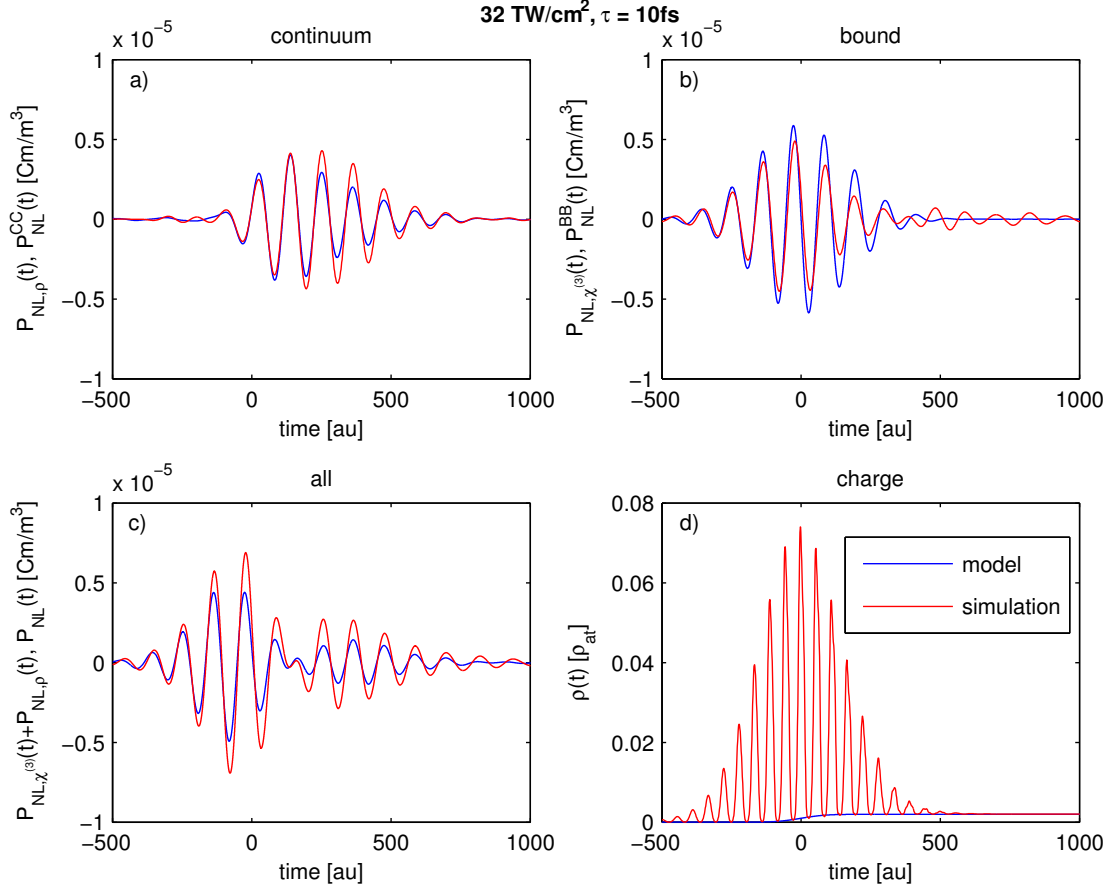


**Figure 5.9.:** Comparison of quantum mechanical simulations (red lines) with the Standard model (blue lines) in time domain for  $\tau = 10$  fs and  $I = 32$  TW/cm<sup>2</sup>. a) compares charge contributions  $P_{NL}^{CC}(t)$  from simulations (red line) with the Standard model  $P_{NL,\rho}(t) = -\frac{q_e^2}{m_e} FT^{-1} \left\{ \frac{FT\{\rho(t)E(t)\}}{\omega^2} \right\}$  (blue line). b) depicts bound contributions  $P_{NL}^{BB}(t)$  from simulation (red line) and  $P_{NL,\chi}^{(3)}(t) = \varepsilon_0 \chi^{(3)} E(t)^3$  from the Standard model (blue line). c) shows total nonlinear polarization  $P_{NL}(t)$  from simulations (red line) and total nonlinear polarization  $P_{NL,\chi}^{(3)}(t) + P_{NL,\rho}(t)$  from the Standard model (blue line). d) presents the charge evolution for simulations (red line) and for the Standard model according to Equation (5.13) (blue line). Results in a)-c) are filtered around  $\omega_0$  in Fourier domain.

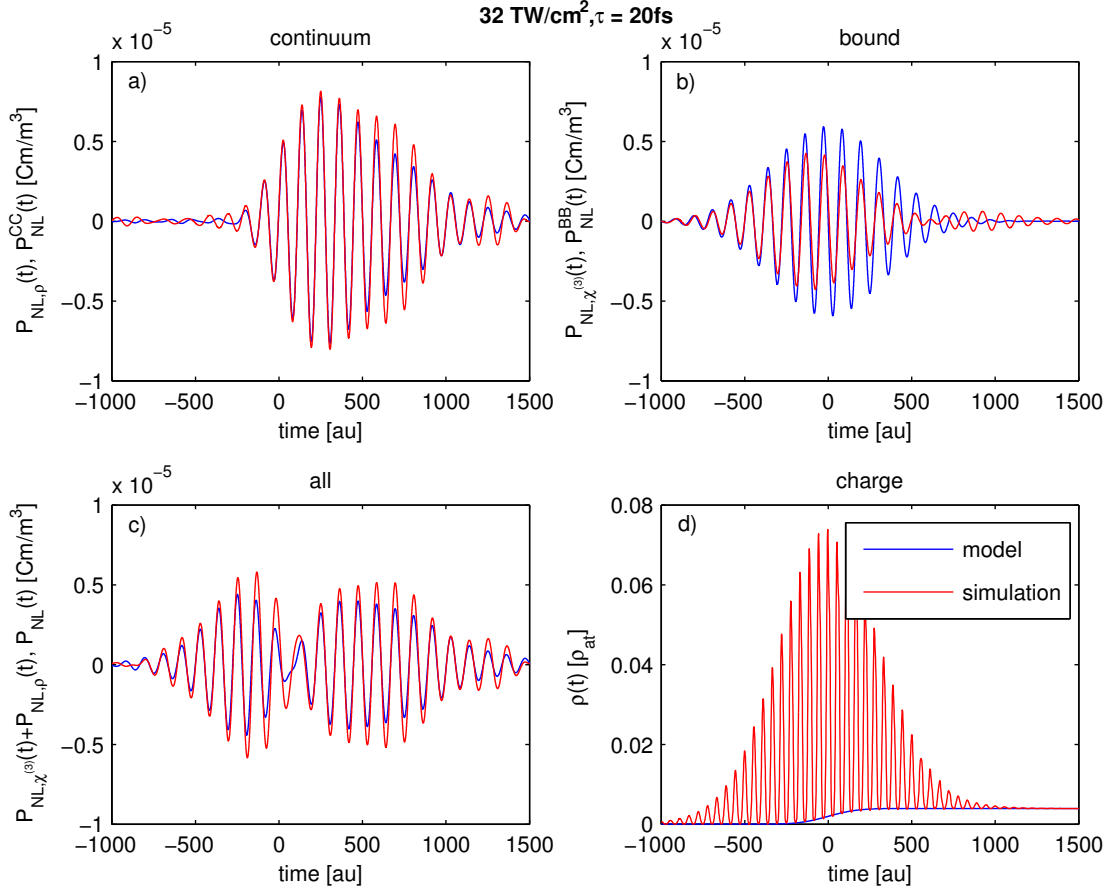


**Figure 5.10.:** Comparison of quantum mechanical simulations (red lines) with the Standard model (blue lines) in time domain for  $\tau = 20$  fs and  $I = 32$  TW/cm<sup>2</sup>. a) compares charge contributions  $P_{\text{NL},\rho}^{\text{CC}}(t)$  from simulations (red line) with the Standard model  $P_{\text{NL},\rho}(t) = -\frac{q_e^2}{m_e} FT^{-1} \left\{ \frac{FT\{\rho(t)E(t)\}}{\omega^2} \right\}$  (blue line). b) depicts bound contributions  $P_{\text{NL}}^{\text{BB}}(t)$  from simulation (red line) and  $P_{\text{NL},\chi^{(3)}}(t) = \varepsilon_0 \chi^{(3)} E(t)^3$  from the Standard model (blue line). c) shows total nonlinear polarization  $P_{\text{NL}}(t)$  from simulations (red line) and total nonlinear polarization  $P_{\text{NL},\chi^{(3)}}(t) + P_{\text{NL},\rho}(t)$  from the Standard model (blue line). d) presents the charge evolution for simulations (red line) and for the Standard model according to Equation (5.13) (blue line). Results in a)-c) are filtered around  $\omega_0$  in Fourier domain.

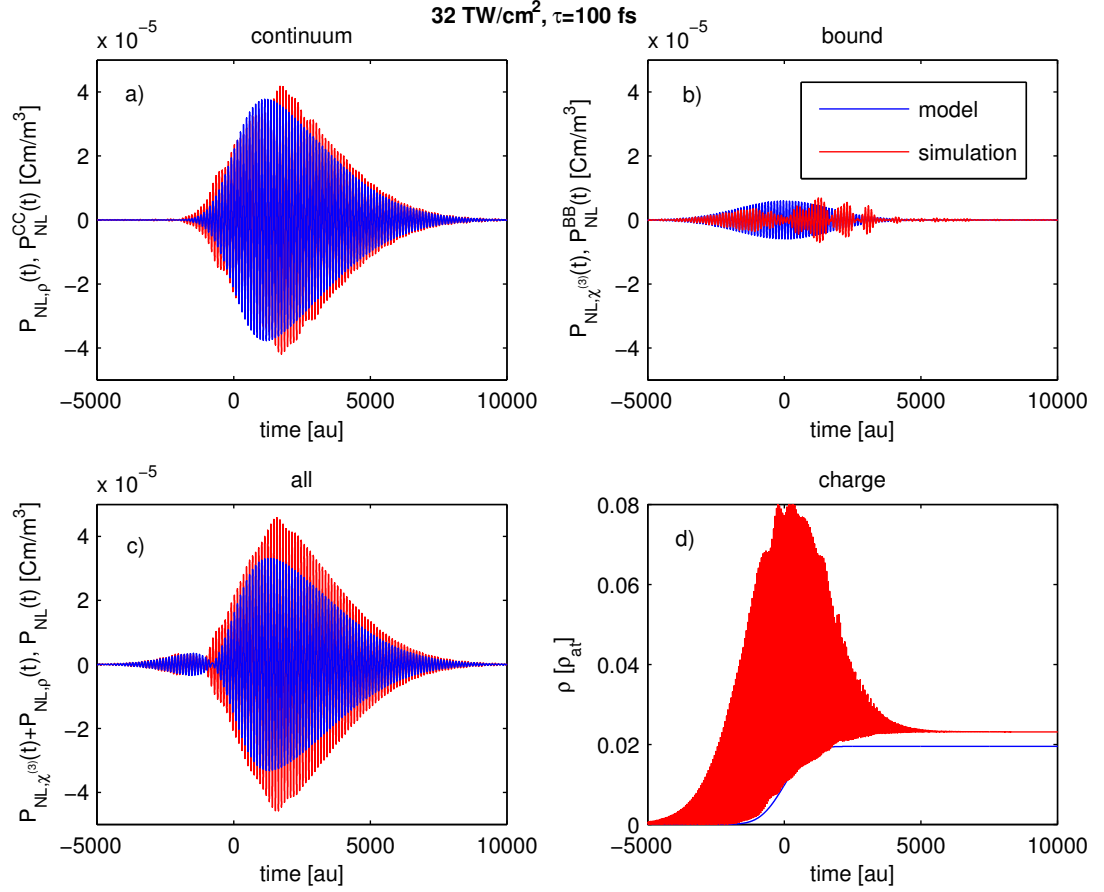


**Figure 5.11.:** Comparison of quantum mechanical simulations (red lines) with the Standard model (blue lines) in time domain for  $\tau = 100$  fs and  $I = 32$  TW/cm<sup>2</sup>. a) compares charge contributions  $P_{\text{NL},\rho}^{\text{CC}}(t)$  from simulations (red line) with the Standard model  $P_{\text{NL},\rho}(t) = -\frac{q_e^2}{m_e} FT^{-1} \left\{ \frac{FT\{\rho(t)E(t)\}}{\omega^2} \right\}$  (blue line). b) depicts bound contributions  $P_{\text{NL}}^{\text{BB}}(t)$  from simulation (red line) and  $P_{\text{NL},\chi^{(3)}}(t) = \epsilon_0 \chi^{(3)} E(t)^3$  from the Standard model (blue line). c) shows total nonlinear polarization  $P_{\text{NL}}(t)$  from simulations (red line) and total nonlinear polarization  $P_{\text{NL},\chi^{(3)}}(t) + P_{\text{NL},\rho}(t)$  from the Standard model (blue line). d) presents the charge evolution for simulations (red line) and for the Standard model according to Equation (5.13) (blue line). Results in a)-c) are filtered around  $\omega_0$  in Fourier domain.

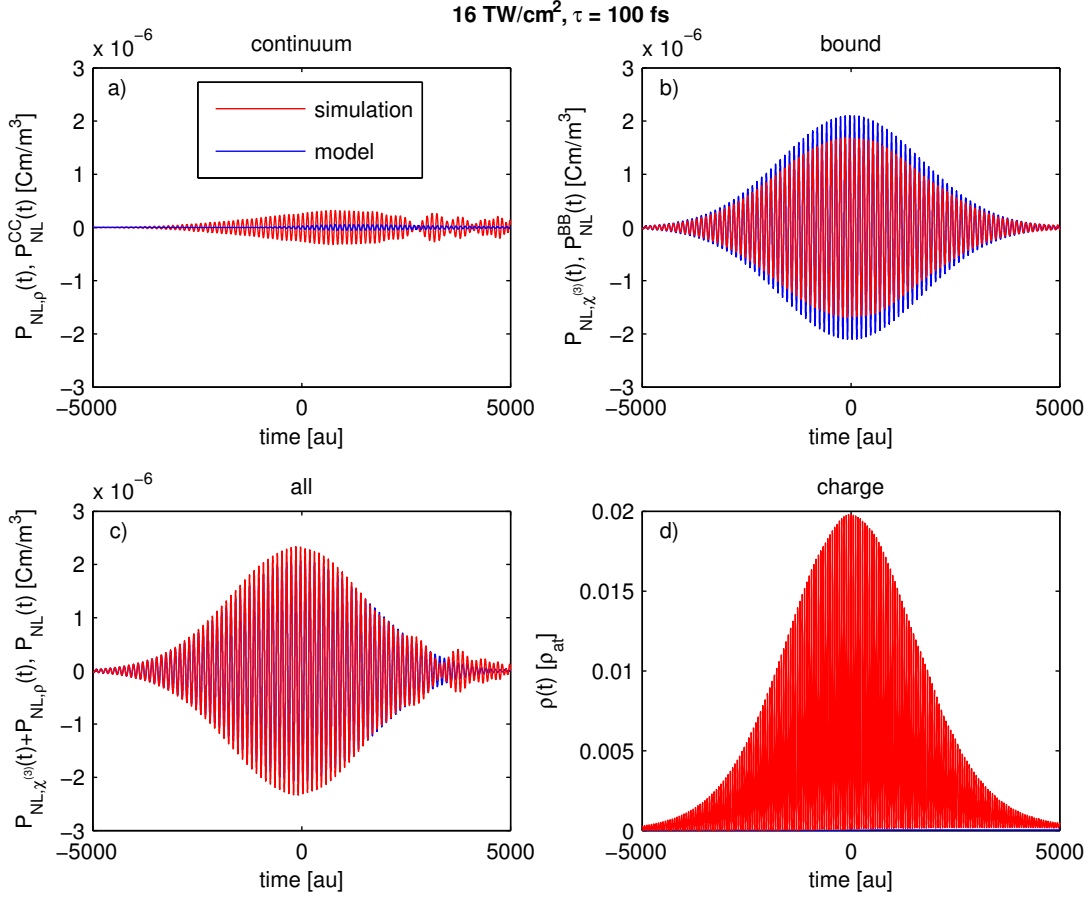


**Figure 5.12.:** Comparison of quantum mechanical simulations (red lines) with the Standard model (blue lines) in time domain for  $\tau = 100$  fs and  $I = 16$  TW/cm<sup>2</sup>. a) compares charge contributions  $P_{\text{NL},\rho}^{\text{CC}}(t)$  from simulations (red line) with the Standard model  $P_{\text{NL},\rho}(t) = -\frac{q_e^2}{m_e} FT^{-1} \left\{ \frac{FT\{\rho(t)E(t)\}}{\omega^2} \right\}$  (blue line). b) depicts bound contributions  $P_{\text{NL}}^{\text{BB}}(t)$  from simulation (red line) and  $P_{\text{NL},\chi^{(3)}}(t) = \varepsilon_0 \chi^{(3)} E(t)^3$  from the Standard model (blue line). c) shows total nonlinear polarization  $P_{\text{NL}}(t)$  from simulations (red line) and total nonlinear polarization  $P_{\text{NL},\chi^{(3)}}(t) + P_{\text{NL},\rho}(t)$  from the Standard model (blue line). d) presents the charge evolution for simulations (red line) and for the Standard model according to Equation (5.13) (blue line). Results in a)-c) are filtered around  $\omega_0$  in Fourier domain.

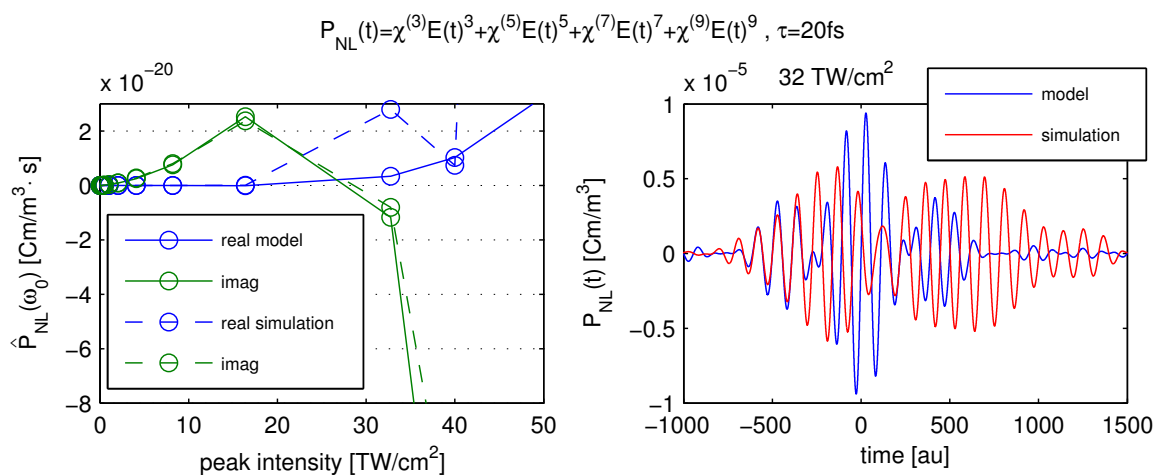


**Figure 5.13.:** Comparison between quantum mechanical simulations and the HOKE model for  $\tau = 20$  fs and  $I = 32$  TW/cm<sup>2</sup>. a) In Fourier domain, simulation results (blue/green dashed lines for real/imaginary part) can be matched for all peak intensities by a HOKE model  $\hat{P}_{\text{NL}}(\omega_0) = \varepsilon_0 FT [\chi^{(3)}E(t)^3 + \chi^{(5)}E(t)^5 + \chi^{(7)}E(t)^7 + \chi^{(9)}E(t)^9]$  (blue/green solid lines for real/imaginary part) by choosing  $\chi^{(3)} = 2.3 \times 10^{-25} + i3.3 \times 10^{-28}$  (m/V)<sup>2</sup>,  $\chi^{(5)} = -2.5 \times 10^{-45}$  (m/V)<sup>4</sup>,  $\chi^{(7)} = 4.5 \times 10^{-65} + i5.7 \times 10^{-67}$  (m/V)<sup>6</sup>,  $\chi^{(9)} = -2.35 \times 10^{-85} - i5.2 \times 10^{-87}$  (m/V)<sup>8</sup>, where the coefficients  $\chi^{(2j+1)}$  are not derived from the simulation result. In time domain in b) the instantaneous nature of the HOKE model (blue line) does not reproduce the temporal character of the simulation (red line). For readability, simulation and HOKE model results were filtered around  $\omega_0$ . Remember, we used an envelope phase of  $\phi = \pi/2$  for the electric field, thus the nonlinear polarization in Fourier domain occurs rotated by  $\phi = \pi/2$  in the complex plain.

becomes very demanding and expensive in numerical effort. Handling these atoms in the single active electron approximation will be a way out.

Additionally, we restricted our analysis to one dimension. Implementing our calculations for fully 3D simulations is in progress and should bring the numerical values closer to the physical reality. Also comparing to the 1D results will decide whether full 3D simulations are necessary or if 1D results give a reasonably good description.

Finally, a combination of the quantum mechanical calculation of the medium response with the laser propagation Equation (2.31) will result in an ultimate tool for modeling laser-matter interaction in the high intensity regime. To match the numerical requirements and to combine our calculations with an existing parallel code for laser propagation, we intend to outsource the quantum mechanical simulations to GPGPU hardware.





## 6. Summary and Outlook

We dealt with the generation and characterization of new ultra-short light sources by using high-intensity laser-matter interactions to engineer the light. We approached the description of laser-matter interaction from the optical side in the two major parts Chapter 3 and Chapter 4 and switched to atomic physics considerations in Chapter 5.

The first setup we investigated in the optical part analyzed the generation of THz radiation as it is emitted when focusing an ionizing two-color laser pulse into a gas. We demonstrated that a frequency conversion process as well as the radiating plasma current are able to emit THz radiation. We proved that the THz emission from the plasma current exceeds by orders of magnitude the one from the frequency conversion process in the high intensity regime and thus performed a detailed analysis of the plasma current mechanism. In the local spectrum approximation, we revealed the THz spectra to result from interference in Fourier domain of many contributing spectra. The single spectra correspond to radiation that is emitted during a short period of time around the well separated moments of ionization, where the charge density increases stepwise. The understanding of that interference mechanism allowed us to explain the THz spectra we observed for varying parameters of the input pulse. We advanced by considering extended plasma sources, where we already included linear propagation of the input pulse and found a first hint of the propagation direction of the input pulse to be the main direction of THz emission. We refined the description and modeled linear and nonlinear propagation of the input pulse and emitted THz radiation by directly solving Maxwell's equation via the finite-differences time-domain (FDTD) method. The results showed, that a description of forward propagating fields is sufficient, which allowed us to accurately model THz generation with significant less numerical effort by means of the unidirectional pulse propagation equation (UPPE). A final comparison of results from the UPPE were excellently confirmed by experimental results. Further advancement can be achieved by going beyond considering linearly polarized light only. Since vectorial effects start to play a role, emission of THz radiation is expected not to be only in forward direction. Then the description with UPPE renders inappropriate and modeling field propagation with FDTD becomes mandatory. This gives rise to challenging numerical modeling, but new possibilities for engineering and optimizing THz radiation arise. To capture new effects, the underlying analytical model has to be improved, which leaves room for future analysis.

The second optical part dealt with self-compression of laser pulses in gas. We transformed the usually in fibers applied solitary compression scheme, where self-phase modulation broadens the spectrum and linear dispersion ensures the mandatory flat phase into bulk gas. In order to inhibit spatial pulse collapse due to a positive Kerr

coefficient, we exploited an exotic setup with negative Kerr coefficient on the cost of the underlying third order nonlinearity to be highly dispersive. Such a dispersive Kerr coefficient questioned the compression scheme, which is based on a constant coefficient. In a purely temporal analysis, we demonstrated that the solitary compression survives this obstacle by identifying temporal shifts of high intensity zones of the pulse to later times to be the only additional effect. These shifts can already be captured by the first order term of an Taylor expansion of the dispersive nonlinearity and do not qualitatively change, when including the remaining terms from the expansion. We provided a scheme to estimate suited pulse parameters for self-compression and demonstrated our findings to be applicable in the bulk setup. Furthermore, we revealed the possibility of pulse compression for a vanishing Kerr coefficient, where the dispersion of the nonlinearity itself mediates the compression. It works perfectly in the purely temporal configuration, but leads to partial pulse collapse in the bulk setup. Further prospects lie in the more accurate description of the medium nonlinearities. The here employed nonlinearity is well reasoned, but still approximate and the for an experimental realization important, precise numbers might not coincide with the here obtained ones. Additionally, we could speculate on possibly existing properties of the medium response which are not captured by the approximated model for the nonlinearity, but can be exploited for designing an improved compression scheme.

The third major part elucidated the atomic physics side of laser matter interaction by studying the nonlinear polarization and the closely related nonlinear refractive index of a gas under irradiation of a high intensity laser pulse. For simplicity we considered the one dimensional hydrogen atom in linearly polarized light. Despite this crude simplification, we were able to extract basic physical features by numerically solving the time dependent Schrödinger equation. We observed a linear rising, subsequent saturation and final change of sign of the nonlinear refractive index for increasing intensity. Furthermore, the strict distinction between bound and ionized contributions revealed that the saturation and change of sign occurs at intensities at which charge generation sets in and that this charge is responsible for the saturating behavior of the refractive index. In order to connect our results to phenomenological models for the nonlinear polarization and refractive index, we extracted the model parameters from our quantum mechanical results. The phenomenological model expand the response of bound electrons in a Taylor series in terms of the applied field and are controversial about how to handle the ionized contributions. We were able to show, that an accountancy for the ionized contribution of the response by high orders of the Taylor expansion is impossible, due to the different temporal character of instantaneous bound and delayed continuum responses. In contrast, the simple standard model, including a third order term for bound contributions and a intensity dependent ionization rate is well suited for the description of the nonlinear polarization and refractive index over a large intensity range. It seems that the quantum mechanical description is a way to heavy tool when compared to the simple standard model, but justifies its utilization by revealing the underlying mechanism for saturation of the refractive index. We will advance beyond hydrogen gas by investigating, e.g., argon and

---

xenon. These are many electron systems, which renders the numerical description demanding, but currently ongoing work tries to capture the essential physics by treating the atoms in the single active electron approximation. Moreover, the investigations will be extended to three dimensions and the quantitative results are expected to be closer to the physical reality.

All together, extending an existing computer code for the propagation of laser light by a precise description of the medium response with the time dependent Schrödinger equation will result in an ultimate tool for modeling laser-matter interaction in the high intensity regime. To meet the numerical requirements, a massive parallelization along with taking advantage of the capacities of graphical processors is mandatory.



# A. Finite-Differences Time-Domain Scheme

The finite-differences time-domain (FDTD) method [83,84] is the straight forward way to numerically solve the time dependent Maxwell equations

$$\nabla \times \mathbf{E} = -\partial_t \mathbf{B} \quad (\text{A.1})$$

$$\nabla \times \mathbf{H} = \mathbf{J} + \partial_t \mathbf{D}. \quad (\text{A.2})$$

For a nonmagnetic medium the fields are connected via the material equations

$$\mathbf{D} = \varepsilon \mathbf{E} \quad (\text{A.3})$$

$$\mathbf{B} = \mu_0 \mathbf{H}. \quad (\text{A.4})$$

For the moment, we assume given  $\varepsilon = \varepsilon(\mathbf{r}, t)$  and  $\mathbf{J} = \mathbf{J}(\mathbf{r}, t)$ . Choosing Cartesian coordinates and denoting our fields as  $\mathbf{F} = (F_x, F_y, F_z)^T$ , Equations (A.1), (A.2) are equivalent to the system of scalar equations

$$\frac{\partial E_z}{\partial y} - \frac{\partial E_y}{\partial z} = -\frac{\partial B_x}{\partial t}, \quad (\text{A.5})$$

$$\frac{\partial E_x}{\partial z} - \frac{\partial E_z}{\partial x} = -\frac{\partial B_y}{\partial t}, \quad (\text{A.6})$$

$$\frac{\partial E_y}{\partial x} - \frac{\partial E_x}{\partial y} = -\frac{\partial B_z}{\partial t}, \quad (\text{A.7})$$

$$\frac{\partial H_z}{\partial y} - \frac{\partial H_y}{\partial z} = J_x + \frac{\partial D_x}{\partial t}, \quad (\text{A.8})$$

$$\frac{\partial H_x}{\partial z} - \frac{\partial H_z}{\partial x} = J_y + \frac{\partial D_y}{\partial t}, \quad (\text{A.9})$$

$$\frac{\partial H_y}{\partial x} - \frac{\partial H_x}{\partial y} = J_z + \frac{\partial D_z}{\partial t}. \quad (\text{A.10})$$

### A. Finite-Differences Time-Domain Scheme

---

We introduce an evenly spaced grid along the spatial and temporal axis

$$x_i = x_0 + i\Delta x \quad (\text{A.11})$$

$$y_j = x_0 + j\Delta y \quad (\text{A.12})$$

$$z_k = x_0 + k\Delta z \quad (\text{A.13})$$

$$t_n = x_0 + n\Delta t. \quad (\text{A.14})$$

We represent our functions  $F(x, y, z, t)$  by their values on the grid  $F(x_i, y_j, z_k, t_n)$  and use the abbreviation

$$F(x_i, y_j, z_k, t_n) = F|_{i,j,k}^n. \quad (\text{A.15})$$

Then a finite difference version of Equation (A.5) is

$$\frac{B_x|_{i,j+1/2,k+1/2}^{n+1/2} - B_x|_{i,j+1/2,k+1/2}^{n-1/2}}{\Delta t} = \frac{E_y|_{i,j+1/2,k+1}^n - E_y|_{i,j+1/2,k}^n}{\Delta z} \quad (\text{A.16})$$

$$- \frac{E_z|_{i,j+1,k+1/2}^n - E_z|_{i,j,k+1/2}^n}{\Delta y} \quad (\text{A.17})$$

and analogous for Equations (A.6), (A.7). For Equation (A.8) we get

$$\frac{D_x|_{i+1/2,j,k}^n - D_x|_{i+1/2,j,k}^{n-1}}{\Delta t} = \frac{H_z|_{i+1/2,j+1/2,k}^{n-1/2} - H_z|_{i+1/2,j-1/2,k}^n}{\Delta y} \quad (\text{A.18})$$

$$- \frac{H_y|_{i+1/2,j,k+1/2}^{n-1/2} - H_y|_{i+1/2,j,k-1/2}^{n-1/2}}{\Delta z} \quad (\text{A.19})$$

$$+ J_x|_{i+1/2,j,k}^{n-1/2} \quad (\text{A.20})$$

and analogous for Equations (A.9), (A.10). The relative shifts of the grid points for the involved field components originate from assuring a centered time and space differencing scheme for all scalar Equations (A.5)-(A.10). These schemes are numerically stable [105], if the Courant-condition

$$\frac{\sqrt{(\Delta x)^2 + (\Delta y)^2 + (\Delta z)^2}}{\Delta t} > c, \quad (\text{A.21})$$

is fulfilled. Here,  $c$  is the speed of light, the maximum velocity information at which travels in our equations.

## B. Crank Nicholson Scheme

We want to numerically solve

$$i \frac{\partial}{\partial t} \psi(x, t) = \left[ -\frac{\partial^2}{\partial x^2} - iA(t)\partial_x + V(x) \right] \psi(x, t) \quad (\text{B.1})$$

with the initial condition

$$\psi(x, t = 0) = \psi_0(x). \quad (\text{B.2})$$

We introduce an evenly spaced grid in space and time

$$x_n = x_0 + n\Delta x \quad (\text{B.3})$$

$$t_j = t_0 + j\Delta t. \quad (\text{B.4})$$

Any function of  $x$  and  $t$  is represented by its values at the grid points. In the following we use the abbreviations:

$$\psi(x_n, t_j) = \psi_n^j \quad (\text{B.5})$$

$$A(t_j) = A^j \quad (\text{B.6})$$

$$V(x_n) = V_n. \quad (\text{B.7})$$

For the discretization of Equations (B.1) a 'Crank-Nicholson' scheme

$$i \frac{\psi_n^{j+1} - \psi_n^j}{\Delta t} = -\frac{1}{2} \left[ \frac{1}{2} \left( \frac{\psi_{n+1}^{j+1} - 2\psi_n^{j+1} + \psi_{n-1}^{j+1}}{\Delta x^2} + \frac{\psi_{n+1}^j - 2\psi_n^j + \psi_{n-1}^j}{\Delta x^2} \right) \right] \quad (\text{B.8})$$

$$- i \frac{1}{2} \left( A^{j+1} \frac{\psi_{n+1}^{j+1} - \psi_{n-1}^{j+1}}{2\Delta x} + A^j \frac{\psi_{n+1}^j - \psi_{n-1}^j}{2\Delta x} \right) \quad (\text{B.9})$$

$$+ \frac{1}{2} V_n (\psi_n^{j+1} + \psi_n^j) \quad (\text{B.10})$$

is used. Introducing

$$\alpha = \frac{\Delta t}{4\Delta x^2} \quad (\text{B.11})$$

and regrouping terms according to their according time-slice  $j$  gives

$$\begin{aligned} & \left( \alpha + \frac{i\Delta t}{2\Delta x} A^{j+1} \right) \psi_{n+1}^{j+1} + \left( i - 2\alpha + \frac{\Delta t}{2} V_n \right) \psi_n^{j+1} + \left( \alpha - \frac{i\Delta t}{2\Delta x} A^{j+1} \right) \psi_{n-1}^{j+1} = \\ & \left( -\alpha - \frac{i\Delta t}{2\Delta x} A^j \right) \psi_{n+1}^j + \left( i + 2\alpha + \frac{\Delta t}{2} V_n \right) \psi_n^j + \left( -\alpha + \frac{i\Delta t}{2\Delta x} A^j \right) \psi_{n-1}^j. \end{aligned} \quad (\text{B.12})$$

The iteration of time-slice  $j$  to  $j+1$  is equivalent to the solution of the following linear system of equations

$$\begin{pmatrix} b_0 & c_0 & 0 & \cdots \\ a_1 & b_1 & c_1 & \cdots \\ & & \cdots & \\ & & \cdots & a_{N-2} & b_{N-2} & c_{N-2} \\ & & \cdots & 0 & a_{N-1} & b_{N-1} \end{pmatrix} \cdot \begin{pmatrix} \psi_0^{j+1} \\ \psi_1^{j+1} \\ \cdots \\ \psi_{N-1}^{j+1} \end{pmatrix} = \begin{pmatrix} r_0 \\ r_1 \\ \cdots \\ r_{N-1} \end{pmatrix} \quad (\text{B.13})$$

with the tridiagonal coefficient-matrix determined by

$$a_k = \left( \alpha - \frac{i\Delta t}{2\Delta x} A^{j+1} \right) \quad (\text{B.14})$$

$$b_k = \left( i - 2\alpha + \frac{\Delta t}{2} V_k \right) \quad (\text{B.15})$$

$$c_k = \left( \alpha + \frac{i\Delta t}{2\Delta x} A^{j+1} \right) \quad (\text{B.16})$$

and the resulting vector elements

$$r_k = \left( -\alpha - \frac{i\Delta t}{2\Delta x} A^j \right) \psi_{k+1}^j + \left( i + 2\alpha + \frac{\Delta t}{2} V_k \right) \psi_k^j + \left( -\alpha + \frac{i\Delta t}{2\Delta x} A^j \right) \psi_{k-1}^j. \quad (\text{B.17})$$

Together with the initial condition Equation (B.2) we are then able to calculate the wave function  $\psi(x, t)$  for all times  $t$ .

That scheme is accurate up to second order in space and time, but numerically slightly unstable. The outcome of the simulations were not affected by this instability, as was checked by a stable version, where the term Equation (B.9) was replaced by

$$-i \frac{1}{2} \left( \frac{A^{j+1} + A^j}{2} \right) \left( \frac{\psi_{n+1}^{j+1} - \psi_{n-1}^{j+1}}{2\Delta x} + \frac{\psi_{n+1}^j - \psi_{n-1}^j}{2\Delta x} \right). \quad (\text{B.18})$$

However, the accuracy of such a scheme is then only approximate of second order in time.



# C. Definition of the optical intensity

## C.1. Continuous wave

Consider an electric field

$$E(t) = a_0 \cos(\omega_0 t + \phi) \quad (\text{C.1})$$

$$= \frac{a_0}{2} (\exp(i(\omega_0 t + \phi)) + \exp(-i(\omega_0 t + \phi))) \quad (\text{C.2})$$

The intensity  $I$  is defined as temporal average ( $\langle \dots \rangle_t$ ) of the absolute value of the pointing vector, which is given for a TEM wave as  $S = \varepsilon_0 c_0 |E(t)|^2$ . Then

$$I = \langle S \rangle_t = \varepsilon_0 c_0 \langle |E(t)|^2 \rangle_t \quad (\text{C.3})$$

$$= \varepsilon_0 c_0 \frac{a_0^2}{4} \langle \exp(i2(\omega_0 t + \phi)) + 2 + \exp(-i2(\omega_0 t + \phi)) \rangle_t \quad (\text{C.4})$$

$$= \varepsilon_0 c_0 \frac{a_0^2}{2} + \varepsilon_0 c_0 \underbrace{\left\langle \frac{a_0^2}{2} \cos(2(\omega_0 t + \phi)) \right\rangle_t}_{=0 \quad t \dots t+T} \quad (\text{C.5})$$

$$= \varepsilon_0 c_0 \frac{a_0^2}{2}. \quad (\text{C.6})$$

## C.2. Pulse

Consider an electric field

$$E(t) = a_0 \cos(\omega_0 t + \phi) e^{-\frac{t^2}{\tau^2}} \quad (\text{C.7})$$

$$= \frac{a_0}{2} \left( \exp(i(\omega_0 t + \phi)) e^{-\frac{t^2}{\tau^2}} + \exp(-i(\omega_0 t + \phi)) e^{-\frac{t^2}{\tau^2}} \right). \quad (\text{C.8})$$

The intensity  $I$  is defined as temporal average ( $\langle \dots \rangle_t$ ) of the absolute value of the pointing vector, which is given for a TEM wave as  $S = \varepsilon_0 c_0 |E(t)|^2$ . For the laser

### C. Definition of the optical intensity

---

pulse we have

$$I = \langle S \rangle_t = \varepsilon_0 c_0 \langle |E(t)|^2 \rangle_t \quad (\text{C.9})$$

$$= \varepsilon_0 c_0 \frac{a_0^2}{4} \left\langle e^{-\frac{2t^2}{\tau^2}} (\exp(i2(\omega_0 t + \phi)) + 2 + \exp(-i2(\omega_0 t + \phi))) \right\rangle_t \quad (\text{C.10})$$

$$I(t) = \varepsilon_0 c_0 \frac{a_0^2}{2} e^{-\frac{2t^2}{\tau^2}}, \quad (\text{C.11})$$

which is the envelope intensity, provided the period  $T$  and pulse duration fulfill  $T \ll \tau$ .

# D. Fourier Transformation

## D.1. Continuous wave

Assume a continuous wave laser as given in Equation (C.2). Its Fourier transform is

$$E(\omega) = \int dt e^{-i\omega t} \frac{a_0}{2} (\exp(i(\omega_0 t + \phi)) + \exp(-i(\omega_0 t + \phi))) \quad (\text{D.1})$$

$$= \frac{a_0}{2} (\delta(\omega - \omega_0) + \delta(\omega + \omega_0)). \quad (\text{D.2})$$

## D.2. Pulse

Assume a laser pulse as given in Equation (C.8). Its Fourier transform is

$$E(\omega) = \int dt e^{-i\omega t} \frac{a_0}{2} (e^{i(\omega_0 t + \phi)} + e^{-i(\omega_0 t + \phi)}) e^{-\frac{t^2}{\tau^2}} \quad (\text{D.3})$$

$$= \int dt \frac{a_0}{2} e^{-\frac{t^2}{\tau^2} - i(\omega - \omega_0)t} e^{i\phi} + \frac{a_0}{2} e^{-\frac{t^2}{\tau^2} - i(\omega + \omega_0)t} e^{-i\phi} \quad (\text{D.4})$$

$$= \int dt \frac{a_0}{2} e^{-\left(\frac{t}{\tau} + \frac{i(\omega - \omega_0)\tau}{2}\right)^2} e^{-\left(\frac{(\omega - \omega_0)\tau}{2}\right)^2} e^{i\phi} + \text{same}(+\omega_0, -\phi). \quad (\text{D.5})$$

Introducing  $t' = \left(\frac{t}{\tau} + \frac{i(\omega - \omega_0)\tau}{2}\right)$  with  $dt'/dt = 1/\tau$ , we get

$$E(\omega) = \underbrace{\int dt' e^{-t'^2}}_{=\sqrt{\pi}} \tau \frac{a_0}{2} e^{-\left(\frac{(\omega - \omega_0)\tau}{2}\right)^2} e^{i\phi} + \text{same}(+\omega_0, -\phi) \quad (\text{D.6})$$

$$= \tau \sqrt{\pi} \frac{a_0}{2} \left( e^{-\left(\frac{(\omega - \omega_0)\tau}{2}\right)^2} e^{i\phi} + e^{-\left(\frac{(\omega + \omega_0)\tau}{2}\right)^2} e^{-i\phi} \right). \quad (\text{D.7})$$



## E. Nonlinear polarization

We assume

$$P(t) = P^{(1)}(t) + P^{(3)}(t) + P^{(5)}(t) + \dots \quad (\text{E.1})$$

$$= \sum_{j=0} P^{(2j+1)}(t), \quad (\text{E.2})$$

where

$$P^{(2j+1)}(t) = \varepsilon_0 \chi^{(2j+1)} E(t)^{2j+1} \quad (\text{E.3})$$

with the  $\chi^{(2j+1)}$  to be not frequency dependent (instantaneous). Lets consider the polarization in Fourier domain:

$$P^{(2j+1)}(\omega) = \int dt P^{(2j+1)}(t) e^{-i\omega t} \quad (\text{E.4})$$

$$= \varepsilon_0 \chi^{(2j+1)} \int dt e^{-i\omega t} E(t)^{2j+1} \quad (\text{E.5})$$

$$= \varepsilon_0 \chi^{(2j+1)} \int dt e^{-i\omega t} \int \dots \int \frac{d\omega_1}{2\pi} \dots \frac{d\omega_{2j+1}}{2\pi} \times \quad (\text{E.6})$$

$$E(\omega_1) \dots E(\omega_{2j+1}) e^{i\omega_1 t} \dots e^{i\omega_{2j+1} t} \quad (\text{E.7})$$

$$= \varepsilon_0 \chi^{(2j+1)} \int \dots \int \frac{d\omega_1}{2\pi} \dots \frac{d\omega_{2j+1}}{2\pi} \delta(\omega - \omega_1 - \dots - \omega_{2j+1}) \times \quad (\text{E.8})$$

$$E(\omega_1) \dots E(\omega_{2j+1}) \quad (\text{E.9})$$

### E.1. Contributions at $\omega_0$

Inserting Equation (D.7) in Equation (E.9) and evaluating at  $\omega_0$  yields

$$P^{(2j+1)}(\omega_0) = \varepsilon_0 \chi^{(2j+1)} \int \dots \int \frac{d\omega_1}{2\pi} \dots \frac{d\omega_{2j+1}}{2\pi} \delta(\omega_0 - \omega_1 - \dots - \omega_{2j+1}) \times \quad (\text{E.10})$$

$$\frac{a_0}{2} \sqrt{\pi} \tau \left( e^{-\left(\frac{\omega_1 - \omega_0}{2/\tau}\right)^2} e^{i\phi} + e^{-\left(\frac{\omega_1 + \omega_0}{2/\tau}\right)^2} e^{-i\phi} \right) \quad (\text{E.11})$$

$$\dots \quad (\text{E.12})$$

$$\frac{a_0}{2} \sqrt{\pi} \tau \left( e^{-\left(\frac{\omega_{2j+1} - \omega_0}{2/\tau}\right)^2} e^{i\phi} + e^{-\left(\frac{\omega_{2j+1} + \omega_0}{2/\tau}\right)^2} e^{-i\phi} \right). \quad (\text{E.13})$$

## E. Nonlinear polarization

---

In order to evaluate the  $\delta$  integral, we have to choose  $j + 1$  of our  $2j + 1$  frequencies  $\omega_i \approx +\omega_0$  and  $j$  to be  $\omega_i \approx -\omega_0$ , since only for these frequencies the electric field  $\hat{E}(\omega)$  has significant contributions. There are  $\binom{2j+1}{j}$  ways to do so. Then, only the exponential with the argument close to zero contributes  $\omega_i \pm \omega_0 \approx 0$ . Without loss of generality we write

$$P^{(2j+1)}(\omega_0) = \varepsilon_0 \chi^{(2j+1)} \int \dots \int \frac{d\omega_1}{2\pi} \dots \frac{d\omega_{2j+1}}{2\pi} \delta(\omega_0 - \omega_1 - \dots - \omega_{2j+1}) \binom{2j+1}{j} \times$$

$$\frac{a_0}{2} \sqrt{\pi\tau} \left( e^{-\left(\frac{\omega_1 - \omega_0}{2/\tau}\right)^2} e^{i\phi} \right) \quad (\text{E.14})$$

$$\dots \quad (\text{E.15})$$

$$\frac{a_0}{2} \sqrt{\pi\tau} \left( e^{-\left(\frac{\omega_{j+1} - \omega_0}{2/\tau}\right)^2} e^{i\phi} \right) \quad (\text{E.16})$$

$$\frac{a_0}{2} \sqrt{\pi\tau} \left( e^{-\left(\frac{\omega_{j+2} + \omega_0}{2/\tau}\right)^2} e^{-i\phi} \right) \quad (\text{E.17})$$

$$\dots \quad (\text{E.18})$$

$$\frac{a_0}{2} \sqrt{\pi\tau} \left( e^{-\left(\frac{\omega_{2j+1} + \omega_0}{2/\tau}\right)^2} e^{-i\phi} \right). \quad (\text{E.19})$$

We introduce

$$\nu_i = \omega_i - \omega_0 \quad \text{for } i = 1 \dots j + 1 \quad (\text{E.20})$$

$$\nu_i = \omega_i + \omega_0 \quad \text{for } i = j + 2 \dots 2j + 1 \quad (\text{E.21})$$

and get

$$P^{(2j+1)}(\omega_0) = \varepsilon_0 \chi^{(2j+1)} \int \dots \int \frac{d\nu_1}{2\pi} \dots \frac{d\nu_{2j+1}}{2\pi} \delta(\nu_1 + \dots + \nu_{2j+1}) \times \quad (\text{E.22})$$

$$\binom{2j+1}{j} \left(\frac{a_0}{2}\right)^{2j+1} \sqrt{\pi}^{2j+1} \tau^{2j+1} e^{i\phi} e^{-\left(\frac{\nu_1}{2/\tau}\right)^2} \dots e^{-\left(\frac{\nu_{2j+1}}{2/\tau}\right)^2} \quad (\text{E.23})$$

$$= \varepsilon_0 \chi^{(2j+1)} \binom{2j+1}{j} \left(\frac{a_0}{2}\right)^{2j+1} \sqrt{\pi}^{2j+1} \tau^{2j+1} e^{i\phi} \times \quad (\text{E.24})$$

$$\int \dots \int \frac{d\nu_1}{2\pi} \dots \frac{d\nu_{2j}}{2\pi} \frac{2\pi}{2\pi} e^{-\left(\frac{\nu_1}{2/\tau}\right)^2} \dots e^{-\left(\frac{\nu_{2j}}{2/\tau}\right)^2} e^{-\left(\frac{\sum_i^{2j} \nu_i}{2/\tau}\right)^2} \quad (\text{E.25})$$

$$= \varepsilon_0 \chi^{(2j+1)} \binom{2j+1}{j} \left(\frac{a_0}{2}\right)^{2j+1} \sqrt{\pi}^{2j+1} \tau^{2j+1} e^{i\phi} \times \quad (\text{E.26})$$

$$\left(\frac{1}{2\pi}\right)^{2j} \frac{1}{2j+1} \pi^j (2/\tau)^{2j} \sqrt{2j+1} \quad (\text{E.27})$$

$$= \varepsilon_0 \chi^{(2j+1)} \sqrt{\pi} \tau e^{i\phi} \binom{2j+1}{j} \left(\frac{a_0}{2}\right)^{2j+1} \frac{1}{\sqrt{2j+1}}. \quad (\text{E.28})$$

## E.2. Contributions at $(2j + 1)\omega_0$

We now evaluate the polarization at different frequencies  $(2j + 1)\omega_0$ . Performing the same calculations as before, we get

$$P^{(2j+1)}((2j+1)\omega_0) = \varepsilon_0 \chi^{(2j+1)} \sqrt{\pi} \tau e^{i(2j+1)\phi} \left(\frac{a_0}{2}\right)^{2j+1} \frac{1}{\sqrt{2j+1}}. \quad (\text{E.29})$$





# Nomenclature

$\delta(x)$	delta distribution $\delta(x) = \infty \quad x = 0, \delta(x) = 0 \quad x \neq 0, \int \delta(x)dx = 1$
$\varepsilon_0$	vacuum susceptibility $\varepsilon_0 = 8.854 \times 10^{-12} \text{ As/Vm}$
$\lambda_0$	vacuum wavelength $\lambda_0 = 2\pi c/\omega_0$
$\mu_0$	vacuum permeability $\mu_0 = 4\pi \times 10^{-7} \text{ Vs/Am}$
$\nabla$	Nabla operator $\nabla = \partial_x \mathbf{e}_x + \partial_y \mathbf{e}_y + \partial_z \mathbf{e}_z$
$\nabla_{\perp}$	transverse Nabla operator $\nabla = \partial_x \mathbf{e}_x + \partial_y \mathbf{e}_y$
$\nu$	frequency $\nu = \omega/2\pi$
$\omega$	angular frequency
$\omega_0$	central frequency
$\partial_t$	partial differentiation with respect to $t$
$\mathbf{r}$	position vector $\mathbf{r} = x\mathbf{e}_x + y\mathbf{e}_y + z\mathbf{e}_z$
$\mathbf{e}_x$	unit vector in $x$ -direction
$c$	speed of light in vacuum $c = 2.99 \times 10^8 \text{ m/s}$
$k(\omega)$	Dispersion relation $k(\omega) = \omega n(\omega)/c$
$k_0$	wave number in material $k_0 = k(\omega_0) = \omega_0 n(\omega_0)/c$
$k_1$	reciprocal group velocity $k_1 = 1/v_g = \partial_{\omega} k(\omega) _{\omega_0}$
$k_2$	group velocity dispersion coefficient $k_2 = \partial_{\omega}^2 k(\omega) _{\omega_0}$
$L_d$	Dispersion length
$L_{NL}$	Nonlinear length
$n(\omega)$	linear refractive index
$n_2$	Kerr coefficient

## *Nomenclature*

---

$v_g$	group velocity
FDTD	Finite-Differences Time-Domain
FW/BW	Forward/Backward
FWHM	Full Width Half Maximum
GVD	Group Velocity Dispersion
HOKE	Higher Order Kerr Effect
MI	Modulational Instability
NLS	Nonlinear Schrödinger Equation
SPM	Self Phase Modulation
THz	Terahertz 1 THz = $10^{12}$ Hz
UPPE	Unidirectional Pulse Propagation Equation

# Bibliography

- [1] T. H. Maiman. Stimulated optical radiation in ruby. *Nature*, 187:493 – 494, 1960.
- [2] Masayoshi Tonouchi. Cutting-edge terahertz technology. *Nature Photonics*, 1(2):97 – 105, 2007.
- [3] Daniel Mittleman. *Sensing with Terahertz Radiation*. Springer Berlin Heidelberg, 2002.
- [4] Kiyomi Sakai. *Terahertz optoelectronics*. Topics in applied physics. Springer, 2005.
- [5] A. Giles Davies, Andrew D. Burnett, Wenhui Fan, Edmund H. Linfield, and John E. Cunningham. Terahertz spectroscopy of explosives and drugs. *Materials Today*, 11:18 – 26, 2008.
- [6] Kodo Kawase, Yuichi Ogawa, Yuuki Watanabe, and Hiroyuki Inoue. Non-destructive terahertz imaging of illicit drugs using spectral fingerprints. *Opt. Express*, 11(20):2549–2554, Oct 2003.
- [7] Ruth M Woodward, Bryan E Cole, Vincent P Wallace, Richard J Pye, Donald D Arnone, Edmund H Linfield, and Michael Pepper. Terahertz pulse imaging in reflection geometry of human skin cancer and skin tissue. *Physics in Medicine and Biology*, 47(21):3853, 2002.
- [8] Markus Walther, Bernd M. Fischer, and P. Uhd Jepsen. Noncovalent intermolecular forces in polycrystalline and amorphous saccharides in the far infrared. *Chemical Physics*, 288(2–3):261 – 268, 2003.
- [9] Jingle Liu, Jianming Dai, See Leang Chin, and ZhangX.-C. Broadband terahertz wave remote sensing using coherent manipulation of fluorescence from asymmetrically ionized gases. *Nature Photonics*, 4(9):627 – 631, 2010.
- [10] J.W. Waters, L. Froidevaux, R.S. Harwood, R.F. Jarnot, H.M. Pickett, W.G. Read, P.H. Siegel, R.E. Cofield, M.J. Filipiak, D.A. Flower, J.R. Holden, G.K. Lau, N.J. Livesey, G.L. Manney, H.C. Pumphrey, M.L. Santee, D.L. Wu, D.T. Cuddy, R.R. Lay, M.S. Loo, V.S. Perun, M.J. Schwartz, P.C. Stek, R.P. Thurstans, M.A. Boyles, K.M. Chandra, M.C. Chavez, Gun-Shing Chen, B.V. Chudasama, R. Dodge, R.A. Fuller, M.A. Girard, J.H. Jiang, Yibo Jiang, B.W.

- Knosp, R.C. LaBelle, J.C. Lam, K.A. Lee, D. Miller, J.E. Oswald, N.C. Patel, D.M. Pukala, O. Quintero, D.M. Scaff, W. Van Snyder, M.C. Tope, P.A. Wagner, and M.J. Walch. The earth observing system microwave limb sounder (eos mls) on the aura satellite. *Geoscience and Remote Sensing, IEEE Transactions on*, 44(5):1075 – 1092, may 2006.
- [11] Jerome Faist, Federico Capasso, Deborah L. Sivco, Carlo Sirtori, Albert L. Hutchinson, and Alfred Y. Cho. Quantum cascade laser. *Science*, 264(5158):553–556, 1994.
- [12] D. You, R. R. Jones, P. H. Bucksbaum, and D. R. Dykaar. Generation of high-power sub-single-cycle 500-fs electromagnetic pulses. *Opt. Lett.*, 18(4):290–292, Feb 1993.
- [13] D. H. Auston, K. P. Cheung, J. A. Valdmanis, and D. A. Kleinman. Cherenkov radiation from femtosecond optical pulses in electro-optic media. *Phys. Rev. Lett.*, 53:1555–1558, Oct 1984.
- [14] K.-L. Yeh, M. C. Hoffmann, J. Hebling, and Keith A. Nelson. Generation of 10  $\mu$ j ultrashort terahertz pulses by optical rectification. *Applied Physics Letters*, 90(17):171121, 2007.
- [15] Andrei G. Stepanov, Luigi Bonacina, Sergei V. Chekalin, and Jean-Pierre Wolf. Generation of 30  $\mu$ j single-cycle terahertz pulses at 100 hz repetition rate by optical rectification. *Opt. Lett.*, 33(21):2497–2499, Nov 2008.
- [16] Klaus Reimann. Table-top sources of ultrashort thz pulses. *Reports on Progress in Physics*, 70(10):1597, 2007.
- [17] C. D’Amico, A. Houard, M. Franco, B. Prade, A. Mysyrowicz, A. Couairon, and V. T. Tikhonchuk. Conical forward thz emission from femtosecond-laser-beam filamentation in air. *Phys. Rev. Lett.*, 98:235002, Jun 2007.
- [18] Joseph Peñano, Phillip Sprangle, Bahman Hafizi, Daniel Gordon, and Philip Serafim. Terahertz generation in plasmas using two-color laser pulses. *Phys. Rev. E*, 81:026407, Feb 2010.
- [19] V. B. Gildenburg and N. V. Vvedenskii. Optical-to-thz wave conversion via excitation of plasma oscillations in the tunneling-ionization process. *Phys. Rev. Lett.*, 98:245002, Jun 2007.
- [20] D. J. Cook and R. M. Hochstrasser. Intense terahertz pulses by four-wave rectification in air. *Opt. Lett.*, 25(16):1210–1212, Aug 2000.
- [21] Jianming Dai, Xu Xie, and X.-C. Zhang. Detection of broadband terahertz waves with a laser-induced plasma in gases. *Phys. Rev. Lett.*, 97:103903, Sep 2006.

- [22] Markus Kress, Torsten Löffler, Susanne Eden, Mark Thomson, and Hartmut G. Roskos. Terahertz-pulse generation by photoionization of air with laser pulses composed of both fundamental and second-harmonic waves. *Opt. Lett.*, 29(10):1120–1122, May 2004.
- [23] Xu Xie, Jianming Dai, and X.-C. Zhang. Coherent control of thz wave generation in ambient air. *Phys. Rev. Lett.*, 96:075005, Feb 2006.
- [24] Aurélien Houard, Yi Liu, Bernard Prade, and André Mysyrowicz. Polarization analysis of terahertz radiation generated by four-wave mixing in air. *Opt. Lett.*, 33(11):1195–1197, Jun 2008.
- [25] T. Bartel, P. Gaal, K. Reimann, M. Woerner, and T. Elsaesser. Generation of single-cycle thz transients with high electric-field amplitudes. *Opt. Lett.*, 30(20):2805–2807, Oct 2005.
- [26] I. Babushkin, W. Kuehn, C. Köhler, S. Skupin, L. Bergé, K. Reimann, M. Woerner, J. Herrmann, and T. Elsaesser. Ultrafast spatiotemporal dynamics of terahertz generation by ionizing two-color femtosecond pulses in gases. *Phys. Rev. Lett.*, 105:053903, Jul 2010.
- [27] H.G. Roskos, M.D. Thomson, M. Kieß, and T. Löffler. Broadband thz emission from gas plasmas induced by femtosecond optical pulses: From fundamentals to applications. *Laser & Photonics Reviews*, 1(4):349–368, 2007.
- [28] K. Y. Kim, A. J. Taylor, J. H. Glowina, and G. Rodriguez. Coherent control of terahertz supercontinuum generation in ultrafast laser-gas interactions. *Nat Photon*, 2:605–609, 2008.
- [29] Ki-Yong Kim, James H. Glowina, Antoinette J. Taylor, and George Rodriguez. Terahertz emission from ultrafast ionizing air in symmetry-broken laser fields. *Opt. Express*, 15(8):4577–4584, Apr 2007.
- [30] Ki-Yong Kim. Generation of coherent terahertz radiation in ultrafast laser-gas interactions. *Physics of Plasmas*, 16(5):056706, 2009.
- [31] Markus Kress, Torsten Löffler, Mark D. Thomson, Reinhard Dörner, Hartmut Gimpel, Karl Zrost, Thorsten Ergler, Robert Moshhammer, Uwe Morgner, Joachim Ullrich, and Hartmut G. Roskos. Determination of the carrier-envelope phase of few-cycle laser pulses with terahertz-emission spectroscopy. *Nat Phys*, 2:327 – 331, 05 2006.
- [32] Takao Fuji, Takuya Horio, and Toshinori Suzuki. Generation of 12 fs deep-ultraviolet pulses by four-wave mixing through filamentation in neon gas. *Opt. Lett.*, 32(17):2481–2483, 2007.

- [33] S. Ashihara, J. Nishina, T. Shimura, and K. Kuroda. Soliton compression of femtosecond pulses in quadratic media. *J. Opt. Soc. Am. B*, 19(10):2505–2510, 2002.
- [34] M. Bache, J. Moses, and F. W. Wise. Scaling laws for soliton pulse compression by cascaded quadratic nonlinearities. *J. Opt. Soc. Am. B*, 24(10):2752–2762, 2007.
- [35] Xiang Liu, Liejia Qian, and Frank Wise. High-energy pulse compression by use of negative phase shifts produced by the cascade  $\chi^{(2)}:\chi^{(2)}$  nonlinearity. *Opt. Lett.*, 24(23):1777–1779, 1999.
- [36] C. V. Shank, R. L. Fork, R. Yen, R. H. Stolen, and W. J. Tomlinson. Compression of femtosecond optical pulses. *Applied Physics Letters*, 40(9):761–763, 1982.
- [37] F. M. Mitschke and L. F. Mollenauer. Ultrashort pulses from the soliton laser. *Opt. Lett.*, 12(6):407–409, 1987.
- [38] R. Y. Chiao, E. Garmire, and C. H. Townes. Self-trapping of optical beams. *Phys. Rev. Lett.*, 13:479–482, Oct 1964.
- [39] L. Bergé, S. Skupin, R. Nuter, J. Kasparian, and J-P Wolf. Ultrashort filaments of light in weakly ionized, optically transparent media. *Reports on Progress in Physics*, 70(10):1633, 2007.
- [40] J.H. and Marburger. Self-focusing: Theory. *Progress in Quantum Electronics*, 4, Part 1(0):35 – 110, 1975.
- [41] R. H. Lehmberg, C. J. Pawley, A. V. Deniz, M. Klapisch, and Y. Leng. Two-photon resonantly-enhanced negative nonlinear refractive index in xenon at 248 nm. *Optics Communications*, 121(1-3):78 – 88, 1995.
- [42] Mahesh R. Junnarkar and Naoshi Uesugi. Near two-photon resonance short pulse compression in atomic noble gases. *Optics Communications*, 175(4-6):447 – 459, 2000.
- [43] Christian Köhler, Luc Bergé, and Stefan Skupin. Effect of nonlinear dispersion on pulse self-compression in a defocusing noble gas. *Physica D: Nonlinear Phenomena*, 240(11):963 – 970, 2011.
- [44] Luc Bergé, Christian Köhler, and Stefan Skupin. Compression of ultrashort uv pulses in a self-defocusing gas. *Phys. Rev. A*, 81(1):011805, Jan 2010.
- [45] R. W. Boyd. *Nonlinear Optics*. Academic, New York, 1992.

- 
- [46] L. Bergé and A. Couairon. Gas-induced solitons. *Phys. Rev. Lett.*, 86:1003–1006, Feb 2001.
- [47] K. D. Moll, Alexander L. Gaeta, and Gadi Fibich. Self-similar optical wave collapse: Observation of the townes profile. *Phys. Rev. Lett.*, 90:203902, May 2003. self similar collapse.
- [48] A. Braun, G. Korn, X. Liu, D. Du, J. Squier, and G. Mourou. Self-channeling of high-peak-power femtosecond laser pulses in air. *Opt. Lett.*, 20(1):73–75, Jan 1995.
- [49] A. Brodeur, C. Y. Chien, F. A. Ilkov, S. L. Chin, O. G. Kosareva, and V. P. Kandidov. Moving focus in the propagation of ultrashort laser pulses in air. *Opt. Lett.*, 22(5):304–306, Mar 1997. experimental filament and power in it, moving focus model; numerics.
- [50] Luc Bergé and Stefan Skupin. Modeling ultrashort filaments of light. *Discrete and continuous dynamical systems. Series A*, 23(4):1099, 2008.
- [51] Mysyrowicz A.b Couairon, A.a. Femtosecond filamentation in transparent media. *Physics Reports*, 441(2-4):47–189, 2007. cited By (since 1996) 383.
- [52] M. Mlejnek, E. M. Wright, and J. V. Moloney. Dynamic spatial replenishment of femtosecond pulses propagating in air. *Opt. Lett.*, 23(5):382–384, Mar 1998. theory, dynamical equilibrium.
- [53] Antoine Vinçotte and Luc Bergé.  $\chi^{(5)}$  susceptibility stabilizes the propagation of ultrashort laser pulses in air. *Phys. Rev. A*, 70:061802, Dec 2004.
- [54] I. G. Koprinkov, Akira Suda, Pengqian Wang, and Katsumi Midorikawa. Self-compression of high-intensity femtosecond optical pulses and spatiotemporal soliton generation. *Phys. Rev. Lett.*, 84:3847–3850, Apr 2000.
- [55] Vincent Lorient, Edouard Hertz, Olivier Faucher, and Bruno Lavorel. Measurement of high order kerr refractive index of major air components. *Opt. Express*, 17(16):13429–13434, Aug 2009.
- [56] V. Lorient, E. Hertz, O. Faucher, and B. Lavorel. Measurement of high order kerr refractive index of major air components: erratum. *Opt. Express*, 18(3):3011–3012, Feb 2010.
- [57] Muhammad Nurhuda, Akira Suda, and Katsumi Midorikawa. Generalization of the kerr effect for high intensity, ultrashort laser pulses. *New Journal of Physics*, 10(5):053006, 2008.
- [58] Carsten Brée, Ayhan Demircan, and Günter Steinmeyer. Saturation of the all-optical kerr effect. *Phys. Rev. Lett.*, 106:183902, May 2011.

- [59] A. Teleki, E. M. Wright, and M. Kolesik. Microscopic model for the higher-order nonlinearity in optical filaments. *Phys. Rev. A*, 82:065801, Dec 2010.
- [60] P. Béjot, J. Kasparian, S. Henin, V. Loriot, T. Vieillard, E. Hertz, O. Faucher, B. Lavorel, and J.-P. Wolf. Higher-order kerr terms allow ionization-free filamentation in gases. *Phys. Rev. Lett.*, 104:103903, Mar 2010.
- [61] Olga Kosareva, Jean-Francois Daigle, Nikolay Panov, Tiejun Wang, Sima Hosseini, Shuai Yuan, Gilles Roy, Vladimir Makarov, and See Leang Chin. Arrest of self-focusing collapse in femtosecond air filaments: higher order kerr or plasma defocusing? *Opt. Lett.*, 36(7):1035–1037, Apr 2011.
- [62] G. Fibich, B. Ilan, and S. Tsynkov. Computation of nonlinear backscattering using a high-order numerical method. *J. Scien. Comput.*, 17:351, 2002.
- [63] A. V. Husakou and J. Herrmann. Supercontinuum generation of higher-order solitons by fission in photonic crystal fibers. *Phys. Rev. Lett.*, 87:203901, 2001.
- [64] M. Kolesik and J. V. Moloney. Nonlinear optical pulse propagation simulation: From maxwell’s to unidirectional equations. *Phys. Rev. E*, 70(3):036604, Sep 2004.
- [65] G Mainfray and G Manus. Multiphoton ionization of atoms. *Reports on Progress in Physics*, 54(10):1333, 1991.
- [66] L. V. Keldysh. Ionization in the field of a strong electromagnetic wave. *Soviet Physics JETP*, 20(5):1307, 1965.
- [67] Vladimir S Popov. Tunnel and multiphoton ionization of atoms and ions in a strong laser field (keldysh theory). *Physics-Uspekhi*, 47(9):855, 2004.
- [68] M. Uiberacker, Th. Uphues, M. Schultze, A. J. Verhoef, V. Yakovlev, M. F. Kling, J. Rauschenberger, N. M. Kabachnik, H. Schroder, M. Lezius, K. L. Kompa, H.-G. Muller, M. J. J. Vrakking, S. Hendel, U. Kleineberg, U. Heinzmann, M. Drescher, and F. Krausz. Attosecond real-time observation of electron tunnelling in atoms. *Nature*, 446:627–632, 2007.
- [69] Aart J. Verhoef, Alexander V. Mitrofanov, Evgenii E. Serebryannikov, Daniil V. Kartashov, Aleksei M. Zheltikov, and Andrius Baltuška. Optical detection of tunneling ionization. *Phys. Rev. Lett.*, 104:163904, Apr 2010.
- [70] P. B. Corkum, N. H. Burnett, and F. Brunel. Above-threshold ionization in the long-wavelength limit. *Phys. Rev. Lett.*, 62(11):1259–1262, Mar 1989.
- [71] M. V. Ammosov, N. D. Delone, and V. P. Krainov. Tunnel ionization of complex atoms and of atomic ions in an alternating electromagnetic field. *Zh. Eksp. Teor. Fiz.*, 91:2008–2013, 1986.



- 
- [72] L. D. Landau and E. M. Lifshitz. *Quantum mechanics: non-relativistic theory*, volume 3. Pergamon Press, 3 edition, 1977.
- [73] P. Sprangle, E. Esarey, and J. Krall. Self-guiding and stability of intense optical beams in gases undergoing ionization. *Phys. Rev. E*, 54:4211–4232, Oct 1996.
- [74] S Tzortzakis, B Prade, M Franco, and A Mysyrowicz. Time-evolution of the plasma channel at the trail of a self-guided ir femtosecond laser pulse in air. *Optics Communications*, 181(1–3):123 – 127, 2000.
- [75] P. Sprangle, J. R. Peñano, B. Hafizi, and C. A. Kapetanacos. Ultrashort laser pulses and electromagnetic pulse generation in air and on dielectric surfaces. *Phys. Rev. E*, 69:066415, Jun 2004.
- [76] M. D. Feit and Jr. J. A. Fleck. Effect of refraction on spot-size dependence of laser-induced breakdown. *Applied Physics Letters*, 24(4):169–172, 1974.
- [77] O. D. Jefimenko. *Electricity and Magnetism: An Introduction to the Theory of Electric and Magnetic Fields*. Appleton-Century-Crofts, New-York, 1966.
- [78] I Babushkin, S Skupin, A Husakou, C Köhler, E Cabrera-Granado, L Bergé, and J Herrmann. Tailoring terahertz radiation by controlling tunnel photoionization events in gases. *New Journal of Physics*, 13(12):123029, 2011.
- [79] I. Babushkin, S. Skupin, and J. Herrmann. Generation of terahertz radiation from ionizing two-color laser pulses in ar filled metallic hollow waveguides. *Opt. Express*, 18(9):9658–9663, Apr 2010.
- [80] C. Köhler, E. Cabrera-Granado, I. Babushkin, L. Bergé, J. Herrmann, and S. Skupin. Directionality of terahertz emission from photoinduced gas plasmas. *Opt. Lett.*, 36(16):3166–3168, Aug 2011.
- [81] Prof. Falk Lederer. Grundkonzepte der optik. Lecture Notes, 2008.
- [82] A. Dalgarno and A. E. Kingston. The refractive indices and verdet constants of the inert gases. *Proceedings of the Royal Society of London. Series A, Mathematical and Physical Sciences*, 259(1298):pp. 424–431, 1960.
- [83] Kane Yee. Numerical solution of initial boundary value problems involving maxwell’s equations in isotropic media. *Antennas and Propagation, IEEE Transactions on*, 14(3):302 –307, may 1966.
- [84] R.M. Joseph and A. Taflove. Fdtd maxwell’s equations models for nonlinear electrodynamics and optics. *Antennas and Propagation, IEEE Transactions on*, 45(3):364 –374, mar 1997.

- [85] A. Leitenstorfer, S. Hunsche, J. Shah, M. C. Nuss, and W. H. Knox. Detectors and sources for ultrabroadband electro-optic sampling: Experiment and theory. *Applied Physics Letters*, 74(11):1516–1518, 1999.
- [86] Wm. M. Wood, C. W. Siders, and M. C. Downer. Measurement of femtosecond ionization dynamics of atmospheric density gases by spectral blueshifting. *Phys. Rev. Lett.*, 67:3523–3526, Dec 1991.
- [87] S. C. Rae and K. Burnett. Detailed simulations of plasma-induced spectral blueshifting. *Phys. Rev. A*, 46:1084–1090, Jul 1992.
- [88] P. J. Leonard. Refractive indices, verdet constants, and polarizabilities of the inert gases. *atomic data and nuclear data tables*, 14:21–37, 1974.
- [89] H. A. Lorentz. über die beziehung der fortpflanzungsgeschwindigkeit des lichtes und der körperdichte. *Ann. Phys. Chem.*, 9:641 – 665, 1880.
- [90] L. Lorenz. über die refractionsconstante. *Wiedem. Ann.*, 11:70–103, 1881.
- [91] V. I. Karpman. Self-modulation of nonlinear plane waves in dispersive media. *Zh. Eksp. Teor. Fiz. Pis'ma Red.*, 6:829, 1967.
- [92] A. Hasegawa and W. Brinkman. Tunable coherent ir and fir sources utilizing modulational instability. *Quantum Electronics*, 16(7):694 – 697, 1980.
- [93] Govind P. Agrawal. *Nonlinear fiber optics*. Academic Press, 3 edition, 2001.
- [94] Junkichi Satsuma and Nobuo Yajima. B. initial value problems of one-dimensional self-modulation of nonlinear waves in dispersive media. *Progress of Theoretical Physics Supplement*, 55:284–306, 1974.
- [95] V. I. Karpman. Radiation of solitons described by a high-order cubic nonlinear schrödinger equation. *Phys. Rev. E*, 62(4):5678–5687, Oct 2000.
- [96] Y. R. Shen. *The Principles of Nonlinear Optics*. John Wiley & Sons, New-York, 1984.
- [97] Luc Bergé and Jens Juul Rasmussen. Multisplitting and collapse of self-focusing anisotropic beams in normal/anomalous dispersive media. *Physics of Plasmas*, 3(3):824–843, 1996.
- [98] V. I. Bespalov and V. I. Talanov. Filamentary structure of light beams in nonlinear liquids. *JETP Lett.*, 3:307–310, Apr 1966.
- [99] A. Couairon and L. Berge. Modeling the filamentation of ultra-short pulses in ionizing media. *Physics of Plasmas*, 7(1):193–209, 2000.

- [100] B.H. Bransden and C.J. Joachain. *Physics of atoms and molecules*. Pearson Education. Prentice Hall, 2003.
- [101] Yong-Chang Han and Lars Bojer Madsen. Comparison between length and velocity gauges in quantum simulations of high-order harmonic generation. *Phys. Rev. A*, 81:063430, Jun 2010.
- [102] Donald H. Kobe. Implications of gauge invariance for length versus velocity forms of the interaction with electric dipole radiation. *International Journal of Quantum Chemistry*, 14(S12):73–86, 1978.
- [103] S. C. Rae, X. Chen, and K. Burnett. Saturation of harmonic generation in one- and three-dimensional atoms. *Phys. Rev. A*, 50:1946–1949, Aug 1994.
- [104] A. A. Silaev, M. Yu. Ryabikin, and N. V. Vvedenskii. Strong-field phenomena caused by ultrashort laser pulses: Effective one- and two-dimensional quantum-mechanical descriptions. *Phys. Rev. A*, 82:033416, Sep 2010.
- [105] W. H. Press. *Numerical Recipes in Fortran: The Art of Scientific Computing*. Cambridge University Press, 2 edition, 1992.



# Acknowledgments

I would like to thank all the people, who made this work possible.

First, I wish to thank my supervisor Prof. Stefan Skupin for his excellent scientific mentoring. His mind and door were always open for sincere and stupid questions and I am indebted for his untiring patience in finding bugs in the code and explaining physical situations. His motivating presence not only provided my knowledge how to deal with scientific life, but also taught me that Thüringer Rostbratwurst is way better than anything else and what the issue with french hotel rooms is.

Moreover, I thank Dr. Luc Bergé for productive collaborations, fruitful discussions and kind hospitality during my visits in France and his eagle eye when revising manuscripts.

There are all the people from the institutes floor I'd like to thank. Eduardo for the inspiring experience of closely collaborating and the numerous coffee sessions with Elena outside Mensa. Fabian for not giving up in teaching me kicker in endless sessions and elucidating the world around GDP. Micka for all the small breaks outside the institute and for one of my first french sentences "Je vais ...". My office mates Pierfrancesco (who is still looking for a citable statement) and Karsten for the relaxing and productive atmosphere and company at lunch, along with Evangelos and Jörg, also for reviewing the manuscript. And of course all the others I met in line at the coffee machine (thanks Gerhard and Sebastian for providing continuous flow) and around the institute who contributed to the enjoyable everyday life.

Additional thanks go to Werner, who also very constructively proofread my thesis.

I'd like to thank my parents Angelika and Matthias, who continuously supported me and without whom I would not be where I am.

The biggest thanks I owe Yvonne, who bore me even during the finishing period of my thesis, when work seemed to be more important than everything else.



# Versicherung

Hiermit versichere ich, dass ich die vorliegende Arbeit ohne unzulässige Hilfe Dritter und ohne Benutzung anderer als der angegebenen Hilfsmittel angefertigt habe; die aus fremden Quellen direkt oder indirekt übernommenen Gedanken sind als solche kenntlich gemacht. Die Arbeit wurde bisher weder im Inland noch im Ausland in gleicher oder ähnlicher Form einer anderen Prüfungsbehörde vorgelegt.

Die Arbeit wurde am Max-Planck-Institut für Physik komplexer Systeme in der Abteilung „Endliche Systeme“ angefertigt und von Prof. Dr. Jan-Michael Rost betreut. Ich erkenne die Promotionsordnung der Fakultät Mathematik und Naturwissenschaften der Technischen Universität Dresden vom 23.02.2011 an.

---

Christian Köhler